
Theses and Dissertations

Spring 2016

Individual submicrometer particles and biomolecular systems studied on the nanoscale

Holly Sue Morris VanMetre
University of Iowa

Copyright 2016 Holly VanMetre

This dissertation is available at Iowa Research Online: <http://ir.uiowa.edu/etd/3207>

Recommended Citation

VanMetre, Holly Sue Morris. "Individual submicrometer particles and biomolecular systems studied on the nanoscale." PhD (Doctor of Philosophy) thesis, University of Iowa, 2016.
<http://ir.uiowa.edu/etd/3207>.

Follow this and additional works at: <http://ir.uiowa.edu/etd>



Part of the [Chemistry Commons](#)

INDIVIDUAL SUBMICROMETER
PARTICLES AND BIOMOLECULAR
SYSTEMS STUDIED ON THE NANOSCALE

by

Holly Sue Morris (VanMetre)

A thesis submitted in partial fulfillment
of the requirements for the Doctor of Philosophy
degree in Chemistry in the
Graduate College of
The University of Iowa

May 2016

Thesis Supervisor: Professor Alexei V. Tivanski

Copyright by

HOLLY SUE MORRIS (VANMETRE)

2016

All Rights Reserved

Graduate College
The University of Iowa
Iowa City, Iowa

CERTIFICATE OF APPROVAL

PH.D. THESIS

This is to certify that the Ph.D. thesis of

Holly Sue Morris (VanMetre)

has been approved by the Examining Committee for
the thesis requirement for the Doctor of Philosophy degree
in Chemistry at the May 2016 graduation.

Thesis Committee:

Alexei V. Tivanski, Thesis Supervisor

Vicki H. Grassian

Amnon Kohen

Scott K. Shaw

Gregory R. Carmichael

To my parents Val and Steve Morris, grandparents Evelyn and Ervin Morris, Mary Jo and Russel Sutton, sister Angie Thorn, brother Craig Morris, and my husband Nathan VanMetre.

An investment in knowledge pays the best interest.
Benjamin Franklin

ACKNOWLEDGEMENTS

I would, first, like to thank my family for their unwavering support during my Ph.D. career, especially my parents. Your reassurance and encouragement is what motivated me to keep going.

I am grateful for the following scientists and mentors: Angie Thorn for all our fun science discussions, taking classes/studying together, and always helping me with statistics. Professor Audra Sostarecz who inspired me early in my academic career to be a great chemist and inspired me to pursue my Ph.D. Lindsay Ditzler provided me with guidance and taught me skills that made my graduate career successful. Olga Laskina taught me how to be a successful chemist both inside and outside of the laboratory. Professor Vicki Grassian who provided me with many opportunities, advice and inspiration during my graduate career. My collaborators Professor Amnon Kohen and Professor Betsy Stone for their guidance.

Finally, I would like to thank my thesis advisor Alexei Tivanski. You taught me how to be a great chemist. You were always patient, understanding, and an overall great role model.

ABSTRACT

The necessity to explore nanoscopic systems is ever increasing in the world of science and technology. This evolving need to study such physically small systems demands new experimental techniques and methodologies. Atomic force microscopy (AFM) is a versatile technique that can overcome many nanoscopic size limitations. AFM has been utilized in the world of nanotechnology to study physiochemical properties of particles, materials, and biomolecules through characterization of morphology, electrical and mechanical properties, binding interactions, and surface tension, among others. The work discussed herein is largely a report of several novel AFM methodologies that were developed to allow new characterization techniques of individual submicrometer particles and single biomolecular interactions.

The effects of atmospheric aerosols on the radiative budget of the earth and climate are largely unknown. For this reason, characterizing the physiochemical properties of aerosols is vital. Since the particles that have relatively long lifetimes in the atmosphere are smaller than one micrometer in size, high resolution microscopy techniques are required to study them. AFM is a suitable technique for single particle studies because it has nanometer spatial resolution, can perform experiments under ambient pressure and variable relative humidity and temperature. These advantages were utilized here and AFM was used to study morphology, organic volume fraction, water uptake, and surface tension of nascent sea spray aerosol (SSA) particles as well as laboratory generated aerosols composed of relevant chemical model systems. The morphology of SSA was found, often times, to be composed of core-shell structure. With complementary microscopy techniques, the composition of the core and the shell was

found to be inorganic and organic in nature, respectively. Novel methodology to measure water uptake and surface tension of single substrate deposited particles with AFM was established using chemical model systems. Furthermore, these methodologies were employed on nascent chemically complex SSA particles collected from a biologically active oceanic waveflume experiment. Finally, phase imaging was used to measure organic volume fraction on a single particle basis and was correlated with biological activity. Overall, this suite of single (submicrometer) particle AFM analysis techniques have been established, allowing future systematic studies of increasing complexity aimed at bridging the gap between the simplicity of laboratory generated particles and the complexity of nature.

Another nanotechnology topic of interest is studying single biomolecular interactions. Virtually every biological process involves some amount of minute forces that are required for the biomolecular system to function properly. For example, there are picoNewton forces associated with enzymatic motions that are important for enzyme catalysis. The AFM studies reported here use a model enzyme/drug system to measure the forces associated with single molecule adhesion events. Escherichia Dihydrofolate Reductase (DHFR) is a target of cancer therapeutic studies because it can be inhibited by drugs like methotrexate (MTX) that are structurally similar to the natural folate binder but have much higher binding affinity. One of the obstacles of single molecular recognition force spectroscopy (MRFS) studies is the contribution of non-specific forces that create a source of uncertainty. In this study, DHFR and MTX are bound to the surface and the AFM tip, respectively, using several different linking molecules. These linking molecules included polyethylene glycol (PEG) and double stranded DNA

(dsDNA) and the distribution of forces was compared to scenarios where a linker was not employed. We discovered that dsDNA and PEG both allow identification and removal of non-specific interaction forces from specific forces of interest, which increases the accuracy of the measurement compared to directly bound constructs. Traditionally, the linker of choice in the MRFS community is PEG. Here, we introduce dsDNA as a viable linker that offers more rigidity than PEG, which may be desirable in future molecular constructs.

The majority of the work and data presented in this dissertation supports the establishment of new AFM methodologies that can be used to better explore single biomolecular interactions and individual submicrometer particles on the nanoscale.

PUBLIC ABSTRACT

As the world of science and technology advances, so does the need to study systems that are physically too small to measure with traditional science techniques. For example, particles in the atmosphere (dust and pollution) are smaller than one millionth of a meter in diameter. For comparison, the diameter of a human hair is about one hundred times larger than the average atmospheric particle. Unfortunately, the effects of particles on the climate and the environment remain largely unknown because we need high resolution analysis techniques to be able to study such small scale systems.

Another nanoscopic system of interest is single-biomolecular binding events like a drug binding with an enzyme. These fundamental processes control how enzymes work and how by inhibiting an enzyme with a drug, we can treat diseases like cancer. Studying these processes on a single-molecule basis will gain us insights on their mechanisms and improve our understanding of the catalytic processes of enzymes to ultimately facilitate the development of new and better therapies.

Atomic force microscopy (AFM) is a powerful tool capable of nanoscale imaging and measuring extremely minute forces. The research presented herein describes several novel AFM techniques that were developed to study individual nanoscopic atmospheric particles and biomolecular systems. Ultimately, this work strives to better understand the physicochemical properties of atmospheric particles to determine their effect on climate and environment. Furthermore, we developed new and better methodology to facilitate accurate drug-enzyme binding force detection that will help reveal fundamental insights on single biomolecular systems.

TABLE OF CONTENTS

LIST OF TABLES	xiv
LIST OF FIGURES	XVI
1. INTRODUCTION	1
1.1 Introduction to AFM	1
1.2 AFM theory of operation.....	2
1.3 Atmospheric Aerosols	5
1.3.1 Direct effect	7
1.3.2 Indirect effect.....	7
1.3.3 Hygroscopicity	8
1.3.4 Surface tension	9
1.4 Sea spray aerosol.....	10
1.5 Molecular recognition force spectroscopy	13
2. EXPERIMENTAL METHODS	15
2.1 Aerosol generation	15
2.1.1 Atomizer	15
2.1.2 Marine aerosol reference tank	17
2.1.3 Waveflume	19
2.2 Aerosol collection	19
2.3 Humidity controlled AFM.....	22
3. SUBSTRATE-DEPOSITED SEA SPRAY AEROSOL PARTICLES: INFLUENCE OF ANALYTICAL METHOD, SUBSTRATE, AND STORAGE CONDITIONS ON PARTICLE SIZE, PHASE, AND MORPHOLOGY	23
3.1 Abstract	23
3.2 Introduction	24

3.3 Experimental	26
3.3.1 Synthetic phytoplankton bloom.....	26
3.3.2 Sample collection and storage	26
3.3.3 Microscopy methods	28
3.3.4 Size and shape analysis	29
3.4 Results and Discussion.....	31
3.5 Conclusions	49
4. SIZE MATTERS IN THE WATER UPTAKE AND HYGROSCOPIC GROWTH OF ATMOSPHERICALLY RELEVANT MULTICOMPONENT AEROSOL PARTICLES	51
4.1 Abstract	51
4.2 Introduction	51
4.3 Experimental	54
4.3.1 Sample preparation	54
4.3.2 Hygroscopic Tandem Differential Mobility Analyzer (HTDMA).....	55
4.3.3 Micro-Raman spectroscopy.....	56
4.3.4 Atomic Force Microscopy (AFM).....	57
4.3.5 Ambient Pressure SEM coupled with EDX Spectroscopy	58
4.4 Results	58
4.4.1 Ammonium sulfate and sodium chloride	58
4.4.2 Sodium chloride mixed with malonic acid, 2:1 molar ratio	63
4.4.3 Ammonium sulfate mixed with adipic acid, 1:1 weight ratio	66
4.4.4 Ammonium sulfate mixed with succinic acid, 1:1 weight ratio	69
4.4.5 Marine chloride mixture	72

4.5 Discussion	73
4.5 Conclusions	79
5. QUANTIFYING THE HYGROSCOPIC GROWTH OF SUBMICROMETER PARTICLES WITH ATOMIC FORCE MICROSCOPY	81
5.1 Abstract	81
5.2 Introduction	82
5.3 Experimental	86
5.3.1 Substrate deposited particles.	86
5.3.2 Hygroscopic Tandem Differential Mobility Analyzer (HTDMA)	87
5.3.3 Atomic Force Microscopy (AFM) and water uptake	87
5.4 Results and Discussion.....	88
5.5 Conclusions	101
6. QUANTIFYING ORGANIC VOLUME FRACTION OF INDIVIDUAL SEA SPRAY AEROSOL PARTICLES	103
6.1 Introduction	103
6.2 Experimental	105
6.2.1 Organic volume fraction.....	105
6.2.3 MART.....	106
6.2.3 IMPACTS.....	106
6.3 Results and Discussion.....	107
6.3.1 MART.....	107
6.3.2 IMPACTS.....	109
6.4 Conclusions	112

7. HUMIDITY-DEPENDENT SURFACE TENSION MEASUREMENT OF INDIVIDUAL INORGANIC AND ORGANIC SUBMICROMETRE LIQUID PARTICLES	113
7.1 Abstract	113
7.2 Introduction	114
7.3 Experimental	116
7.3.1 Sample preparation	116
7.3.2 AFM based force spectroscopy	117
7.3.3 Bulk surface tension measurements	118
7.4 Results and Discussion	118
7.4.1 AFM surface tension measurements	118
7.4.2 NaCl AFM results.....	121
7.4.3 GA and MA AFM Results.....	123
7.5 Conclusions	126
8. SIZE-DEPENDENT SURFACE TENSION DEPRESSION OF INDIVIDUAL SUBMICROMETER SEA SPRAY AEROSOL CORRELATES WITH ORGANIC ENRICHMENT DURING A PHYOPLANKTON BLOOM	127
8.1 Abstract	127
8.2 Introduction	127
8.3 Experimental	130
8.4 Results and Discussion	130
8.4.1 SSA generation	130
8.4.2 Particle morphology and organic volume fraction	132
8.4.3 AFM surface tension measurements	136
8.4.4 Particle size dependence	140

8.5 Conclusions	142
9. PROBING SINGLE MOLECULE ENZYME-DRUG INTERACTION WITH MOLECULAR RECOGNITION FORCE SPECTROSCOPY	144
9.1 Abstract	144
9.2 Introduction	144
9.3 Experimental	146
9.3.1 Materials	146
9.3.2 AFM imaging and force spectroscopy	147
9.3.3 Directly bound MTX - AFM probe functionalization procedure	148
9.3.4 PEG bound MTX - AFM probe functionalization procedure	149
9.3.5 dsDNA bound MTX - AFM probe functionalization procedure	151
9.3.6 Substrate functionalization procedure of dsDNA on mica	152
9.3.7 Control Experiments	152
9.4 Results and Discussion	158
9.5 Conclusions	167
10. CONCLUSIONS AND FUTURE WORK	168
10.1 SSA Single Particle Measurements	168
10.2 Molecular Recognition studies	169
REFERENCES	171

LIST OF TABLES

Table 2.1: MOUDI stages and corresponding size ranges.....	20
Table 3.1: Summary of storage conditions used in this study	28
Table 3.2: Circularity Parameter Calculated for Different Two-Dimensional Geometric Shapes.....	30
Table 3.3: Average and standard deviation of the area equivalent diameter and circularity measured for SSA particles analyzed using OM, AFM and SEM in 3, 5 and 7 weeks after particle collection at ambient and frozen storage conditions. OM data was collected by Olga Laskina (Grassian group,University of Iowa) SEM data was collected by Josh Grandquist (Grassian group, University of Iowa)	37
Table 3.4: The number of SSA particles analyzed using OM, AFM and SEM in 3, 5 and 7 weeks after particle collection at different storage conditions. OM data was collected by Olga Laskina (Grassian group, University of Iowa) SEM data was collected by Josh Grandquist (Grassian group, University of Iowa).....	37
Table 3.5: Average and standard deviation of the area equivalent diameter and circularity measured for NaCl/malonic acid particles analyzed using OM, AFM and SEM as prepared, 2 and 4 weeks later stored at ambient, frozen and desiccator storage conditions. OM data was collected by Olga Laskina (Grassian group, University of Iowa) SEM data was collected by Josh Grandquist (Grassian group, University of Iowa).....	43
Table 3.6: The number of NaCl/malonic acid particles analyzed using OM, AFM and SEM as prepared, 2 and 4 weeks later at different storage conditions. OM data was collected by Olga Laskina (Grassian group, University of Iowa) SEM data was collected by Josh Grandquist (Grassian group, University of Iowa).....	43
Table 3.7: Positions and assignments of the bands observed in the Raman spectra of NaCl/malonic acid particles.....	47
Table 4.1: Measured DRH and ERH values for single component and multi-components particle compositions at two size ranges: 100 nm, submicron, as measured using HTDMA system, and 3-10 μm , supermicron, as measured using micro-Raman spectroscopy. Data was collected by Olga Laskina (Grassian group, University of Iowa)	61

Table 5.1: Average and standard deviation of area and volume GFs determined with AFM and compared with the GF determined by HTDMA ($298 \pm 2K$). HTDMA data was collected by Armando Estillore (Grassian group, University of Iowa).....	91
Table 8.1: Average and standard deviation surface tension values of particles 0.56 – 1.0 μm in size	138
Table 9.1: The number of individual force measurements for the distributions reported in the main text.....	148
Table 9.2: Rupture distances and mean rupture forces measured for the 5 linking scenarios before and after MTX blocking control study.....	163

LIST OF FIGURES

Figure 1.1: Schematic representation of AFM.....	2
Figure 1.2: Example of tapping mode height (A), amplitude (B), phase (C), and 3D height (D) images.....	3
Figure 1.3: Typical force-distance cycle.....	4
Figure 1.4: Direct and indirect effects of aerosols in the atmosphere.	6
Figure 1.5: Factors affecting the radiative forcing budget of the earth	6
Figure 1.6: Theoretical hydration curves for (A) NaCl (B) malonic acid and (C) glutaric acid.....	9
Figure 1.7: Pictorial of different bubble bursting mechanisms. Bubbles are typically enriched in organic molecules at the air-water interface. When the bubble film burst, it creates many small submicron droplets that are enriched with organic compounds. A second event occurs when a jet stream rises in the bubble cavity and produces larger jet droplets that tend to resemble more of a “bulk” water composition.	11
Figure 1.8: Typical force –distance cycle for a MRFS experiment.....	14
Figure 2.1: Schematic of the TSI atomizer. Adapted from TSI Inc. (Model 3076) atomizer user manual	16
Figure 2.2: Size distribution of particles generated via atomization of NaCl from 3 different aqueous solution concentrations. Adapted from TSI Inc. (Model 3076) atomizer user manual	16
Figure 2.3: Picture of a MART tank. A. The tank. B. Spillway slot. C. Flow meter. D. Water sampling spigot. E. Pump. F. Flow control valve. G. Timing relay control box. H. Tank drain and purge valves. I. Solenoid valve. Adapted from M. D. Stokes et al. <i>Atmospheric Measurement Techniques</i> 2013, 6, 1085.....	17
Figure 2.4: Probability density functions of SSA number distributions generated by a plunging sheet, breaking waves and sintered glass filter. Size distribution for breaking wave and plunging sheet are larger than for atomization. Adapted from M. D. Stokes et al. <i>Atmospheric Measurement Techniques</i> 2013, 6, 1085.....	18

Figure 2.5: Picture of the waveflume at the Scripps Institute of Oceanography. Adapted from Prather et al. <i>Proceeding of the National Academy of Science</i> 2013, 10, 7550	19
Figure 2.6: Picture of MOUDI. Adapted from MSP MOUDI (Model 110) user manual.....	21
Figure 2.7: Schematic of the interior of MOUDI column detailing aerosol path and impaction. Adapted from MSP MOUDI (Model 110) user manual	21
Figure 2.8: Schematic of the AFM RH cell attachment. ⁵⁷ The RH of air entering the cell is controlled by two flow meters – one controlling the amount of dry air and one controlling the amount of hydrated air. The RH is measured inside the cell using humidity sensor	22
Figure 3.1: Comparison of microscopy methods on particles size and shape: a) representative OM, AFM height and SEM images of SSA particles deposited on a quartz disc, silicon nitride membrane and silicon wafer, respectively. b) Histograms of area equivalent diameters for three microscopy methods with corresponding mean and standard deviation values. OM data was collected by Olga Laskina (Grassian group, University of Iowa) SEM data was collected by Josh Grandquist (Grassian group, University of Iowa)	31
Figure 3.2: SEM images of particles collected from NaCl/malonic acid mixture on WETSEM capsule and imaged a) captured inside the WETSEM capsule under 15-20% RH and ambient pressure and b) under vacuum conditions. SEM data was collected by Josh Grandquist (Grassian group, University of Iowa)	33
Figure 3.3: Representative AFM height images of SSA particles deposited on silicon nitride, silicon and quartz substrates showing similar morphology and size range	34
Figure 3.4: a) OM, b) AFM, c) SEM images of sea spray aerosol particles stored under ambient laboratory conditions (top) and frozen at -12°C (bottom). Images were collected 3, 5 and 7 weeks after particle collection. OM data was collected by Olga Laskina (Grassian group, University of Iowa) SEM data was collected by Josh Grandquist (Grassian group, University of Iowa)	34

Figure 3.5: Circularity of SSA particles determined using OM (a), AFM (b) and SEM (c) 3, 5 and 7 weeks after particle collection at different storage conditions. The horizontal line represents the average value of the data set. OM data was collected by Olga Laskina (Grassian group, University of Iowa) SEM data was collected by Josh Grandquist (Grassian group, University of Iowa)	35
Figure 3.6: Area equivalent diameter histograms of SSA particles as probed using OM 3, 5 and 7 weeks after particle collection at different storage conditions. OM data was collected by Olga Laskina (Grassian group, University of Iowa) SEM data was collected by Josh Grandquist (Grassian group, University of Iowa)	35
Figure 3.7: Area equivalent diameter histograms of SSA particles as probed using AFM 3, 5 and 7 weeks after particle collection at different storage conditions. OM data was collected by Olga Laskina (Grassian group, University of Iowa) SEM data was collected by Josh Grandquist (Grassian group, University of Iowa)	36
Figure 3.8: Area equivalent diameter histograms of SSA particles as probed using SEM 3, 5 and 7 weeks after particle collection at different storage conditions. OM data was collected by Olga Laskina (Grassian group, University of Iowa) SEM data was collected by Josh Grandquist (Grassian group, University of Iowa)	36
Figure 3.9: Comparison of mean area equivalent diameters of SSA particles determined using OM (a), AFM (b) and SEM (c) in 3, 5 and 7 weeks after particle collection at ambient and frozen storage conditions. The error bars correspond to one standard deviation. OM data was collected by Olga Laskina (Grassian group, University of Iowa) SEM data was collected by Josh Grandquist (Grassian group, University of Iowa).	38
Figure 3.10: a) OM, b) AFM, c) SEM images of particles collected from NaCl/malonic acid stored in desiccator, under ambient laboratory conditions, and frozen at -12°C. Images were acquired right after particle collection, 2 and 4 weeks later. OM data was collected by Olga Laskina (Grassian group, University of Iowa) SEM data was collected by Josh Grandquist (Grassian group, University of Iowa)	40
Figure 3.11: Area equivalent diameter histograms of NaCl/MA particles as probed using OM 0, 4 and 2 weeks after particle collection at different storage conditions. OM data was collected by Olga Laskina (Grassian group, University of Iowa) SEM data was collected by Josh Grandquist (Grassian group, University of Iowa)	40

Figure 3.12: Diameter histograms of NaCl/MA particles as probed using AFM 0, 2 and 4 weeks after particle collection at different storage conditions. OM data was collected by Olga Laskina (Grassian group, University of Iowa) SEM data was collected by Josh Grandquist (Grassian group, University of Iowa).....	41
Figure 3.13: Diameter histograms of NaCl/MA particles as probed using SEM 0, 2 and 4 weeks after particle collection at different storage conditions. OM data was collected by Olga Laskina (Grassian group, University of Iowa) SEM data was collected by Josh Grandquist (Grassian group, University of Iowa).....	42
Figure 3.14: Circularity of NaCl/MA particles determined using OM (a), AFM (b) and SEM (c) in 0, 2 and 4 weeks after particle collection at different storage conditions. The horizontal line represents the average of the data set. OM data was collected by Olga Laskina (Grassian group, University of Iowa) SEM data was collected by Josh Grandquist (Grassian group, University of Iowa).....	42
Figure 3.15: Comparison of mean area equivalent diameters of NaCl/malonic acid particles determined using OM (a), AFM (b) and SEM (c) as prepared, 2 and 4 weeks later stored at ambient, frozen and desiccator storage conditions. The error bars correspond to one standard deviation. OM data was collected by Olga Laskina (Grassian group, University of Iowa) SEM data was collected by Josh Grandquist (Grassian group, University of Iowa).....	44
Figure 3.16: Particle height plotted as a function of area equivalent diameter analyzed for a) week 7 SSA particles and b) week 4 NaCl/MA particles. Symbols are individual particles data, while solid lines are linear fits.....	45
Figure 3.17: Raman spectra of reacted NaCl/malonic acid at different stages of solvation: dry (top), solvated (middle) and partially solvated (bottom). Peak assignments are shown in Table 3.7. All three types are found in freshly prepared sample as well as in the sample stored at ambient conditions after 2 and 4 weeks of storage. In the sample stored in desiccator only dry and partially solvated particles can be found. Frozen sample only shows solvated particles. Raman data was collected by Olga Laskina (Grassian group, University of Iowa).....	47
Figure 3.18: A) Schematic of freezing experiments performed. B) Representative AFM images from each experiment. Scale bar is 5 μm . C) Scatterplot of area equivalent diameter for each freezing scenario compared to newly prepared particles (ambient). Solid horizontal lines correspond to the mean diameter values.....	49

Figure 4.1: a) AS and b) NaCl Raman spectra of dry (red) and deliquesced (blue) particles are shown as representative spectra. Raman spectra of the substrate (quartz) is also shown for reference (black). Raman data was collected by Olga Laskina (Grassian group, University of Iowa).59

Figure 4.2: a) AS and b) NaCl hygroscopicity measured by HTDMA for 100 nm particles (red triangles) and micro-Raman results for supermicron particles (blue triangles). Theoretical Kohler curves are shown in black. Data was collected by Olga Laskina (Grassian group, University of Iowa).63

Figure 4.3: a) AFM phase images at 10% RH of submicron and supermicron NaCl/MA (2:1 molar ratio) particles and b) SEM image and Cl, Na, C, O elemental maps of a supermicron particle captured at 20% RH in a WETSEM capsule; c) hygroscopicity measured by HTDMA for 100 nm particles (red triangles) and by micro-Raman spectroscopy for supermicron particles (blue triangles). Hygroscopicity data was collected by Olga Laskina (Grassian group, University of Iowa) and SEM data was collected by Josh Grandquist (Grassian group, University of Iowa).66

Figure 4.4: Raman spectra of ammonium sulfate and adipic acid particles (black) and ammonium sulfate/adipic acid mixed particles (red). Blue box highlights the region used to construct an adipic acid map ($900-930\text{ cm}^{-1}$), red box highlights the region used to construct an ammonium sulfate map ($960-990\text{ cm}^{-1}$). Data was collected by Olga Laskina (Grassian group, University of Iowa).67

Figure 4.5: a) AFM phase images at 10% RH of submicron and supermicron AS/AA particles and b) Raman image, AS and AA maps of a supermicron particle at 20% RH; c) hygroscopicity measured by HTDMA for 100 nm particles (red triangles) and micro-Raman spectroscopy for supermicron particles (blue triangles). Raman and hygroscopicity data was collected by Olga Laskina (Grassian group, University of Iowa).69

Figure 4.6: a) AFM phase images at 10% RH of submicron and supermicron AS/SA particles and b) Raman image, AS and SA maps of a supermicron particle at 20% RH; c) hygroscopicity measured by HTDMA for 100 nm particles (red triangles) and micro-Raman spectroscopy for supermicron particles (blue triangles). Dashed arrows indicate deliquescence of submicron (red) and supermicron (blue) particles. $\Delta\text{DRH} = 9.5\%$ is the difference between DRH values of submicron and 100 nm particles. Raman and hygroscopicity data was collected by Olga Laskina (Grassian group, University of Iowa).70

Figure 4.7: Raman spectra of ammonium sulfate and succinic acid particles (black) and ammonium sulfate/succinic acid mixed particles (red). Blue box highlights the region used to construct a succinic acid map ($920\text{-}950\text{ cm}^{-1}$), red box highlights the region used to construct an ammonium sulfate map ($960\text{-}990\text{ cm}^{-1}$). Data was collected by Olga Laskina (Grassian group, University of Iowa).....71

Figure 4.8: a) AFM phase images of marine chloride mixture at 10% RH of submicron (right) and supermicron (left) particles and b) SEM image and Cl, Na, Mg, Ca, K elemental maps of a supermicron particle captured at 20% RH in WETSEM capsule; c) hygroscopicity of mixed chloride particles measured by HTDMA for 100 nm particles (red triangles) and micro-Raman spectroscopy for supermicron particles (blue triangles). Dashed arrows indicate deliquescence of submicron (red) and supermicron (blue). $\Delta\text{DRH} = 9.2\%$ is the difference between DRH values of submicron and 100 nm particles. Hygroscopicity data was collected by Olga Laskina (Grassian group, University of Iowa) SEM data was collected by Josh Grandquist (Grassian group, University of Iowa).....73

Figure 5.1: A. NaCl dry deposition results. A. 3D AFM images of a NaCl particle at 5% RH and corresponding deliquesced liquid droplet at 80% RH. B. Cross section of particle at 5% RH (red) and corresponding deliquesced liquid droplet at 80% RH (blue). C. Comparison plot of average and two standard deviations of GF determined with AFM area, volume, and HTDMA approaches. Error bar for HTDMA is less than the size of the data symbol. HTDMA data was collected by Armando Estillore (Grassian group, University of Iowa).91

Figure 5.2: MA dry deposition results. A. 3D AFM images of a MA particle at 5% RH and corresponding deliquesced liquid droplet at 75% RH. B. Cross section of particle at 5% RH (red) and corresponding deliquesced liquid droplet at 80% RH (blue). C. Comparison plot of average and two standard deviations of GF determined with AFM area, volume, and HTDMA approaches. HTDMA data was collected by Armando Estillore (Grassian group, University of Iowa).94

Figure 5.3: NaCl and MA dry deposition results. A. 3D AFM images of a particle at 5% RH and corresponding deliquesced liquid droplet at 80% RH. B. Cross section of particle at 5% RH (red) and corresponding deliquesced liquid droplet at 80% RH (blue). C. Comparison plot of average and two standard deviations of GF determined with AFM area, volume, and HTDMA approaches. Error bar for HTDMA is less than the size of the data symbol95

Figure 5.4: NaCl and MA wet deposition results. A. 3D AFM images of a particle at 5% RH and corresponding deliquesced liquid droplet at 76% RH. B. Phase AFM images of a particle at 5% RH and corresponding deliquesced liquid droplet at 76% RH. C. Cross section of particle at 5% RH (red) and corresponding liquid droplet at 76% RH (blue). D. Comparison plot of average and two standard deviations of GF determined with AFM area, volume, and HTDMA approaches. Error bar for HTDMA is less than the size of the data symbol. HTDMA data was collected by Armando Estillore (Grassian group, University of Iowa).97

Figure 5.5: Hydration/dehydration GF curves of NaCl obtained using single particle AFM measurements (red data) and HTDMA (blue data). Hydration curves are closed symbols and dehydration curves are open symbols. HTDMA data was collected by Olga Laskina (Grassian Group, University of Iowa).98

Figure 5.6: A. Volume GF distribution measured for 40 individual NaCl/NA particles. The data was fit to a Gaussian distribution. The red dashed line labels the GF value determined with HTDMA. Letters correspond to particles shown in B-D. B-D. The middle row of images shows dehydrated particles at 5% RH and corresponding deliquesced liquid droplets at 77% RH are shown above. The bottom row is phase images. B corresponds to the extreme left side of the distribution of GFs, while C corresponds to the most probable GF value and is representative of the majority of particles. D corresponds to the extreme right side of the GFs distribution. All scale bars are 500 nm. HTDMA data was collected by Armando Estillore (Grassian group, University of Iowa).100

Figure 6.1: Schematic example of a phase shift that can occur during tapping mode AFM imaging. The orange and blue areas on the image represent areas on the sample that are chemically or physically different and cause different phase responses compared to the phase of the drive signal.104

Figure 6.2: Phase image of SSA particles showing core-shell morphology.105

Figure 6.3: Representative AFM phase image of an SSA particle. The left images shows a typical mask surrounding the whole particle and the right shows the mask surround the particle core, used in determining organic volume fraction.106

Figure 6.4: Chlorophyll-a measurement tracking the progression of phytoplankton bloom growth. The dates analyzed are labeled on the x-axis. Chl-a concentration measured via fluorescence intensity was measured by Olga Laskina (Grassian Group, University of Iowa) and Camille Sultana (Prather Group, University of San Diego, California).108

Figure 6.5: Amplitude (top) and 3D images (bottom) of the 5 sample collection days analyzed.	108
Figure 6.6: Organic volume fraction plotted over the chlorophyll-a fluorescence intensity tracking the progression of the phytoplankton bloom. Chl-a concentration measured via fluorescence intensity was measured by Olga Laskina (Grassian Group, University of Iowa) and Camille Sultana (Prather Group, University of California, San Diego).	109
Figure 6.7: Phytoplankton bloom growth during the IMPACTS experiment was tracked by monitoring chl-a concentration (left axis). AMS data is plotted on top of chl-a trace, showing that the organic content of the aerosol increased for the first bloom but remained constant during the second bloom. Chl-a concentration measured was measured by Jon Trueblood (Grassian Group, University of Iowa) and Camille Sultana (Prather Group, University of California, San Diego). AMS Data was collected by Xiaofei Wang (Prather Group, University of California, San Diego). ¹⁵²	110
Figure 6.8: A. Representative phase image of core-shell particles collected during the experiment. B. Temporal variation of organic volume fraction for particles 0.5 – 1.0 μm in size. There is an increase in organic content of the aerosol on July 17 th that coincides with the peak of the first bloom.	111
Figure 6.9: Organic volume fraction plotted as a function of volume equivalent diameter for July 17 th sample.	111
Figure 7.1: Typical AFM force plot measurement depicts the series of events that occur during approach (grey) and retract (black) cycle of the AFM cantilever on the submicron-sized droplet. The retention force (F _{Ret}) is used to quantify the surface tension.	119
Figure 7.2: Experimental results of AFM based surface tension measurements of a ~500 nm NaCl droplet. A. 3D image of a solid NaCl crystal at 10% RH and deliquesced NaCl particle at 80% RH. B. Experimental force plot on a NaCl droplet. The approach data is in grey and the retract data is in black. C. Surface tension measurements (average and standard deviation) as a function of RH (bottom axis) and solute concentration (top axis). Predicted data is obtained from bulk solution surface tension measurements and is shown as the solid line.	123

Figure 7.3: Experimental results of AFM based surface tension measurements of GA and MA. A. 3D images of a solid GA particle at 10% RH and deliquesced GA particle at 90% RH. B,D Experimental force plots on GA (B) and MA (D) droplets. The approach data is in grey and the retract data is in black. C,E. AFM based surface tension measurements (average and standard deviation) as a function of RH (bottom axis) and solute concentration (top axis) of GA (C) and MA (F). Predicted data (solid lines) are obtained from bulk solution surface tension measurements.....124

Figure 8.1: Temporal progression of the phytoplankton bloom. Chlorophyll-a concentration is in green and AMS 43m/z data is in blue. Dashed lines correspond to the selected dates of SSA collection that were analyzed in the present work. Chl-a concentration measured was measured by Jon Trueblood (Grassian Group, University of Iowa) and Camille Sultana (Prather Group, University of California, San Diego). AMS Data was collected by Xiaofei Wang (Prather Group, University of California, San Diego).¹⁵²131

Figure 8.2: A. Representative 3D AFM image a SSA particle. B. AFM phase image of a SSA particle. The red outline gives an example of the mask used to obtain the volume of the whole particle and the blue outline gives the volume of the core. C. STXM/NEXAFS image of a singular value decomposition map obtained from using the carbon pre-edge absorbance at 278 eV and comparing with the carbon post-edge absorbance at 320 eV. Green maps primarily organic species. D. Representative NEXAFS spectrum of the carbon K edge (278-320eV) used to identify regions of organics. The spectrum shows absorbance for carboxylic acid (288.6 eV), carbonate (290.5 eV) and potassium (297 and 299 eV). E. The top image is the backscattered electron image of a representative particle. The bottom left is the EDX map of Na and the bottom left image is the EDX map of Cl. SEM/EDX data was collected by Olga Laskina at Pacific Northwest National Laboratory (Grassian Group, University of Iowa). STXM/NEXAFS data was collected by Don Pham (Moffet Group, University of the Pacific).....134

Figure 8.3: A. Organic volume fraction is plotted as a function of size. Solid line represents fit to a line (slope is $-0.25 \mu\text{m}^{-1}$) for illustrative purpose. The particles that fall in the size range for stage 6 and 7 are labeled. B. Line plots of surface tension distribution for particles on stage 6 (red) and stage 7 (blue). The inset shows individual particle measurements for each stage. AMS Data was collected by Xiaofei Wang (Prather Group, University of California, San Diego).¹⁵²136

Figure 8.4: A. Representative 3D AFM images of solid particles at low RH (left) and corresponding liquid droplets at 80% RH (right). B. Experimental force plot taken on 250nm size SSA droplet (July 13). The retention force used for quantifying surface tension is labeled. C. Line plot of surface tension distributions. The inset shows surface tension values of individual SSA droplets and the black line represents the average value...	139
Figure 8.5: A. Organic volume fraction is plotted as a function of size. Solid line represents fit to a line (slope is $-0.25 \mu\text{m}^{-1}$) for illustrative purpose. The particles that fall in the size range for stage 6 and 7 are labeled. B. Line plots of surface tension distribution for particles on stage 6 (red) and stage 7 (blue). The inset shows individual particle measurements for each stage.	141
Figure 8.6: Surface tension measurements plotted with organic volume fraction. Data points represent the mean and error bars represent standard deviation.	143
Figure 9.1: Distribution of mass spectrometry data used to assess the monodispersity and length of PEG3400.	150
Figure 9.2: A. Representative AFM image of dsDNA pillars on gold. B. Typical cross section of one dsDNA pillar.	154
Figure 9.3: A. Cartoon of control experiment; dsDNA was functionalized on mica surface with thiol exposed. Interaction force was measured with a gold tip. B. Representative force plot. C. Distribution of forces between gold tip and dsDNA.	155
Figure 9.4: Additional force-distance profile (5% of total) observed for scenario in Figure 9.3.	155
Figure 9.5: A. Pictorial representation of the control study performed; dsDNA was bound to a gold surface via the thiol end, leaving amine exposed. A gold tip was used to probe the interaction force between the DNA and tip. B. Representative force measurement. C. Distribution of forces.	156

Figure 9.6: A. Pictorial representation of the control study performed; dsDNA-DHFR was bound to a mica surface and measured against a dsDNA functionalized AFM probe. B. Two representative force measurements. The dark red (top) force plot is offset by 100pN for clarity. C. Distribution of forces. D. Approximately 10% of the force plots showed a large nonspecific adhesion event near the surface which is attributed to dsDNA interacting with the DNA or DHFR on the surface. E. Three force plots are shown simultaneously for comparative purposes. The red and purple force profiles are from the scenario where no MTX is bound the end of the probe. The green force plot is from the experiment where MTX was present on the tip.....158

Figure 9.7: Left: Scheme of DHFR immobilization on mica with dsDNA spacer: the surface cysteine of DHFR is bound via a disulfide bond to 5'-thiol-labeled dsDNA. The dsDNA is bound to mica via amine at the 5'-terminal of the complementary strand. Reprinted with permission from the Analytical Biochemistry.²³⁶ Right: 3D AFM height image of dsDNA pillars on mica surface.160

Figure 9.8: The left column shows typical force measurements (retract data only) and the right column presents distribution of rupture forces of DHFR and MTX (blue lines and bars) and MTX blocking study (red lines and bars) for the five immobilization scenarios illustrated in the inserts. Gaussian fits are shown by solid black lines. The data are summarized in Table 9.2.....162

1. INTRODUCTION

1.1 Introduction to AFM

Atomic Force Microscopy (AFM) is a high resolution imaging and force sensing microscope used to study systems at the nanoscale.¹⁻³ AFM can achieve nanometer spatial resolution in 3-dimensions (3D), making it a powerful tool for characterizing morphology of surfaces^{4,5} and nanoscopic particles. Furthermore, the technique can resolve forces as low as tens of picoNewtons, which facilitates studies for a wide range of sample applications, including the ability to measure biological interaction forces.² Force spectroscopy can be utilized to evaluate properties such as adhesion forces, sample stiffness, elasticity, and hardness, among others.⁶

Since its invention in 1986, AFM has proven to be a unique and unprecedented instrument in the microscopy field. The unique advantages include 3D imaging capabilities, versatile experimental conditions, and the ability to perform experiments at ambient pressure. The microscopy predecessor of AFM was Scanning Tunneling Microscopy (STM) that allowed atomic resolution imaging of conductive and semiconductive surfaces.⁷ AFM was developed several years later to overcome the sample limitations of STM with the additional capability to measure force and is now the most widely used type of scanning probe microscopy.⁶ AFM does not require a vacuum, unlike electron and X-ray microscopy techniques, which facilitates a wide range of experimental conditions including varying temperature,⁸ relative humidity,⁹ and performing experiments in liquid media.¹⁰ Furthermore, AFM provides sample height information and therefore, can quantify sample volume.

1.2 AFM theory of operation

AFM data is generated via a sharp tip interacting with a sample and a schematic of the instrument is illustrated in Figure 1.1. The principle of operation consists of monitoring tip-sample interactions via a cantilever containing a very sharp tip (ca. 8-10 nm), upon which a laser is focused and reflected on a position sensitive photodiode. Tip-sample interactions change the deflection of the laser on the photodiode, which is used to generate images and interpreted in force-distance curves (using Hook's Law).

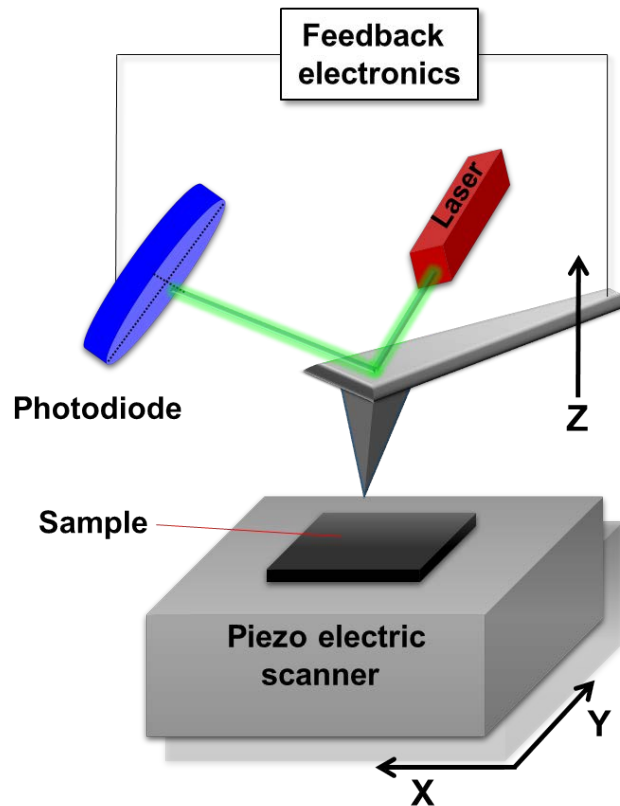


Figure 1.1: Schematic representation of AFM.

During imaging the tip is raster scanned across the sample and simultaneously adjusted in the vertical direction with piezo electronics to maintain a constant feedback.

The most common imaging modes are contact and tapping mode. Contact mode images are collected with the AFM tip directly contacting the sample, using constant force or deflection as the feedback. In tapping mode, the AFM cantilever is oscillated near its resonant frequency, tapping the sample intermittently while maintaining a preset amplitude of oscillation. Contact mode is typically used for relatively harder samples because it requires contact with the sample, while tapping mode is less abrasive and used, often times, for soft samples. In tapping mode, height, amplitude, and phase images are collected simultaneously and 3D height images can be constructed. An example of each type of image is shown in Figure 1.2.

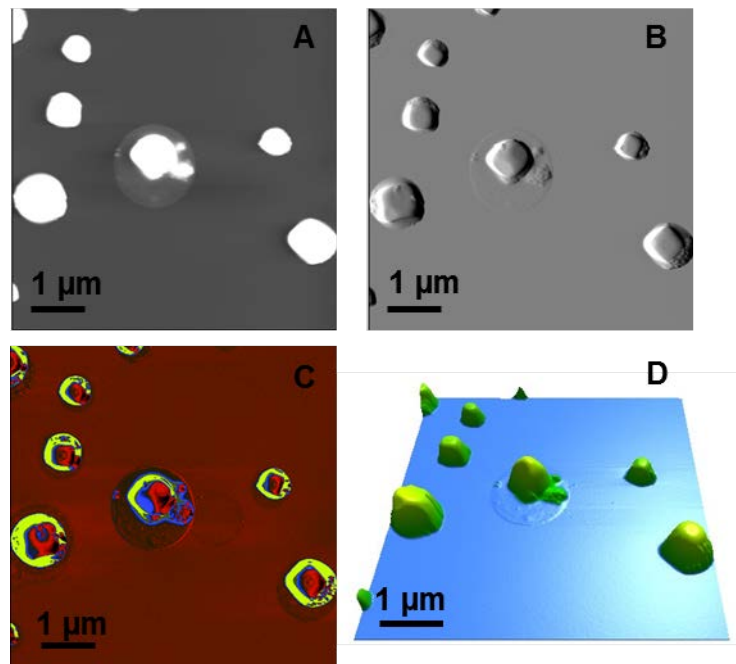


Figure 1.2: Example of tapping mode height (A), amplitude (B), phase (C), and 3D height (D) images.

Force spectroscopy experiments involve the collection and interpretation of hundreds of force-distance cycles. A typical force-distance profile is reported in Figure 1.3. Interaction force between the tip and the sample is recorded as a function of z-piezo

position, which then can be converted to tip-sample separation. The tip starts at an equilibrium distance away from the sample surface (A) and approaches the sample until it makes contact at point B. When a predefined maximum amount of force is reached, the tip retracts back away from the sample (C). At point D, the tip is held at the sample surface due to adhesion forces. Once the gradient of interaction forces becomes less or equal to the spring constant of the cantilever, the tip jumps away from the contact back to zero force (E) and returns to an equilibrium distance above the sample (F). In many applications adhesion force is quantified, which is defined as the absolute value of the difference in force when the tip jumps away from the sample and back to zero force.

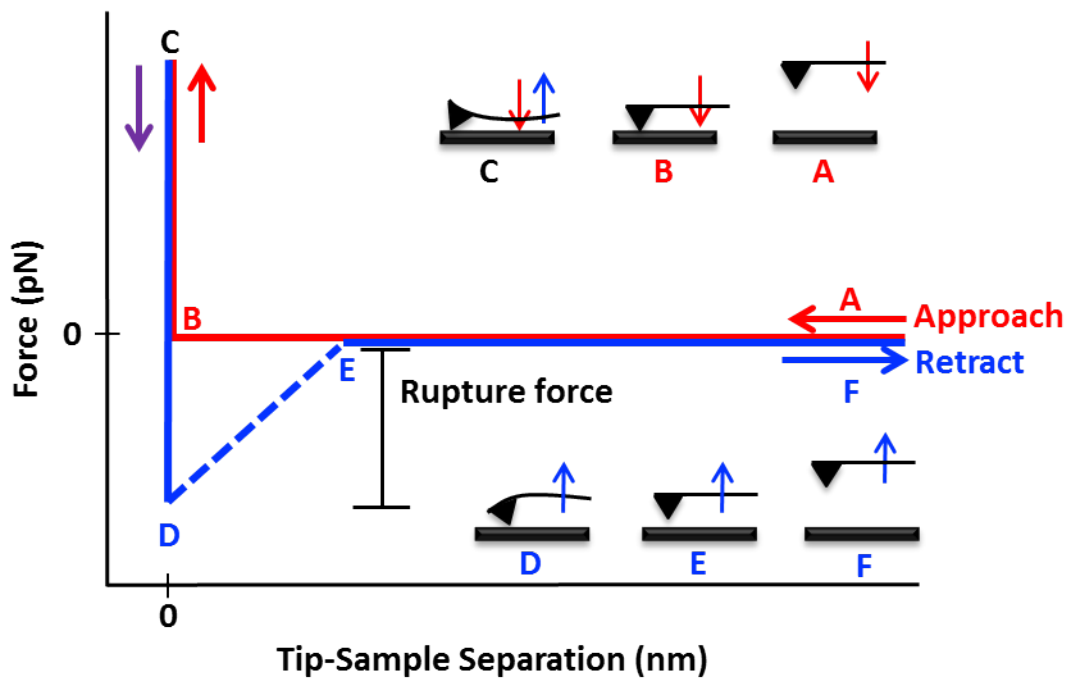


Figure 1.3: Typical force-distance cycle.

1.3 Atmospheric Aerosols

Aerosols, by definition, are liquid or solid particles suspended in gas and are microscopic, having diameters from a few nanometers up to several microns.¹¹ There are many sources of aerosols with the largest natural contributors that are dust, volcanic eruptions, sea spray, and biogenic emissions. However, anthropogenic or manmade aerosols like automobile emissions and fossil fuel burning are thought to be very important in atmospheric chemistry. Several factors including size, morphology, heterogeneous reactions, and composition dictate particles' atmospheric lifetime, which can be as short as a few minutes and as long as tens of days.¹²

Particles and liquid droplets in the atmosphere can directly interact with solar radiation (direct effect) and can nucleate cloud droplets and facilitate the formation of clouds (indirect effect) (Figure 1.4). Among all the factors that affect radiative forcing of the earth, aerosols remain one of the most poorly understood areas. The graphical representation of this uncertainty is displayed in Figure 1.5 that lists factors known to affect the earth's radiative budget and the error bars associated with the effects of aerosols are the largest.¹³ Fine (micron-sized and smaller) aerosol particles can interact strongly with solar radiation and can easily propagate around the world. Therefore, submicron size aerosol particles are thought to have a more substantial effect on atmospheric chemistry than larger particles.¹⁴ Aerosols can have both warming and cooling effects because of their diverse chemical composition and atmospheric processing, which contribute to the vast complexity of aerosol effects, making climate relevant predictions difficult. Thus, a great deal of current research is towards better

understanding the climate effects of aerosols by measuring and modeling their physical and chemical properties.

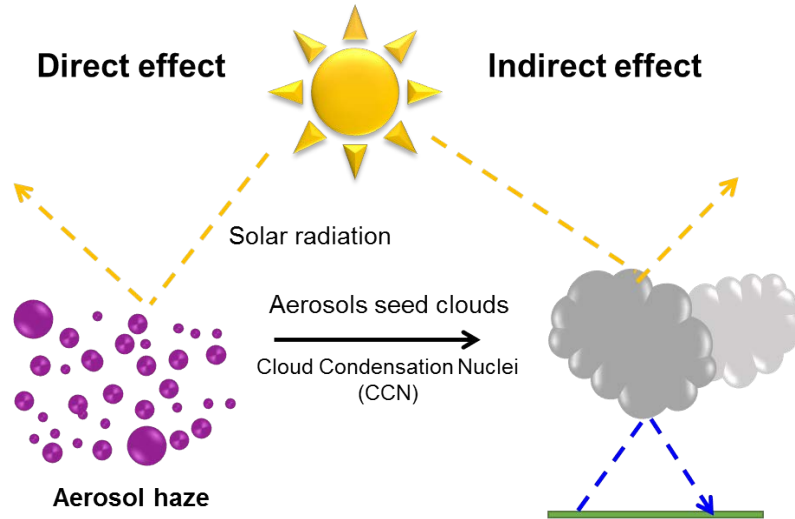


Figure 1.4: Direct and indirect effects of aerosols in the atmosphere.

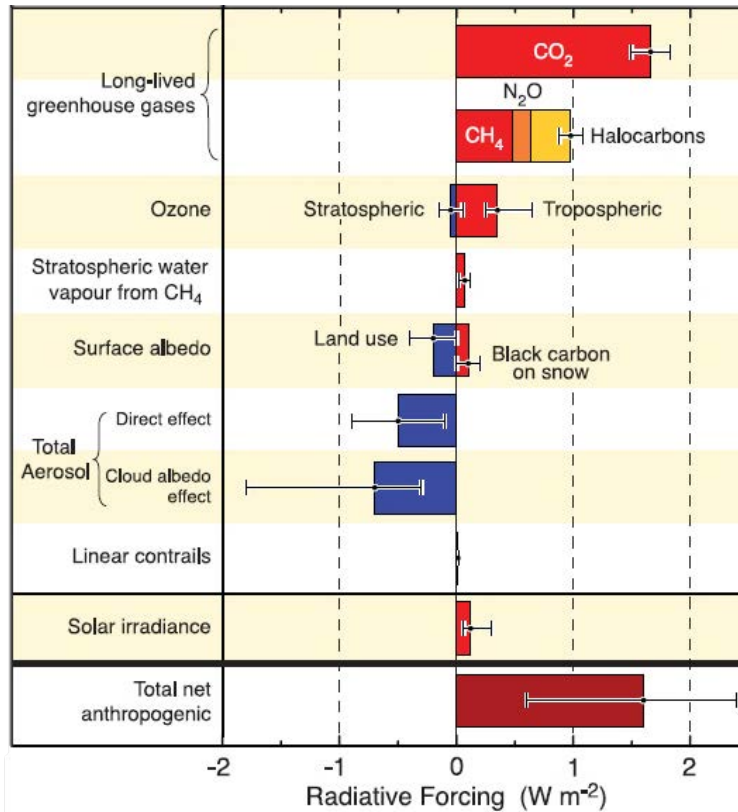


Figure 1.5: Factors affecting the radiative forcing budget of the earth.¹⁵

1.3.1 Direct effect

The direct aerosol effect refers to aerosols' ability to scatter and absorb solar radiation. It has been established that aerosols in the atmosphere can absorb short and long range solar radiation. Overall, aerosols are thought to have a cooling effect on the earth. One major chemical species responsible for radiation scattering is sulfate from biogenic emissions,¹⁶ while elemental carbon absorbs light.^{17,18}

1.3.2 Indirect effect

The indirect effect refers to aerosols' ability to act as cloud condensation nuclei (CCN) and ice nuclei (IN), which ultimately facilitate cloud formation, thus increases number of clouds, optical depth, and albedo.^{19,20} These processes affect the radiative balance of the earth by increasing reflectivity and trapping gases and radiation at the earth's surface.¹⁵ It remains poorly understood how and what type of aerosols can act as IN in the atmosphere and it's estimated that approximately one out of one million airborne particles can effectively nucleate ice.²¹

CCN is a complex process that is dictated by particle size, composition, surface tension, and hygroscopicity. Submicrometer particles act as solid surfaces that water vapor can condense onto and become cloud droplets via heterogeneous nucleation.²² One of the most commonly used theories for predicting the supersaturation relative humidity (RH) needed for cloud droplet activation is Kohler theory, which is expressed in Equation 1.1, where the droplet water vapor pressure (p_w) relative to the corresponding saturation vapor pressure over a flat surface (p^0) is calculated by the difference of two terms where M_w = molar mass of water, σ = surface tension of the droplet at the point of activation, R

= gas constant, T= temperature, D = particle diameter, ρ_w = density of water, and n_s = moles of solute.²³

$$\ln\left(\frac{p_w(D_p)}{p^0}\right) = \frac{4 M_w \sigma}{RT \rho_w D} - \frac{6 n_s M_w}{\pi \rho_w D^3} \quad (\text{Eq. 1.1})$$

Kohler theory predicts the size of aerosol particle as a function of RH based on the Kelvin effect (1st term in Equation 1.1, right side), which accounts for saturation vapor pressure over a curved surface and the Raoult effect (2nd term in Equation 1.1, right side) that takes into account the presence of a solute.²⁴ As seen in Equation 1.1, the Kelvin term is highly dependent on surface tension and the Raoult term is dictated by particle hygroscopicity, both of which will be discussed in the next two sections in more details.

1.3.3 Hygroscopicity

Hygroscopicity refers to a particle's ability to absorb water as a function of RH. Whether or not a particle contains adsorbed water dictates phase state,²⁵ morphology,²⁶ size,²⁷ extent of heterogeneous reactivity,²⁸ CCN ability,²⁹ and surface tension.⁹ Chemical composition is the main factor that determines aerosol hygroscopic properties and Figure 1.6 demonstrates how chemical composition can drastically change water uptake behavior. Figure 1.6A shows the theoretical hydration curve for sodium chloride (NaCl). NaCl does not contain any particle bound water until approximately 75% RH, upon which it deliquesces (transitions from solid to liquid) suddenly and then continuously absorbs water at a higher RH. A more soluble organic species like Malonic acid, however, has drastically different hygroscopic properties. Malonic acid continuously takes up water from low RH and is often times in the liquid or semi-solid state even at low RH (Figure 1.6B). Glutaric acid, on the other hand, is dicarboxylic acid, similar to malonic acid, but with two additional carbons, but its hygroscopic properties are similar

to that of NaCl due to lower water solubility. Research investigating how simple model systems can help elucidate the hygroscopic behavior of complex mixtures that are present in natural atmospheric aerosols is ongoing.^{25,30,31,32}

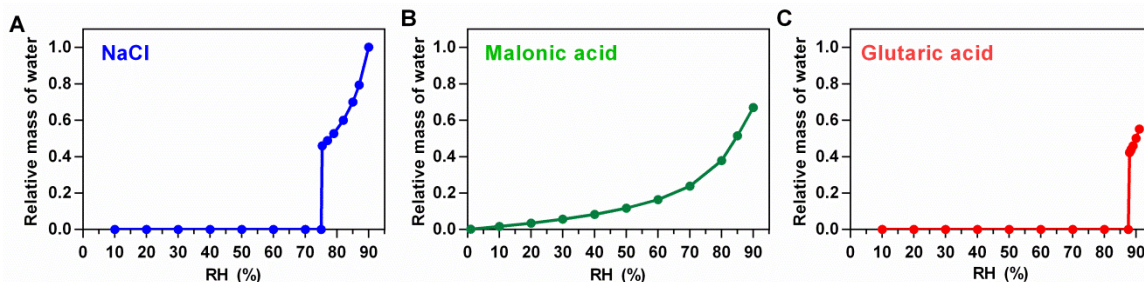


Figure 1.6: Theoretical hydration curves for (A) NaCl (B) malonic acid and (C) glutaric acid.

1.3.4 Surface tension

Surface tension of atmospheric aerosols dictates particle cloud droplet formation. Surface tension is a complex property that is influenced by various factors such as temperature,³³ chemical composition,³⁴ RH,⁹ and size.³⁵ As discussed previously, Kohler theory utilizes surface tension; however, this term is often times assumed to be the surface tension value of water, which can cause inaccuracies in predictions. Several studies^{33,36–38} have addressed the fact that organic species typically lower surface tension and inorganic species, generally, increase surface tension, and therefore, the unique chemical composition and concentration of the species in the particle is important. Furthermore, size dependent surface partitioning of surfactant molecules makes surface tension values for atmospheric aerosols difficult to predict, making it a critical area of atmospheric aerosol research.

1.4 Sea spray aerosol

Sea spray aerosol (SSA) refers to aerosol particles that are generated by the ocean. Over 70% of the earth's surface is covered with ocean, making SSA a significant source of aerosols, contributing about $10^{12} - 10^{14}$ kg of particles per year to the atmosphere.³⁹ When waves break a fine mist of water droplets is ejected into the surrounding environment. Furthermore, during wave breaking, air is entrained into the water creating bubbles and foam. When the bubbles burst at the surface film drops are ejected into the air.⁴⁰ A second event occurs when a jet of water rises in the bubble cavity after bursting, releasing jet drops.⁴¹ This process is depicted in Figure 1.7. Film drops are typically submicron in size, while jet drops are supermicron. Particles produced from these two different bubble bursting mechanisms also have different compositions. Film drops have been found to be enriched in organic species because they are produced from the bubble film, which is an air-water interface composed of amphiphilic molecules.⁴² Jet drops originate from deeper into the bulk ocean water and have been found to contain more soluble inorganic species. Because of these different bubble bursting phenomena, size-dependent chemical composition has been observed for SSA.⁴³⁻⁴⁵

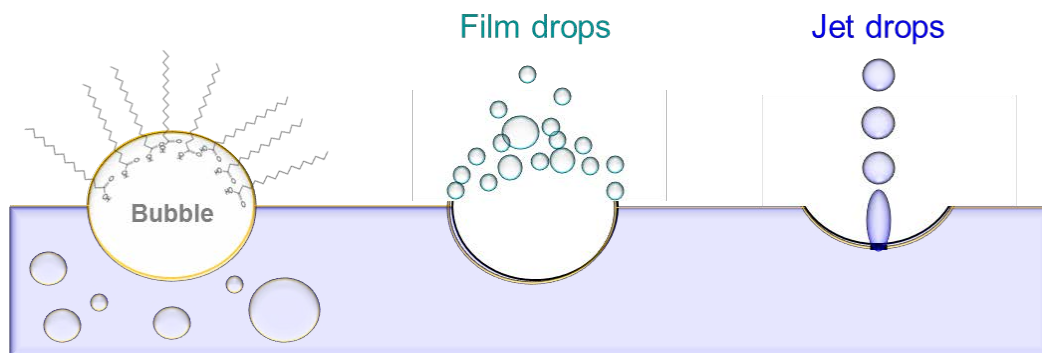


Figure 1.7: Pictorial of different bubble bursting mechanisms. Bubbles are typically enriched in organic molecules at the air-water interface. When the bubble film burst, it creates many small submicron droplets that are enriched with organic compounds. A second event occurs when a jet stream rises in the bubble cavity and produces larger jet droplets that tend to resemble more of a “bulk” water composition.

The ocean water is largely composed of inorganic salts, with sodium chloride (NaCl), being the most abundant. Magnesium, sulfur, calcium, and potassium are also common inorganic species present in sea water. Because there is a vast biological activity in the ocean, there are also many organic species and biomolecules present.^{46,47} Biomolecules include bacteria, phytoplankton, and viruses. Smaller organic species can also be produced from the degradation of these biomolecules. Current efforts in the scientific community have been directed towards identifying specific organic molecules that are present the ocean water and SSA.

Because SSA originates from the ocean water, it is a complex mixture of organic and inorganic chemicals. However, interestingly, it has been determined that SSA often times has a higher ratio of organic species relative to inorganics compared to bulk ocean water concentrations, especially those that are in the submicrometer size range. According to O’Dowd et al. the organic mass fraction of submicron SSA ranges from 15-65%, depending on the biological activity in the ocean.⁴⁸ Leck and Bigg found that SSA particles smaller than 200 nm were purely organic.⁴⁹ Organic enrichment is not

surprising when you consider that the ocean is one large air-water interface. Amphiphilic and relatively water-insoluble molecules reside at the surface of the ocean, forming the sea surface microlayer(SSML),⁵⁰ and are consequently incorporated into the emitted SSA. Insoluble molecules like palmitic acid⁵¹ and lipopolysaccharide (LPS)⁵² have been identified to be present in SSA. The composition of the particles has important implications on atmospheric processes because the physiochemical properties of organics are vastly different than inorganic species and ultimately, dictate their atmospheric and climate effects. Thus, a simplistic view of SSA being just NaCl or a mixture of inorganic species is not adequate.

1.5 Molecular recognition force spectroscopy

Investigating single-biomolecule interactions requires great precision and control over the experimental environment and is important to elucidate molecule-to-molecule properties that can be convoluted or hidden in bulk measurement responses.⁵³ The high spatial and force resolution provided by AFM, as well as the ability to perform experiments in liquid makes it an ideal technique to study single biomolecular processes.⁵ Molecular recognition force spectroscopy (MRFS) is a specific application of AFM that measures binding forces governing bio-molecular interactions, such as that between an enzyme and its inhibitor. Force is highly appropriate probe because it can be used to dynamically alter the system on a relevant scale and can be used to probe enzyme inhibitor interaction.⁵⁴ Not only can it be used to study enzyme drug interactions,⁵⁵ but also it can be used to dynamically alter the system on a relevant scale and explain motions that are important for catalysis.⁵³ It has become a powerful tool to probe the affinity and recognition properties of a variety of bio-molecular interactions since it is possible to perform experiments in liquid, which is physiologically appropriate.

The general experimental setup consists of covalently modifying the AFM tip and surface with a ligand and the receptor, respectively. Figure 1.8 depicts a typical force-distance cycle for a MRFS measurement. The modified tip approaches the enzyme functionalized surface, the ligand and receptor bind and the AFM tip measures the interaction force upon retraction. To develop appropriate experimental conditions and surface modifications, a model system of Dihydrofolate reductase (DHFR) and the drug methotrexate (MTX) was used. A series of several different linking molecules were

employed in the molecular constructs in order to increase the accuracy of the measurement and the results are discussed herein.

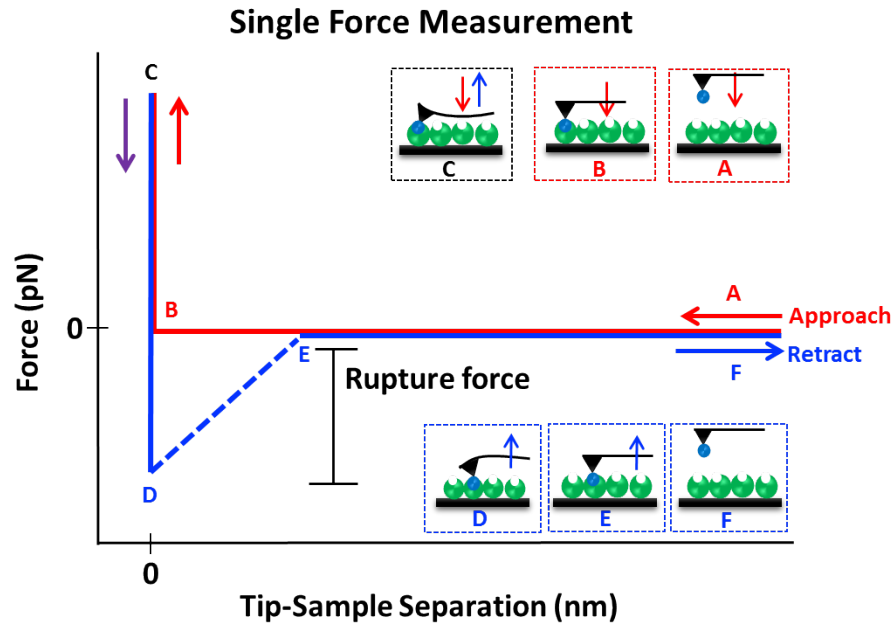


Figure 1.8: Typical force –distance cycle for a MRFS experiment.

2. EXPERIMENTAL METHODS

2.1 Aerosol generation

For AFM experiments aerosol particles are generated and collected onto solid substrates for analysis. There are several different methods of aerosol generation, which are discussed in this section.

2.1.1 Atomizer

The atomizer is one of the simplest and most common ways to create aerosol particles. In this work a TSI Inc., constant output atomizer (Model 3076) was used. A schematic of the atomizer is shown in Figure 2.1. An aqueous solution containing the species of interest is drawn up into the atomizer and encounters a stream of air, which nebulizes the solution into a fine spray. Large droplets do not make it into the aerosol stream and drain back to the closed solution reservoir and recirculate. The size distribution of particles produced by this technique is influenced by the concentration of the aqueous solution. Figure 2.2 shows aerosol size distribution for several different concentrations of NaCl solutions. Solutions prepared in this study are typically between 200 – 500 mM.

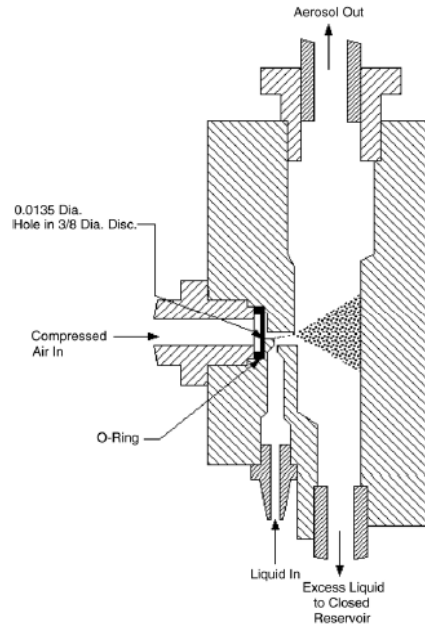


Figure 2.1: Schematic of the TSI atomizer. Adapted from TSI Inc. (Model 3076) atomizer user manual.

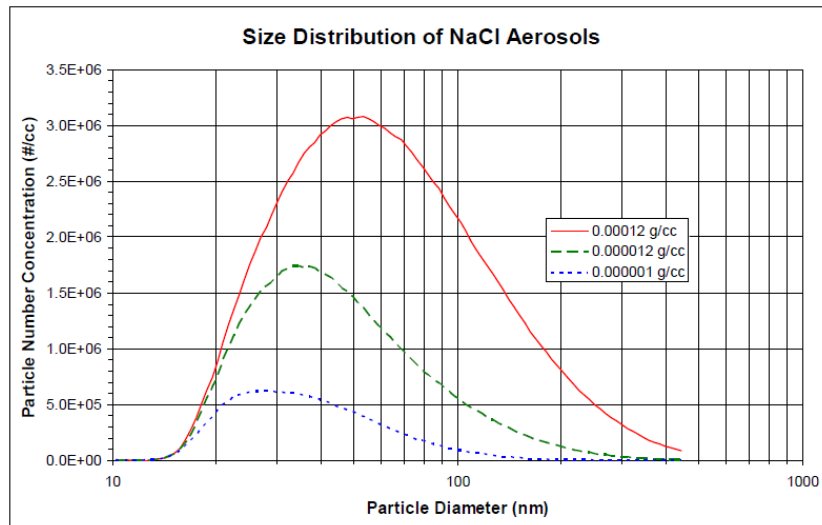


Figure 2.2: Size distribution of particles generated via atomization of NaCl from 3 different aqueous solution concentrations. Adapted from TSI Inc. (Model 3076) atomizer user manual

2.1.2 Marine aerosol reference tank

Considering the complexity of SSA particles, it was realized that the method of generating aerosols similar to that in nature is important for relevant laboratory studies. Stokes et al. developed a marine aerosol reference tank (MART) system in 2012 that mimics bubble and surface foam production similar to what occurs in the ocean (Figure 2.3). The MART consists of a 210 L Plexiglas tank and a plunging waterfall that generated the aerosol. Importantly, they show that the size distribution of particles formed with the MART tank is similar to the size distribution of breaking waves and largely different for sintered glass filter aerosol generation (Figure 2.4). Furthermore, the size distribution of particles generated by the MART tank and breaking ocean waves is larger than that produced by atomization. Thus, atomization cannot properly reproduce the size distribution of natural aerosol production which can have effects on other physiochemical properties.

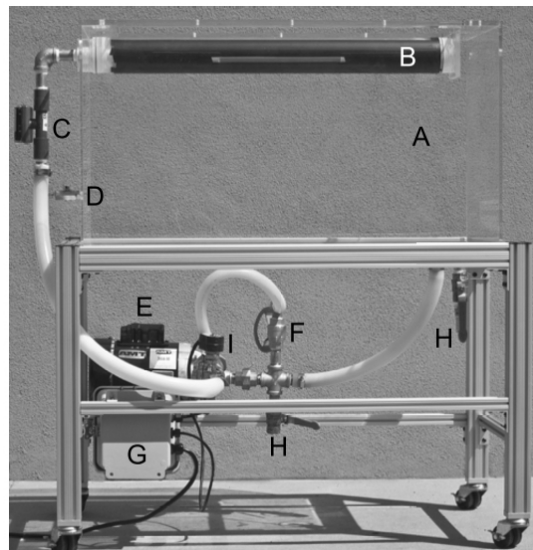


Figure 2.3: Picture of a MART tank. A. The tank. B. Spillway slot. C. Flow meter. D. Water sampling spigot. E. Pump. F. Flow control valve. G. Timing relay control box. H. Tank drain and purge valves. I. Solenoid valve. Adapted from M. D. Stokes et al. *Atmospheric Measurement Techniques* **2013**, 6, 1085.

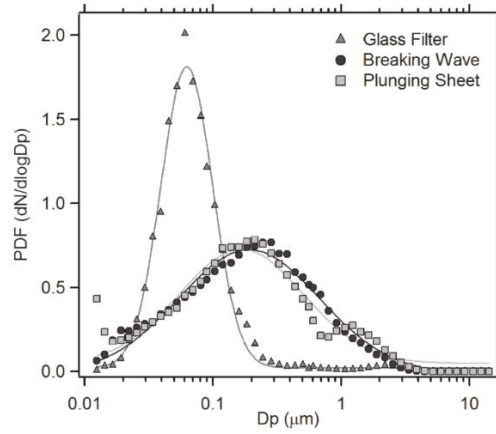


Figure 2.4: Probability density functions of SSA number distributions generated by a plunging sheet, breaking waves and sintered glass filter. Size distribution for breaking wave and plunging sheet are larger than for atomization. Adapted from M. D. Stokes et al. *Atmospheric Measurement Techniques* **2013**, 6, 1085.

2.1.3 Waveflume

Another larger scale ocean-like method of aerosol generation technique is the waveflume at the Scripps Institute of Oceanography at the University of California, San Diego.⁵⁶ The waveflume is 33 meter long tank that creates naturalistic wave action via a hydraulic pump at one end of the flume (Figure 2.5). Waves crash onto a synthetic beach about half way down and SSA is collected through ports above the wave breaking area. The airspace inside the waveflume is maintained with clean air to reduce background particle contamination.



Figure 2.5: Picture of the waveflume at the Scripps Institute of Oceanography. Adapted from Prather et al. *Proceeding of the National Academy of Science* **2013**, *10*, 7550.

2.2 Aerosol collection

After aerosol generation the particles are collected onto solid substrates for AFM analysis. The method of aerosol collection used in the majority of the studies discussed here is a Micro Orifice Uniform Deposit Impactor (MOUDI) (MSP Model 110). The MOUDI is a rotating ten stage cascade impactor that acts as a molecular sieve, separating particles from 0.056 – 18 μm in 10 different size cuts. The particle size range for the ten stages is reported in Table 2.1. A source of aerosol is presented at the inlet of the MOUDI and pulled through the steel column (seen in Figure 2.6) with a pump at a flow rate of 30 L/min. Different size particles are separated based on their aerodynamic

diameters. Heavier/larger particles impact on higher stages while smaller/lighter particles travel further down the column and impact on lower stages (Figure 2.7). Size selection is important for AFM analysis because only particles smaller than several microns in height can be readily imaged. The particles can be dried prior to entering the MOUDI by passing through a diffusion dryer (TSI, Inc. model 3062), which lowers RH in air stream to approximately 20-30%. Alternatively, the diffusion dryer can be bypassed to collect hydrated particles.

Table 2.1: MOUDI stages and corresponding size ranges.

Stage Number	Size range (μm)
1	9.9 – 1.8
2	6.2 – 9.9
3	3.1 – 6.2
4	1.8 – 3.1
5	1 – 1.8
6	0.56 - 1
7	0.33 – 0.56
8	0.18 – 0.33
9	0.092 – 0.18
10	0.055 – 0.092



Figure 2.6: Picture of MOUDI. Adapted from MSP MOUDI (Model 110) user manual.

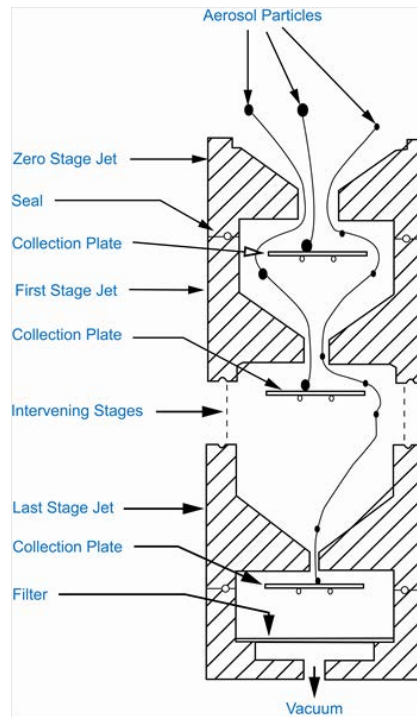


Figure 2.7: Schematic of the interior of MOUDI column detailing aerosol path and impaction. Adapted from MSP MOUDI (Model 110) user manual.

2.3 Humidity controlled AFM

The humidity in the atmosphere varies drastically depending on location, season, and temperature. For single particle studies, it is highly advantageous to perform experiments at variable RH. AFM variable RH experiments were performed with a RH cell developed by Baltrusaitis et al.⁵⁷ A schematic of the cell is shown in Figure 2.8. The cell is sealed by a rubber membrane between the AFM cantilever holder and the bottom of the cell positioned on the sample stage with adhesive tape. An air stream is passed through two flow meters – one regulating the amount of dry nitrogen and the other regulating the amount of hydrated nitrogen, pulled from the headspace of a container of water. The two streams of air mix before entering the cell, allowing the RH to be precisely controlled and measured inside the cell. This experimental setup allows the observation of single particle hydration and dehydration as a function of RH.

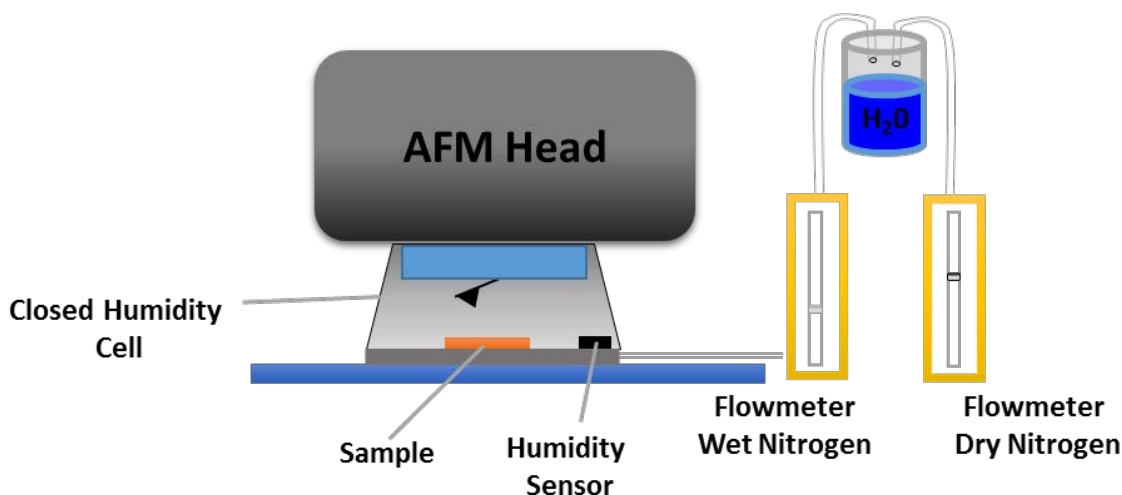


Figure 2.8: Schematic of the AFM RH cell attachment.⁵⁷ The RH of air entering the cell is controlled by two flow meters – one controlling the amount of dry air and one controlling the amount of hydrated air. The RH is measured inside the cell using humidity sensor.

3. SUBSTRATE-DEPOSITED SEA SPRAY AEROSOL PARTICLES: INFLUENCE OF ANALYTICAL METHOD, SUBSTRATE, AND STORAGE CONDITIONS ON PARTICLE SIZE, PHASE, AND MORPHOLOGY*

3.1 Abstract

Atmospheric aerosols are often times collected on substrates and analyzed weeks or months after the initial collection. Here, we investigated how the selection of substrate and microscopy method influences the measured size, phase, and morphology of sea spray aerosol (SSA) particles and have tested how different sample storage conditions affect individual particles using three common microscopy techniques: optical microscopy, atomic force microscopy, and scanning electron microscopy. The results of this study show that the microscopy techniques that operate under ambient conditions provide the most relevant and robust measurement of particle size. The sample storage in a desiccator and at ambient conditions leads to similar sizes and morphologies, while storage that involves freezing and thawing leads to irreversible changes due to phase changes and water condensation. Furthermore, micro-Raman spectra provided detailed spectroscopic information to determine possible changes in the composition and phase of stored particles. Typically, SSA particles are deposited wet and, if possible, samples used for single-particles analysis should be stored at or near conditions at which they were collected in order to avoid their dehydration. However, if samples need to be dry, as often the case, then this study found that storing particles at ambient laboratory conditions (17-

* Adapted from Laskina, O.; Morris, H. S.; Grandquist, J. R.; Estillore, A. D.; Stone, E. A.; Grassian, V. H.; Tivanski, A. V. *Environ. Sci. Technol.* Copyright (2015), 49, 13447–13453.

23% RH and 19-21°C) was effective at preserving and reducing changes that would alter data and subsequent data interpretation.

3.2 Introduction

Particle size, phase and shape are all important properties of atmospheric aerosol particles, as these properties determine the atmospheric lifetime, light scattering properties, and heterogeneous chemistry.^{56,58,59} A variety of microscopy techniques are used to image particles and determine their size, phase and shape.^{60,61} These techniques require different operating conditions and are governed by different physical principles of operation. Conventional scanning electron microscopy (SEM) and transmission electron microscopy (TEM) techniques operate under high vacuum conditions that can facilitate evaporation of semi-volatile species and lead to underestimation of a particle's size and alter composition,⁶² while atomic force microscopy (AFM) operates at ambient conditions. Microscopy techniques require particle deposition onto substrates, such as quartz, TEM grids, silicon wafers, aluminum foil, titanium foil, or filters. The choice of substrate often depends on the compatibility of the substrate with a particular measurement technique. For example, micro-Raman spectroscopy requires substrates that do not have strong Raman scattering that may interfere or obscure the signal of the analyte under consideration,⁶³ AFM requires a flat surface for accurate height measurements,⁶⁴ and for electron microscopy methods, conductive substrates are preferred.^{65,66} However, it remains to be determined whether different substrates can have an effect on the particle size and shape and, additionally, it is not clear if the different modes of operation for these techniques influence particle size determination.

Particles can grow or decrease in size upon absorbing or releasing water due to changing relative humidity (RH) and substrate deposited particles are often used to study hygroscopic properties.^{25,67-71} It has been shown that hygroscopicity of inorganic salts measured on different substrates differs depending on hydrophobicity/hydrophilicity of the substrate.⁷² In fact, the spatial distribution of organic and inorganic phases in mixed substrate deposited particles depends on the surface tension of the components and hydrophobicity/hydrophilicity of the substrates.⁷³ Specifically, hydrophobic substrates are preferred for measuring particle growth and phase transitions as a function of RH.

It is inevitable that samples collected in field studies for off-line analysis require some degree of storage. Therefore, environmental field investigations require careful consideration of the sample storage conditions.⁷⁴ Semi-volatile materials (such as ammonium nitrate, semi-volatile organic compounds and particle bound water) can be lost from the particle during sample collection, handling and storage. In addition, gas-phase organic compounds can also be adsorbed by some substrates resulting in erroneous concentrations of these species.^{75,76} Freezing of biological samples can destroy cells due to cell walls rupture by ice crystals and by freeze dehydration.⁷⁷

In this study, we collected sea spray aerosol (SSA) particles produced via a synthetic phytoplankton bloom conducted in a Marine Aerosol Reference Tank (MART)⁴⁰ on different substrates. Phytoplankton blooms are associated with enrichment of organic matter in SSA and can influence SSA properties, such as hygroscopicity.^{42,78,79} The particles were imaged using AFM, SEM and optical microscopy (OM) and duplicate samples were stored at different conditions and analyzed at different time points. Additionally, storage effects for particles composed of model compounds were also

tested and micro-Raman spectroscopy was used to determine hydration state of individual particles.

3.3 Experimental

3.3.1 Synthetic phytoplankton bloom

Seawater for the experiment was collected from the ocean surface 275 m offshore at the end of Scripps Institution of Oceanography Pier (La Jolla, CA) and filtered through a 50 μm mesh (Nitex). In order to stimulate a phytoplankton bloom collected seawater sample was augmented with Guillard's (F/2) marine water enrichment solution (Sigma Aldrich) and was continuously supplied with broad spectrum light (5700 K). Fluorescence has been measured to monitor the bloom progression (AquaFluor).

3.3.2 Sample collection and storage

Individual SSA particles were collected on substrates during a multi-week synthetic phytoplankton bloom experiment conducted in the MART system (see SI for details). These samples were collected for 30 minutes on silicon wafers (Ted Pella Inc., part no. 16008), quartz discs (Ted Pella Inc., part no. 16001-1), and silicon nitride membranes (Si_3N_4) (Silson Ltd, part no. 11401116) using the sixth stage of Micro-Orifice Uniform Deposition Impactor (MOUDI, MSP Corp. Model 110) operating at a flow rate of 30 lpm. Stage six has aerodynamic diameter range approximately between 560 and 1000 nm. The samples collected on the eleventh day of the bloom (as determined by the maximum chlorophyll fluorescence measured in the sea water) were selected to examine the quantitative differences in size and shape of substrate-deposited particles.

Storage conditions are summarized in Table 3.1. Two different storage conditions were utilized for the SSA samples. One set of samples was placed into Petri dish, sealed with Teflon tape and stored in a cardboard box at ambient laboratory conditions of 17-23% RH and 19-21°C. The second set was placed into a Petri dish, sealed with Teflon tape, placed into two zip-lock bags and stored in a freezer at -12 °C approximately 5 minutes post collection.

As a reference, a laboratory-generated standard was also prepared from 0.1 M solution of NaCl (Fisher Scientific, $\geq 99.0\%$) and malonic acid (MA, Alfa Aesar, 99.0%) in 2:1 NaCl to MA molar ratio. This molar ratio corresponds to 1:1 mass ratio that is consistent with the expected organic to inorganic mass ratio of atmospheric aerosol particles that ranges from 0.2 to 3.5.⁸⁰⁻⁸² The resulting solution was aerosolized using a constant output atomizer (TSI Inc., Model 3076), passed through a diffusion dryer (TSI Inc., Model 3062) and deposited onto stage six of a MOUDI for 5 minutes. One set of the reference samples was stored in the desiccator in addition to ambient laboratory conditions and freezer described above. Samples were placed in a desiccator in the secondary container at $0.2 \pm 0.1\%$ RH approximately 2-3 minutes after collection. Changes in the particle size distribution and morphology due to sample aging were evaluated using OM, AFM and SEM. Comparative analysis was performed at 3, 5 and 7 weeks after sample collection for SSA particles. Analysis of NaCl/MA particles was performed immediately after the sample collection and 2 and 4 weeks after the collection. The samples stored in a freezer were allowed to thaw for 2 hours at 19-21°C in their original sealed containers. The samples stored in the desiccator were allowed to equilibrate for ~15 min prior to analysis. Finally, NaCl/MA particles were collected upon

exiting the dryers for 20 min on WETSEM capsule (Quantomix, part no. QX-102) to compare the particle imaging under the vacuum environment of the SEM chamber and under ambient conditions inside of WETSEM capsule.

Table 3.1: Summary of storage conditions used in this study.

	Ambient	Freezing	Desiccator
T, °C	19-21	-12	19-21
RH, %	17-23	0.-0.3/not controlled	0.1-0.3

3.3.3 Microscopy methods

SEM images were collected using a Hitachi S-4800 Scanning Electron Microscope, with a 5 kV accelerating voltage, a 5 μ A beam current.

AFM images were obtained using a molecular force probe 3D AFM (Asylum Research, Santa Barbara, CA). Height images were collected using intermittent contact mode (AC mode) and silicon probes (MikroMasch, Model CSC37) with a nominal spring constant of 0.35 N/m. Imaging was performed at 20-21% RH. Imaging resolution of AFM is mainly dictated by the radius of curvature of the probe. The nominal radius of curvature of AFM probes used here is \sim 10 nm, significantly smaller than the particle size of 0.5 – 1.0 μ m studied.

Raman spectroscopy was performed using a LabRam HR Evolution Raman spectrometer (Horiba). The spectrometer is equipped with an Olympus BX41 optical microscope and the 100X objective lens was used to collect images at 17-23% RH in the range of 100–4000 cm^{-1} . Raman scattering was performed using a laser operating at 532

nm at 30 mW. Four exposures of 30 s each were averaged to obtain the resulting spectrum.

3.3.4 Size and shape analysis

ImageJ (National Institutes of Health) was used to measure the particle area and perimeter from images collected on SEM, AFM and OM. A statistically significant number of particles (ca 200-500 particles per sample) were analyzed for size and shape determination. Area-equivalent diameter (D_{area}) was calculated using Equation (3.1):








$$D_{area} = 2 \times \sqrt{\frac{A}{\pi}} \quad (\text{Eq. 3.1})$$

where A is the two-dimensional area within substrate plane. To quantitatively compare particle shapes from these two-dimensional images, the particle circularity (C) was determined according to Equation (3.2):

$$C = 4\pi \times \frac{A}{P^2} \quad (\text{Eq. 3.2})$$

where A is the area and P is the perimeter of the particle. Table 3.2 gives a list of different two-dimensional geometric shapes with corresponding circularity values. The circularity ranges from a value of one for a spherical particle to zero for a line. Circularity of SSA particles can be used to distinguish between sea salt particles that often form cubic structures upon crystallization and sea salt particles mixed with organic compounds that have more spherical shapes.⁴⁴

Table 3.2: Circularity parameter calculated for different two-dimensional geometric shapes.

Two-Dimensional Shape	Two-Dimensional Image	Circularity
Circle		1.000
Ellipse, axes ratio = 1:1.5		0.941
Square		0.785
Rectangle, sides ratio = 1:1.5		0.754
Ellipse, axes ratio =1:4		0.537
Rectangle, sides ratio =1:4		0.503
Line		0.000

For substrate-deposited particles studied here, aerodynamic diameter (D_{aero}) can be converted to the area equivalent diameter (D_{area}) using Equation (3.3):

$$D_{aero} = \frac{D_{area}}{\frac{1}{c} \times \sqrt{S_D \times \frac{\rho_p}{\rho_0}}} \quad (\text{Eq. 3.3})$$

where S_D is the aerodynamic shape factor, ρ_p is the particle density, and ρ_0 is unit density (1 g/cm³).⁸³ Assuming a particle density of 1.8 g/cm³,⁸⁴ circularity factor of 0.85 and

aerodynamic shape factor of 1.4,⁸³ the expected particle area equivalent diameter on stage 6 of MOUDI should be approximately 420-750 nm.

3.4 Results and Discussion

The influence of analytical method to particle size and shape was examined first. SSA particles with aerodynamic diameter of approximately 560-1000 nm (corresponding area equivalent diameter of 420-750 nm) were deposited on substrates typically used for each microscopy method (quartz for OM, silicon wafers for SEM, and silicon nitride membranes for AFM) and single particle analysis was employed to determine and compare their sizes.

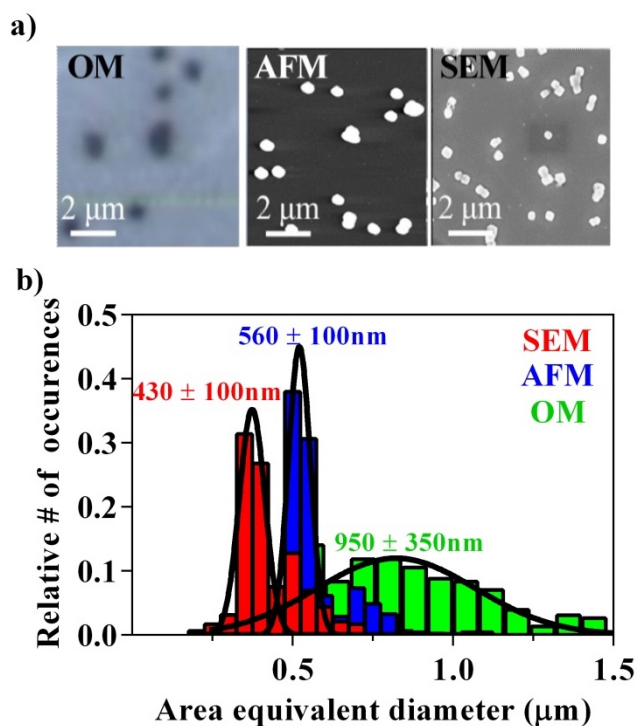


Figure 3.1: Comparison of microscopy methods on particles size and shape: a) representative OM, AFM height and SEM images of SSA particles deposited on a quartz disc, silicon nitride membrane and silicon wafer, respectively. b) Histograms of area equivalent diameters for three microscopy methods with corresponding mean and standard deviation values. OM data was collected by Olga Laskina (Grassian group, University of Iowa) SEM data was collected by Josh Grandquist (Grassian group, University of Iowa).

Representative OM, AFM and SEM images of SSA particles are shown in Figure 3.1. The size analysis performed on hundreds of individual particles (see SI for details) returned mean (\pm one standard deviation) area equivalent diameters for these methods as 950 ± 350 nm (OM), 560 ± 100 nm (AFM) and 430 ± 100 nm (SEM), while the expected area equivalent size range for these particles is 420-750 nm. Determined circularity values were similar between OM (0.88 ± 0.1) and AFM (0.89 ± 0.11), and lower for SEM (0.78 ± 0.12), where the difference can be attributed to vacuum conditions of SEM, as discussed below. Thus, the AFM results appear to provide the particle size closest to the expected range and the results are all statistically different than each other (within 95% confidence interval). Significantly larger sizes observed with OM relative to the AFM are attributed to the diffraction-limited resolution of OM. The resolution limit of the OM used here is in the range of 300-500 nm that overlaps with the expected particle area equivalent diameters of 420-750 nm, giving rise to the apparent size increase observed here.

The smaller particle size observed with SEM likely arises from dehydration of the particles upon subjecting them to vacuum conditions. This can be avoided by encapsulating samples under ambient conditions and as seen in the images in Figure 3.2. The experiment clearly indicates that particles exposed to vacuum conditions are becoming smaller in size and less circular, which is consistent with the lower circularity observed with SEM under vacuum conditions as compared with the ambient OM and AFM methods. The result underscores the importance of utilizing analytical methods under ambient conditions and avoiding subjecting particles to vacuum conditions, when possible.

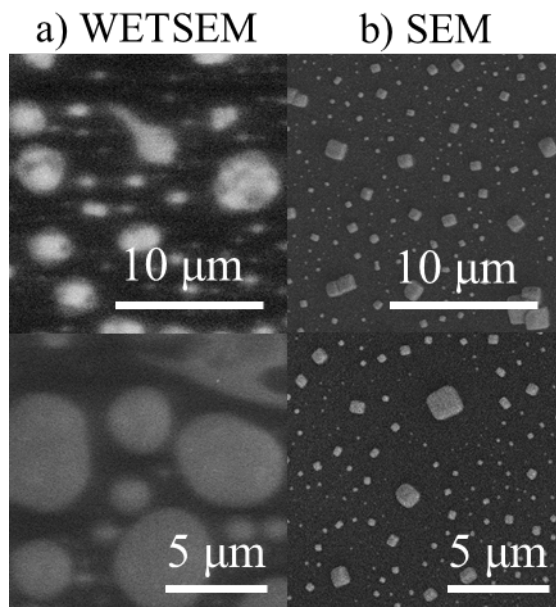


Figure 3.2: SEM images of particles collected from NaCl/malonic acid mixture on WETSEM capsule and imaged a) captured inside the WETSEM capsule under 15-20% RH and ambient pressure and b) under vacuum conditions. SEM data was collected by Josh Grandquist (Grassian group, University of Iowa).

Substrate effects were examined next using AFM as a comparison method. Representative AFM height images of SSA particles deposited on a silicon nitride, silicon and quartz substrates are shown in Figure 3.3. Analysis of hundreds of individual particles for each substrate yielded mean (\pm one standard deviation) area equivalent diameters and circularity factors of 650 ± 100 nm and 0.89 ± 0.11 , 630 ± 190 nm and 0.85 ± 0.15 , 600 ± 180 nm and 0.86 ± 0.11 for silicon nitride, silicon and quartz substrates, respectively. Thus, both circularity and area-equivalent diameter values of SSA particles determined from AFM measurements for the different substrates are statistically similar and determined sizes fall into the expected range of 420-750 nm. Hence, we can conclude for these types of particles, selection of a substrate does not appear to influence their size and morphology.

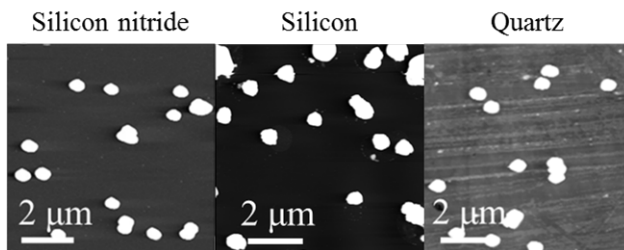


Figure 3.3: Representative AFM height images of SSA particles deposited on silicon nitride, silicon and quartz substrates showing similar morphology and size range.

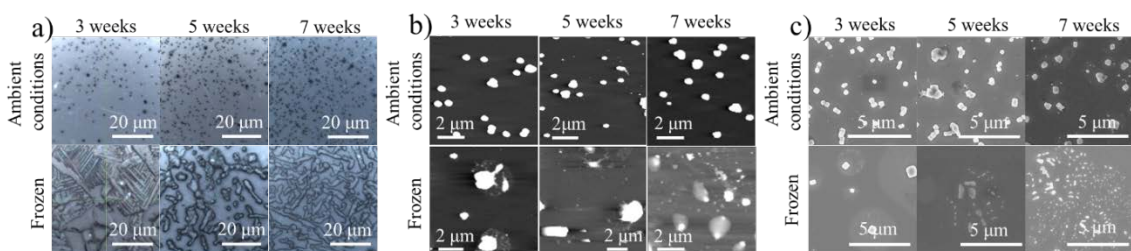


Figure 3.4: a) OM, b) AFM, c) SEM images of sea spray aerosol particles stored under ambient laboratory conditions (top) and frozen at -12°C (bottom). Images were collected 3, 5 and 7 weeks after particle collection. OM data was collected by Olga Laskina (Grassian group, University of Iowa) SEM data was collected by Josh Grandquist (Grassian group, University of Iowa).

We next turned to quantitatively examine how storage conditions influence particle size and morphology. Figure 3.4 shows representative images for each analysis type of SSA particles stored under ambient laboratory conditions and frozen at -12°C collected 3, 5, and 7 weeks after initial particle collection. Distributions of circularity factors and histograms of area equivalent diameter obtained from single particle analysis are shown in Figure 3.5, and Figure 3.6, 3.7, and 3.8, respectively and averaged values reported in Table 3.3. The number of SSA particles analyzed is given in Table 3.4 (200-700 per sample). Figure 3.9 shows a graphical representation of mean area equivalent diameters and their standard deviations for SSA particles determined using each microscopy methods under different storage conditions.

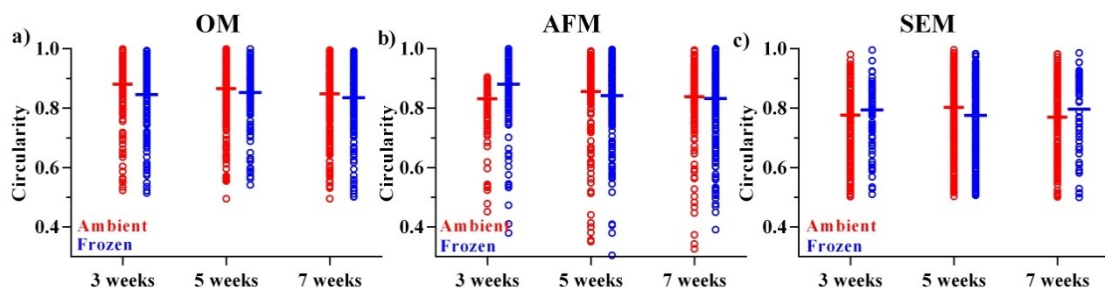


Figure 3.5: Circularity of SSA particles determined using OM (a), AFM (b) and SEM (c) 3, 5 and 7 weeks after particle collection at different storage conditions. The horizontal line represents the average value of the data set. OM data was collected by Olga Laskina (Grassian group, University of Iowa) SEM data was collected by Josh Grandquist (Grassian group, University of Iowa).

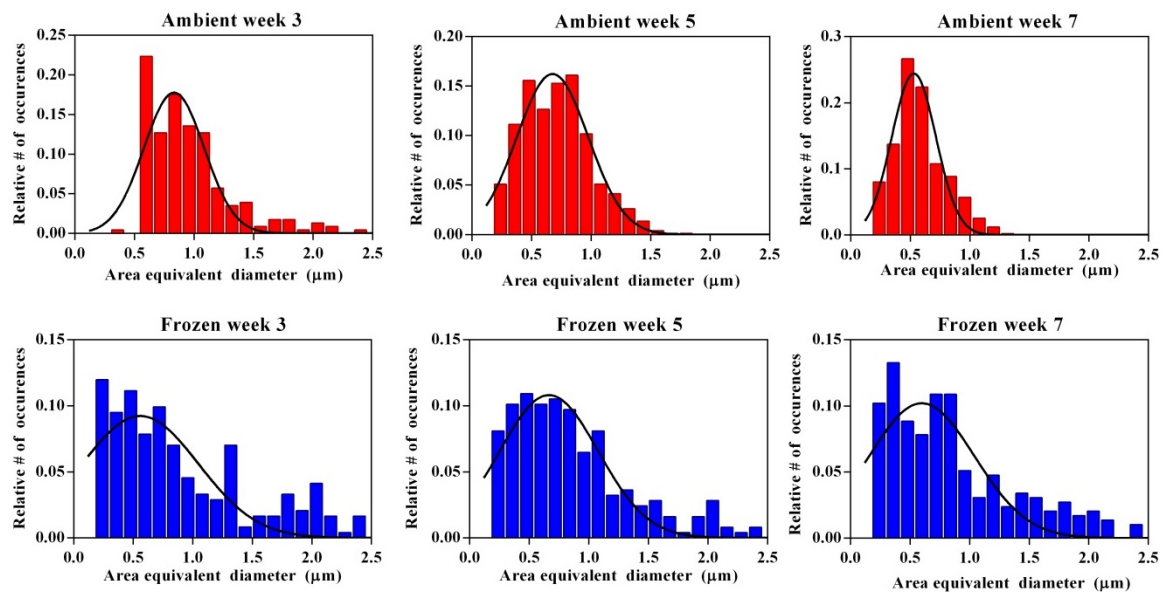


Figure 3.6: Area equivalent diameter histograms of SSA particles as probed using OM 3, 5 and 7 weeks after particle collection at different storage conditions. OM data was collected by Olga Laskina (Grassian group, University of Iowa) SEM data was collected by Josh Grandquist (Grassian group, University of Iowa).

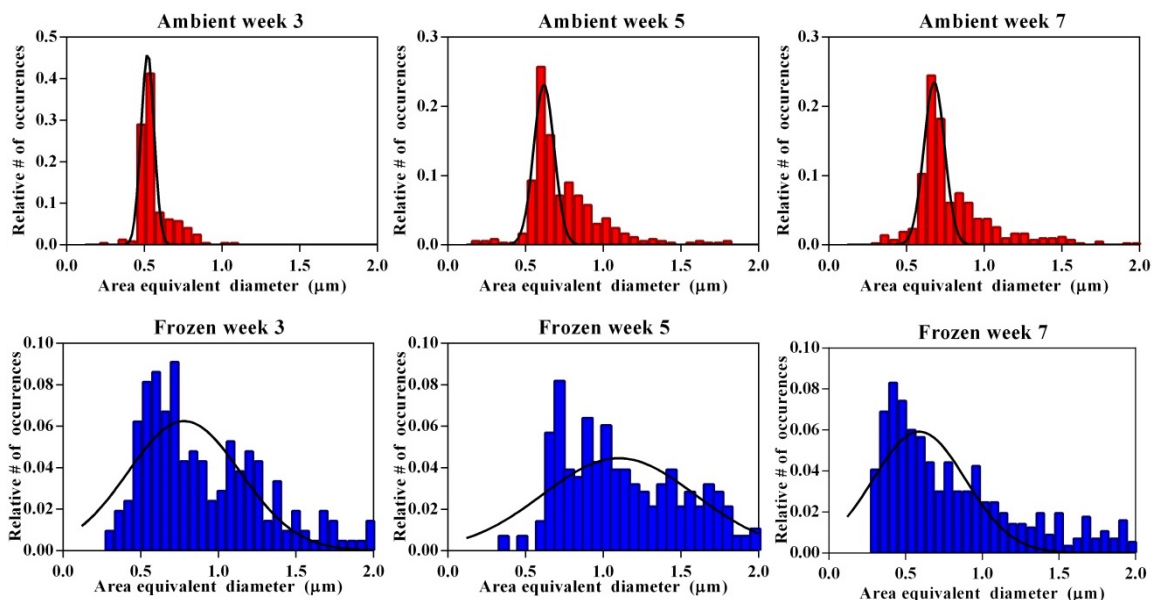


Figure 3.7: Area equivalent diameter histograms of SSA particles as probed using AFM 3, 5 and 7 weeks after particle collection at different storage conditions. OM data was collected by Olga Laskina (Grassian group, University of Iowa) SEM data was collected by Josh Grandquist (Grassian group, University of Iowa).

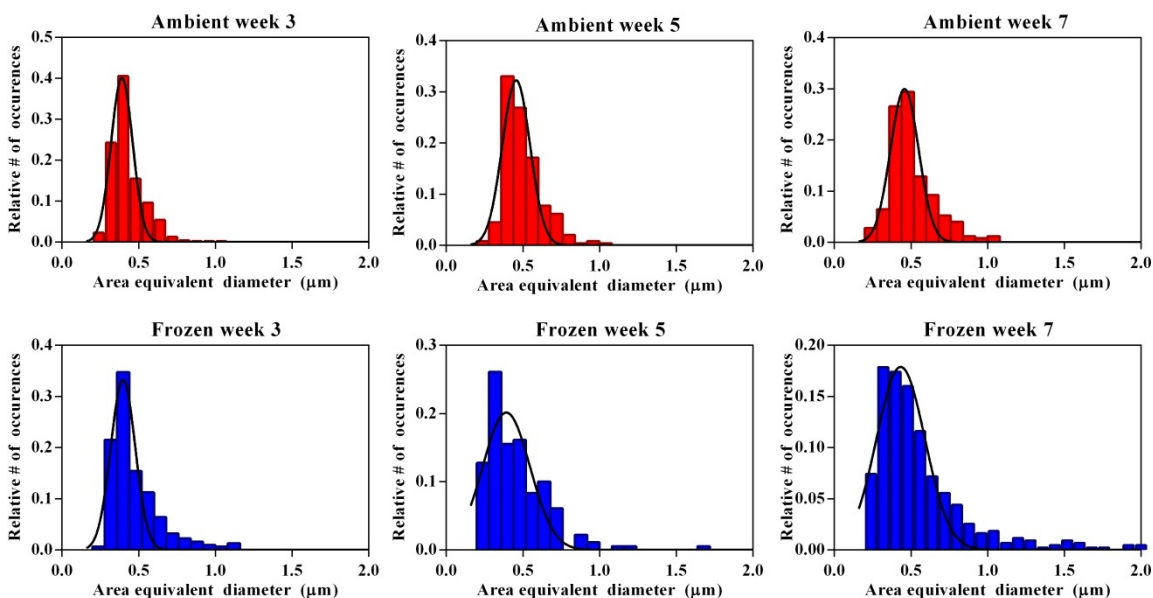


Figure 3.8: Area equivalent diameter histograms of SSA particles as probed using SEM 3, 5 and 7 weeks after particle collection at different storage conditions. OM data was collected by Olga Laskina (Grassian group, University of Iowa) SEM data was collected by Josh Grandquist (Grassian group, University of Iowa).

Table 3.3: Average and standard deviation of the area equivalent diameter and circularity measured for SSA particles analyzed using OM, AFM and SEM in 3, 5 and 7 weeks after particle collection at ambient and frozen storage conditions. OM data was collected by Olga Laskina (Grassian group, University of Iowa) SEM data was collected by Josh Grandquist (Grassian group, University of Iowa).

		Ambient		Frozen	
		diameter(μm)	circularity	diameter(μm)	circularity
OM	3 weeks	0.95 ± 0.35	0.88 ± 0.10	1.06 ± 0.79	0.85 ± 0.11
	5 weeks	0.71 ± 0.35	0.87 ± 0.11	0.99 ± 0.77	0.85 ± 0.10
	7 weeks	0.58 ± 0.21	0.86 ± 0.11	1.02 ± 0.87	0.84 ± 0.11
AFM	3 weeks	0.56 ± 0.10	0.83 ± 0.07	0.96 ± 0.47	0.88 ± 0.11
	5 weeks	0.74 ± 0.24	0.86 ± 0.14	1.37 ± 0.67	0.84 ± 0.13
	7 weeks	0.81 ± 0.32	0.84 ± 0.12	1.24 ± 1.41	0.83 ± 0.13
SEM	3 weeks	0.43 ± 0.10	0.78 ± 0.12	0.47 ± 0.16	0.79 ± 0.11
	5 weeks	0.49 ± 0.12	0.80 ± 0.13	0.46 ± 0.16	0.78 ± 0.13
	7 weeks	0.51 ± 0.15	0.77 ± 0.13	0.56 ± 0.31	0.80 ± 0.13

Table 3.4: The number of SSA particles analyzed using OM, AFM and SEM in 3, 5 and 7 weeks after particle collection at different storage conditions. OM data was collected by Olga Laskina (Grassian group, University of Iowa) SEM data was collected by Josh Grandquist (Grassian group, University of Iowa).

OM - ambient			AFM - ambient			SEM - ambient		
week 3	week 5	week 7	week 3	week 5	week 7	week 3	week 5	week 7
228	726	510	245	366	429	478	245	248
OM - frozen			AFM - frozen			SEM - frozen		
week 3	week 5	week 7	week 3	week 5	week 7	week 3	week 5	week 7
242	247	294	209	281	566	311	180	431

Collectively, results clearly show that the particles stored in the freezer and thawed under ambient laboratory conditions undergo substantial morphological changes. Specifically, frozen particles become significantly larger and agglomerate, likely the result of water condensation on particles during sample thawing and/or freezing. Quantitative size analysis supports this conclusion, as shown in Figure 3.9. Mean area equivalent diameters and their standard deviations of samples stored in the freezer are larger than of those stored in ambient laboratory conditions. Although the shape of the

particles changes significantly, this does not have a large effect on the average value of circularity factor, however, the circularity values shown in Figure 3.5 show a broader range for the frozen samples for OM and AFM, compared to the ones stored in ambient laboratory conditions. The presence of both large spherical single particles with high circularity factor and agglomerates with low circularity factor leads to a broader distribution of circularities, while the average circularity value remains approximately constant.

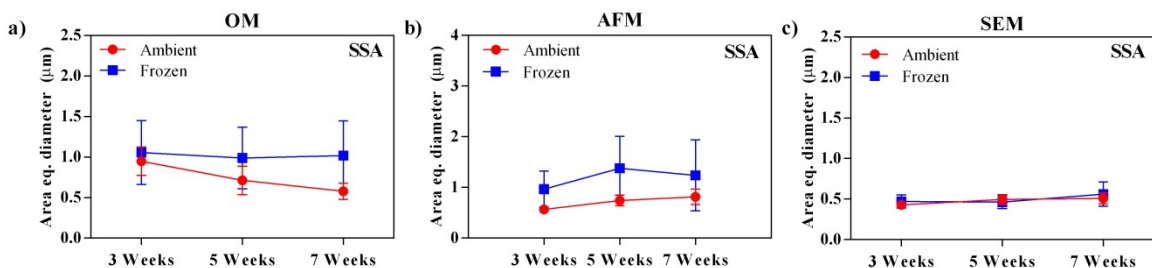


Figure 3.9: Comparison of mean area equivalent diameters of SSA particles determined using OM (a), AFM (b) and SEM (c) in 3, 5 and 7 weeks after particle collection at ambient and frozen storage conditions. The error bars correspond to one standard deviation. OM data was collected by Olga Laskina (Grassian group, University of Iowa) SEM data was collected by Josh Grandquist (Grassian group, University of Iowa).

Some particles stored under frozen conditions have residues surrounding them (Figure 3.4, middle images) that are not apparent for particles stored at ambient conditions. This low height residue might be indicative of phase separation, driven by solubility difference and the freeze-thaw cycle. This could lead to inaccurate interpretation of particle heterogeneity for single particle analysis. However, for techniques that extract the aerosol for bulk analysis, this may not be an issue since freezing and thawing does not necessarily promote compositional changes.

Interestingly, particle size and shape as analyzed by SEM (Figures 3.8 and 3.9) suggest no size and shape change in any of the storage conditions probed. Once subjected

to vacuum, the particles dehydrate to approximately their original size but there is a residue surrounding them, similar to the one observed by AFM (Figure 3.4). The more freeze cycles the sample undergoes effects the severity of the agglomeration and subsequent effect of dehydration, as can be seen in the images taken after 5 and 7 weeks (Figure 3.4). Ultimately, while frozen particles are, in fact, undergoing changes relative to particles stored at ambient conditions, average area equivalent sizes are similar due to vacuum dehydration effects.

To complement the data shown for SSA samples, a model SSA system represented by a mixture of NaCl/malonic acid (NaCl/MA) at various time points following being stored under different conditions. Figure 3.10 shows representative images for each analysis type of NaCl/MA particles stored under ambient laboratory conditions, under desiccator and frozen at -12°C . Images were obtained for particles as prepared (0 weeks), 2 and 4 weeks after initial particle collection and histograms for the area equivalent diameters and distributions of circularity factors obtained from single particle analysis are shown in Figures 3.11-3.13 and Figure 3.14, respectively, and their averaged values are reported in Table 3.5. Figure 3.15 shows mean area equivalent diameters of NaCl/malonic acid particles determined using each microscopy methods under different storage conditions. The numbers of particles analyzed are given in Table 3.6 (170-500 per sample).

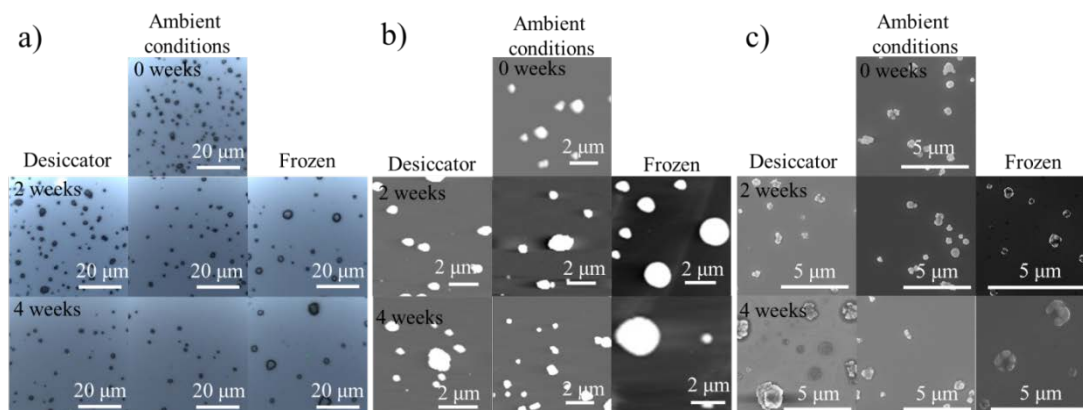


Figure 3.10: a) OM, b) AFM, c) SEM images of particles collected from NaCl/malonic acid stored in desiccator, under ambient laboratory conditions, and frozen at -12°C . Images were acquired right after particle collection, 2 and 4 weeks later. OM data was collected by Olga Laskina (Grassian group, University of Iowa) SEM data was collected by Josh Grandquist (Grassian group, University of Iowa).

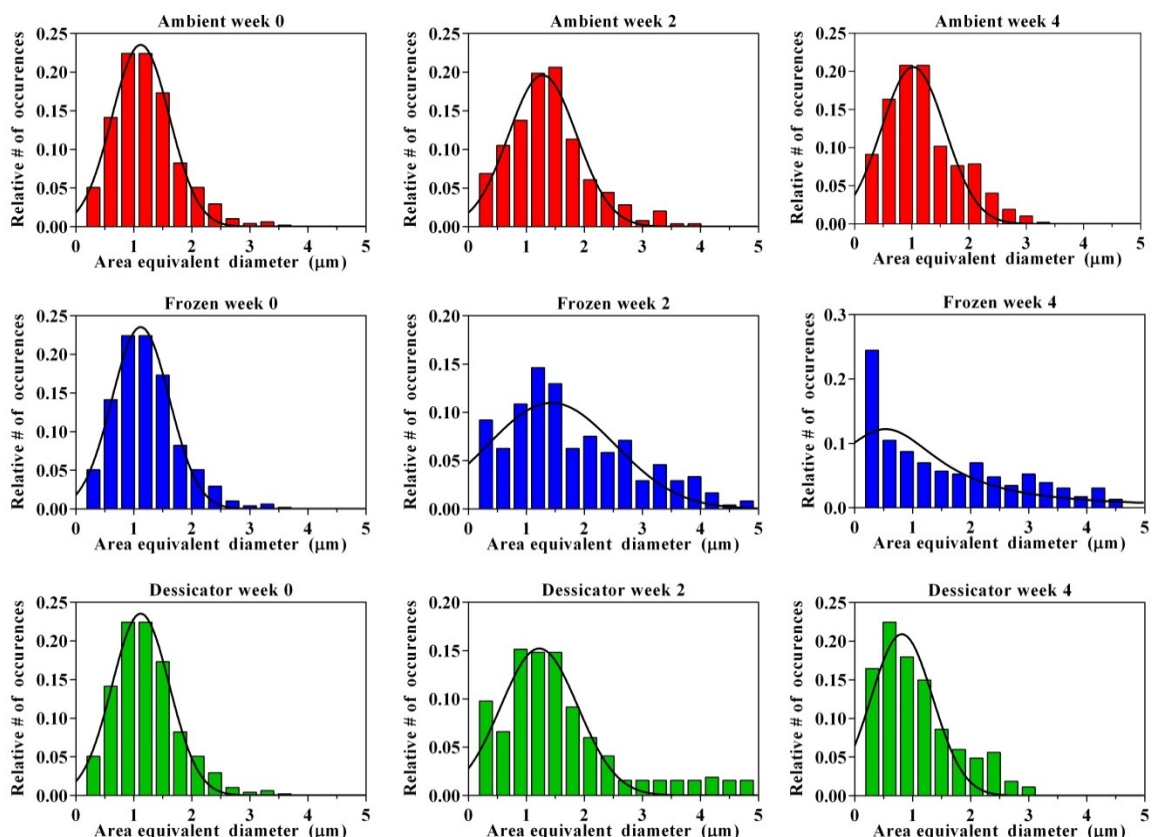


Figure 3.11: Area equivalent diameter histograms of NaCl/MA particles as probed using OM 0, 4 and 2 weeks after particle collection at different storage conditions. OM data was collected by Olga Laskina (Grassian group, University of Iowa) SEM data was collected by Josh Grandquist (Grassian group, University of Iowa).

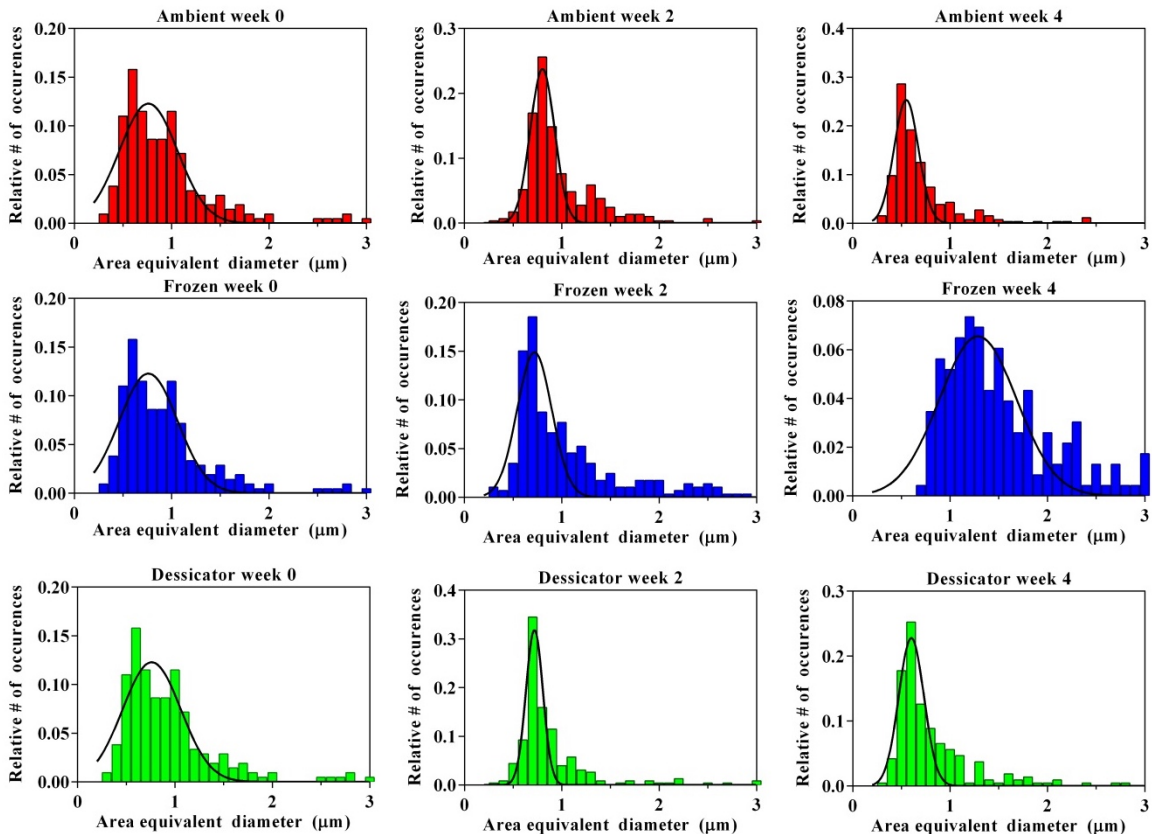


Figure 3.12: Diameter histograms of NaCl/MA particles as probed using AFM 0, 2 and 4 weeks after particle collection at different storage conditions. OM data was collected by Olga Laskina (Grassian group, University of Iowa) SEM data was collected by Josh Grandquist (Grassian group, University of Iowa).

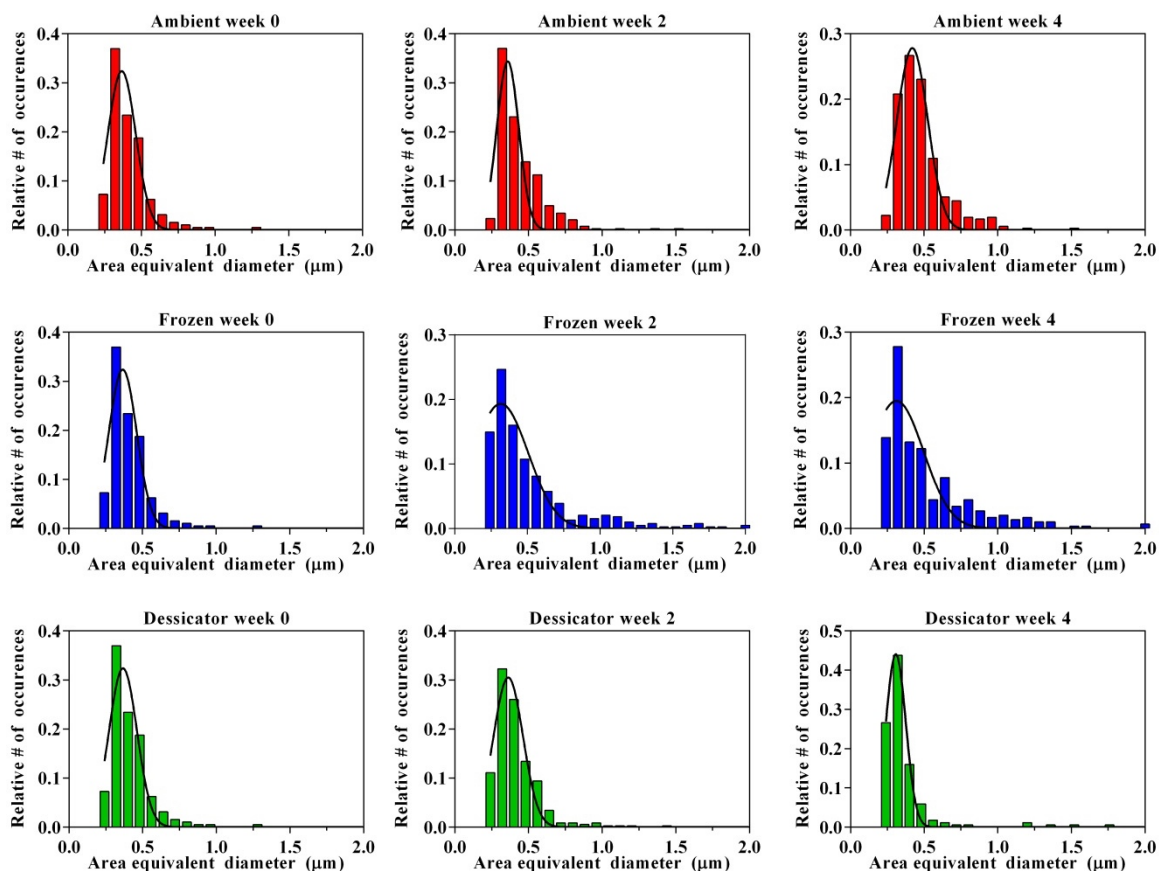


Figure 3.13: Diameter histograms of NaCl/MA particles as probed using SEM 0, 2 and 4 weeks after particle collection at different storage conditions. OM data was collected by Olga Laskina (Grassian group, University of Iowa) SEM data was collected by Josh Grandquist (Grassian group, University of Iowa).

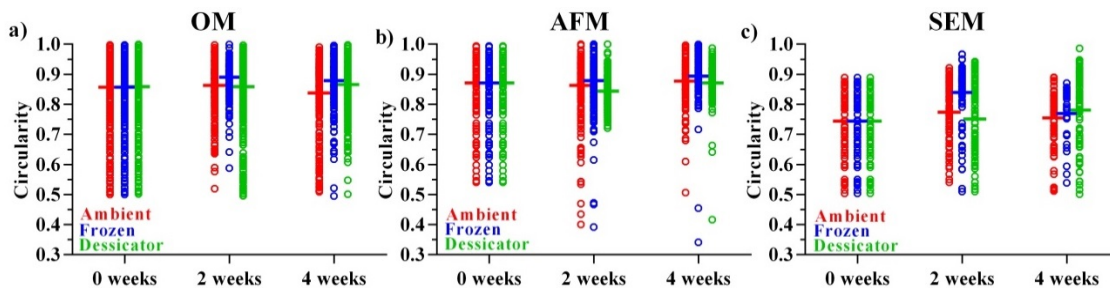


Figure 3.14: Circularity of NaCl/MA particles determined using OM (a), AFM (b) and SEM (c) in 0, 2 and 4 weeks after particle collection at different storage conditions. The horizontal line represents the average of the data set. OM data was collected by Olga Laskina (Grassian group, University of Iowa) SEM data was collected by Josh Grandquist (Grassian group, University of Iowa).

Table 3.5: Average and standard deviation of the area equivalent diameter and circularity measured for NaCl/malonic acid particles analyzed using OM, AFM and SEM as prepared, 2 and 4 weeks later stored at ambient, frozen and desiccator storage conditions. OM data was collected by Olga Laskina (Grassian group, University of Iowa) SEM data was collected by Josh Grandquist (Grassian group, University of Iowa).

	Ambient		Frozen		Desiccator	
	diameter (μm)	circularity	diameter (μm)	circularity	diameter (μm)	circularity
OM						
0 weeks	1.22 ± 0.56	0.86 ± 0.12	1.22 ± 0.56	0.86 ± 0.12	1.22 ± 0.56	0.86 ± 0.12
2 weeks	1.39 ± 0.69	0.86 ± 0.08	1.89 ± 1.27	0.89 ± 0.06	1.84 ± 1.42	0.86 ± 0.12
4 weeks	1.20 ± 0.63	0.84 ± 0.12	1.78 ± 1.54	0.88 ± 0.08	1.09 ± 0.67	0.86 ± 0.09
AFM						
0 weeks	0.96 ± 0.54	0.87 ± 0.10	0.96 ± 0.54	0.87 ± 0.10	0.96 ± 0.54	0.87 ± 0.10
2 weeks	0.98 ± 0.42	0.86 ± 0.10	1.26 ± 1.05	0.88 ± 0.10	0.89 ± 0.43	0.84 ± 0.06
4 weeks	0.75 ± 0.53	0.87 ± 0.08	2.73 ± 2.41	0.89 ± 0.11	0.83 ± 0.47	0.87 ± 0.06
SEM						
0 weeks	0.41 ± 0.14	0.74 ± 0.10	0.41 ± 0.14	0.74 ± 0.10	0.41 ± 0.14	0.74 ± 0.10
2 weeks	0.44 ± 0.16	0.76 ± 0.10	0.57 ± 0.40	0.86 ± 0.09	0.41 ± 0.16	0.75 ± 0.12
4 weeks	0.48 ± 0.17	0.75 ± 0.09	0.52 ± 0.30	0.76 ± 0.09	0.38 ± 0.25	0.78 ± 0.12

Table 3.6: The number of NaCl/malonic acid particles analyzed using OM, AFM and SEM as prepared, 2 and 4 weeks later at different storage conditions. OM data was collected by Olga Laskina (Grassian group, University of Iowa) SEM data was collected by Josh Grandquist (Grassian group, University of Iowa).

OM - ambient			AFM - ambient			SEM - ambient		
week 0	week 2	week 4	week 0	week 2	week 4	week 0	week 2	week 4
473	247	471	209	289	255	192	381	356
OM - frozen			AFM - frozen			SEM - frozen		
week 0	week 2	week 4	week 0	week 2	week 4	week 0	week 2	week 4
473	239	229	209	286	231	456	454	332
OM - desiccator			AFM - desiccator			SEM - desiccator		
week 0	week 2	week 4	week 0	week 2	week 4	week 0	week 2	week 4
473	317	267	209	226	214	192	350	169

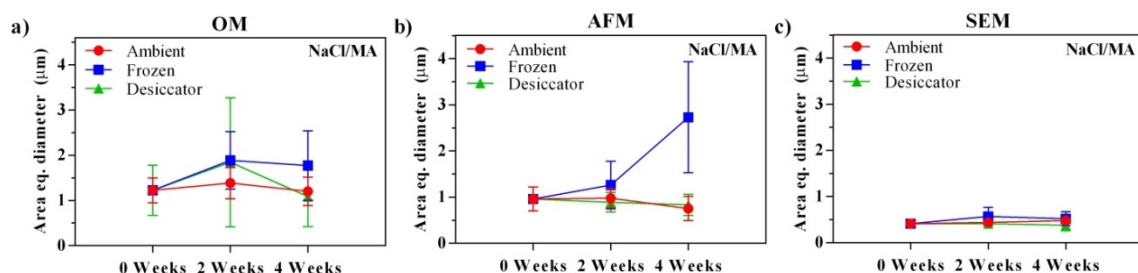


Figure 3.15: Comparison of mean area equivalent diameters of NaCl/malonic acid particles determined using OM (a), AFM (b) and SEM (c) as prepared, 2 and 4 weeks later stored at ambient, frozen and desiccator storage conditions. The error bars correspond to one standard deviation. OM data was collected by Olga Laskina (Grassian group, University of Iowa) SEM data was collected by Josh Grandquist (Grassian group, University of Iowa).

Overall, the results are similar as what was found for more chemically complex SSA particles discussed above. The particles stored in ambient laboratory conditions and desiccator do not change significantly in size or shape a month after collection, but particles stored in the freezer and then thawed prior to analysis are significantly larger than other samples both at 2 and 4 weeks after collection. These results are also supported by the broader distribution seen in Figures 3.11 – 3.13. As discussed above, this is likely due to water uptake by particles upon thawing. The circularity of particles stored under different conditions is similar, consistent with the results observed for SSA above. We note the storage under desiccator does not appear to provide any statistically significant improvements over ambient storage, hence later is recommended from a practical prospective. Finally, SEM data indicates no difference between different storage methods in terms of variation in size due to vacuum exposure of the technique coupled with dehydration of particles, as the discussed above.

To further illustrate the difference between the storage methods, AFM 3-D imaging capabilities were utilized to compare changes in both particle area-equivalent diameter and height. Figure 3.16 shows how height of individual particles changes with

respect to the corresponding area equivalent diameter for SSA particles stored for 7 weeks under ambient and frozen conditions, and NaCl/MA particles stored for 4 weeks at ambient, frozen and desiccator storage conditions. Each plot was fit to a linear function, which returns slope of 0.43 and 0.34 for the SSA particles at ambient and frozen storages, respectively, while 0.45, 0.40 and 0.19 for the NaCl/MA particles at ambient, desiccator and frozen storages, respectively. Significantly lower slope values observed for the samples stored under frozen storage conditions, once again, support our conclusion that it induces significant morphological changes that lead to hydration of stored particles, which in turn increases their spreading over the surface, as indicated by the decrease in the measured slopes.

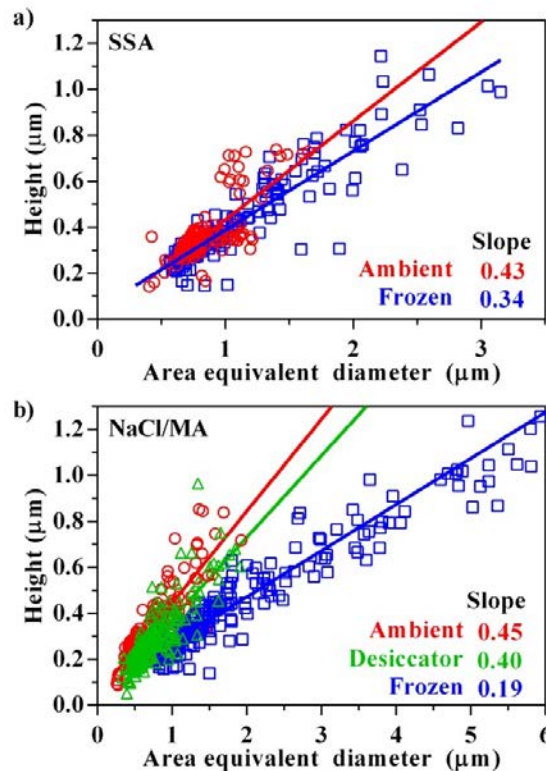


Figure 3.16: Particle height plotted as a function of area equivalent diameter analyzed for a) week 7 SSA particles and b) week 4 NaCl/MA particles. Symbols are individual particles data, while solid lines are linear fits.

Furthermore, Micro-Raman spectroscopy was used to determine chemical changes in the model NaCl/malonic acid mixture and investigate the extent of hydration of particles. Figure 3.17 shows representative Raman spectra taken on freshly prepared particles and Table 3.7 reports positions and assignments of the bands observed in the Raman spectra. The spectral profiles are similar, with differences mostly in broadening of peaks that can be attributed to solvation, where sharper transitions correspond to more dehydrated^{85,86} particles and spectra were assigned as dry (dehydrated), solvated, or partially solvated based on the extent of peak broadening. Particles stored in ambient conditions showed a large range hydration, having spectra that fell into all three spectral categories. Samples stored in a desiccator show only dehydrated or partially solvated particles. Interestingly, the frozen samples show no dehydrated or even only partially solvated spectra. This result confirms our conclusion that particles uptake water during thawing and suggests that composition (other than water uptake or release) is not significantly changing.

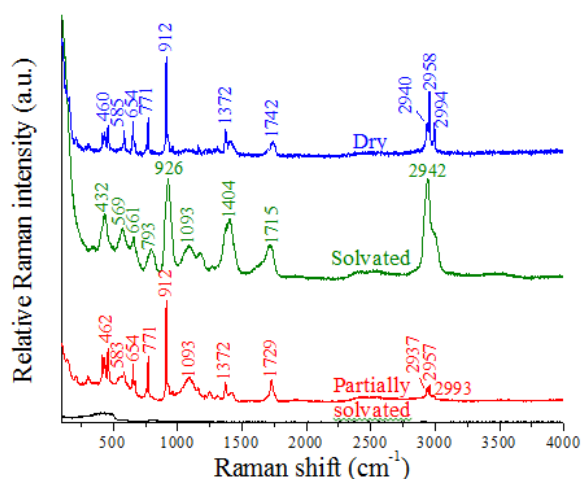


Figure 3.17: Raman spectra of reacted NaCl/malonic acid at different stages of solvation: dry (top), solvated (middle) and partially solvated (bottom). Peak assignments are shown in Table 3.7. All three types are found in freshly prepared sample as well as in the sample stored at ambient conditions after 2 and 4 weeks of storage. In the sample stored in desiccator only dry and partially solvated particles can be found. Frozen sample only shows solvated particles. Raman data was collected by Olga Laskina (Grassian group, University of Iowa).

Table 3.7: Positions and assignments of the bands observed in the Raman spectra of NaCl/malonic acid particles.

Dry	Partially solvated	Solvated	Literature	Assignment ^{87,88}
460	462	432	432	$\gamma(\text{CCO})$
585	583	569	578	Skeletal bending
654	654	661	642	$\delta(\text{COO})$
771	771	793	766	C-C
912	912	926	923	$\nu_a(\text{C-C-C})$
1372	1372	1404	1403	$\delta(\text{CH}_2)$
1742	1729	1715	1650	$\nu(\text{C=O})$
2940	2937	2942	2927	$\nu_s(\text{CH}_3)$
2958	2957		2954	$\nu_s(\text{CH})$
2994	2993		3005	$\nu_a(\text{CH})$

All data suggests that freezing samples induces significant particle changes but it is not clear if the changes occur during freezing or thawing. An additional study was performed in order to investigate whether these changes are caused by the temperature

change, thawing, or freezing. Figure 3.18 depicts the four experiments performed, where scenario A is the experiment that has been discussed previously – frozen and thawed with no humidity control, B was allowed to freeze without humidity control, then thaw in a desiccator, C was frozen in a desiccator and thawed at ambient room conditions, and D was frozen and thawed in a desiccator. Each sample was analyzed with AFM and for each scenario the scatterplot of diameters is reported, along with a representative image and compared to the size distribution for particles analyzed immediately after deposition (ambient). Interestingly, freezing or thawing without humidity control both induce the size changes, while controlling the humidity during both decreases the severity of particle change and coalescence. The size distribution for particles that undergo the freeze-thaw cycle in the desiccator (D) have a slightly higher size distribution but is still comparable to the original size distribution. Thus, it is apparent that in order to preserve particle morphology during freezing, humidity control is important because it significantly reduces the extent of phase changes.

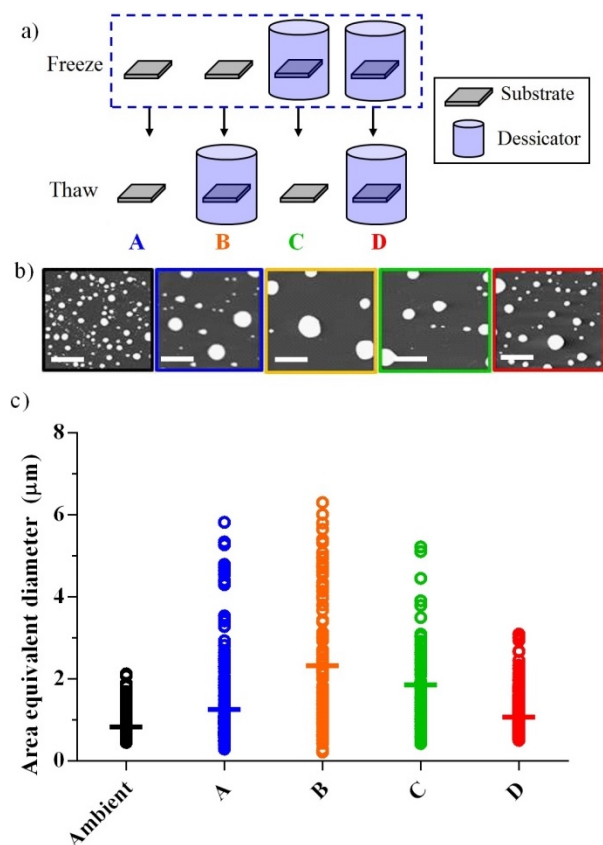


Figure 3.18: A) Schematic of freezing experiments performed. B) Representative AFM images from each experiment. Scale bar is 5 μm . C) Scatterplot of area equivalent diameter for each freezing scenario compared to newly prepared particles (ambient). Solid horizontal lines correspond to the mean diameter values.

3.5 Conclusions

Here we investigated the substrate, microscopy method and storage conditions influences the size and morphology of SSA particles. Typical substrates that are used for particle deposition for microscopy (silicon wafer, quartz and silicon nitride membranes) do not show significant deviation in size or morphology. Caution should be taken when comparing results for SSA obtained by different microscopy methods, as clear differences were observed between OM, AFM and SEM techniques. We conclude that the ambient-based approaches appear to be the most reliable way to determine representative size of SSA particles because the particles are not altered by vacuum

conditions. For particles in the submicron size range, OM does not have enough spatial resolution and AFM should be utilized instead. For SEM, the particle size decreases when the vacuum desorbs water or volatile species. However, this can be avoided by encapsulating particles in ambient conditions.

Storage of SSA samples under ambient laboratory conditions (~20% RH, 22 °C) does not appear to show any sample aging effects (over 4-7 week period) in either size or shape and thus, is recommended for single particle microscopy studies. Storing samples in the freezer results in clear changes in size and morphology, where particles become noticeably larger and sometimes agglomerate as a result of water uptake during freeze-thaw cycle. This result is supported by micro-Raman spectroscopy which shows significant degree of solvation in particles. However, if samples must be frozen, it is recommended to use humidity control to reduce particle coalescence. It should be noted that the SSA particles are very sensitive to these changes due to hygroscopicity and therefore, the conclusions made in this study may not be applicable to other types of the aerosols.

4. SIZE MATTERS IN THE WATER UPTAKE AND HYGROSCOPIC GROWTH OF ATMOSPHERICALLY RELEVANT MULTICOMPONENT AEROSOL PARTICLES*

4.1 Abstract

Understanding the interactions of water with atmospheric aerosols is crucial for determining the size, physical state, reactivity, and climate impacts of this important component of the Earth's atmosphere. Here we show that water uptake and hygroscopic growth of multi-component, atmospherically-relevant particles can be size dependent when comparing 100 nm versus ca. 6 μm sized particles. It was determined that particles composed of ammonium sulfate with succinic acid and of mixture of chlorides typical of the marine environment show size dependent hygroscopic behavior. Microscopic analysis of the distribution of components within the aerosol shows that the size dependence is due to differences in the mixing state, i.e. whether particles are homogeneously mixed or phase separated, for different sized particles. Morphology dependent hygroscopicity has consequences for heterogeneous atmospheric chemistry as well as aerosol interactions with electromagnetic radiation and clouds.

4.2 Introduction

The hygroscopic behavior and cloud condensation nuclei activity of multi-component atmospheric aerosol particles depends on their mixing state.^{42,79} It has been previously shown that when organic compounds are mixed with inorganic salts, both the

* Adapted from Laskina, O.; Morris, H. S.; Grandquist, J. R.; Qin, Z.; Stone, E. A.; Tivanski, A. V.; Grassian, V. H. Copyright (2015) *J. Phys. Chem. A* *119*, 4489–4497.

deliquescence and efflorescence relative humidity, DRH and ERH, respectively, of the salt decreases when these components are homogeneously mixed.⁸⁹ As a result of the lowering of both the DRH and ERH, these particles remain in the liquid state over the relative humidity (RH) range typically experienced by particles in the atmosphere. In contrast, when the organic component phase separates from the inorganic salt in heterogeneous particles, there is little or no change in DRH and ERH values from those of the salt component.^{25,69,89-92} Although these differences in the water uptake and hygroscopic growth between homogeneously mixed and phase separated aerosol particles are well understood, what is not clear is whether hygroscopic properties and mixing states can depend on the particle size.

In general, the morphology of phase-separated particles depends on composition, including organic material, inorganic salt and organic to inorganic ratio.^{25,69,89-92} Previously, it was inferred that phase separation behavior for ammonium sulfate (AS) when mixed with secondary organic material is size-independent.⁹² However, Veghte et al. recently reported size-dependent liquid-liquid phase separation for organic-inorganic mixtures of ammonium sulfate mixed with pimelic acid.⁹³ Liquid-liquid phase separation in larger particles leads to phase separation in these particles upon drying whereas smaller particles are homogeneous at all RH. Thus, size of particles can result in different mixing states and therefore may yield to different hygroscopic properties. Since the mixing states (i.e. components homogeneously mixed or phase separated), of multi-component aerosol particles can be size dependent, we hypothesized that it would also lead to size-dependent water uptake properties in multi-component aerosol particles. The determination of size dependent hygroscopic growth that originates from the difference in

mixing states due to size effects is essential towards better understanding of aerosol reactivity and climate forcing.

Typically, water uptake and hygroscopic growth of submicron aerosol particles are studied by hygroscopic tandem differential mobility analyzers (HTDMA) whereas supermicron particles are often studied by microscopy methods such as micro-Raman or infrared spectroscopy where particles are typically substrate-deposited for these optical measurements along with substrate free methods such as particle levitation techniques.^{69,73,94–99}

In this study, we investigate the size dependent mixing states, water uptake and hygroscopic properties of multi-component aerosol particles using HTDMA and micro-Raman spectroscopy. Mixtures of sodium, magnesium, calcium and potassium chlorides were studied as the most abundant inorganic components of sea spray aerosol.¹⁰⁰ Additionally, a mixture of AS with succinic acid (SA), representative of mixed inorganic-organic aerosols, was studied.¹⁰¹ In order to understand the mixing states of these mixtures, we utilized several complimentary microscopy techniques including atomic force microscopy (AFM), scanning electron microscopy coupled with energy dispersive X-ray spectroscopy (SEM/EDX) and chemical functional group mapping using micro-Raman spectroscopy. As discussed and shown here for the first time, the size dependence of water uptake and hygroscopic growth is a result of the aerosol particle mixing state.

4.3 Experimental

4.3.1 Sample preparation

Aerosol particles are formed by atomizing (TSI Inc., Model 3076) solutions in Optima water (Fisher Scientific). Ammonium sulfate (NH_4SO_4), sodium chloride (NaCl) and potassium chloride (KCl) are purchased from Fisher Scientific (all $\geq 99.0\%$); succinic acid ($\text{HOOC}-(\text{CH}_2)_2-\text{COOH}$, SA), magnesium chloride hexahydrate ($\text{MgCl}_2 \cdot 6\text{H}_2\text{O}$) and calcium chloride dihydrate ($\text{CaCl}_2 \cdot 2\text{H}_2\text{O}$) are purchased from Sigma-Aldrich (all $\geq 99.0\%$); malonic ($\text{HOOC}-\text{CH}_2-\text{COOH}$, MA) and adipic acids ($\text{HOOC}-(\text{CH}_2)_4-\text{COOH}$, AA) are purchased from Alfa Aesar (both 99.0%) and are used without further purification.

Pure AS and NaCl particles are prepared by atomizing solutions containing 0.5 wt. % of either salt. Mixed AS/SA and AS/AA particles are prepared from solution containing 0.5 wt. % AS and 0.5 wt. % organic acid. That corresponds to the expected organic to inorganic mass ratio of atmospheric aerosol particles that ranges from 0.2 to 3.5.^{80,81,82} Mixed NaCl/MA particles are prepared from solution containing 0.5 wt. % NaCl and 2:1 molar ratio between NaCl and MA. Mixture of chlorides are prepared from solution of NaCl, $\text{MgCl}_2 \cdot 6\text{H}_2\text{O}$, $\text{CaCl}_2 \cdot 2\text{H}_2\text{O}$ and KCl with a ratio of Na^+ , Mg^{2+} , Ca^{2+} , K^+ = 1:0.11:0.02:0.02 wt.%, respectively, to mimic the composition of sea water and therefore are referred to as marine chloride mixture. Upon exiting the atomizer, aerosols with a flow rate of 1.5 lpm are passed through diffusion dryer (TSI Inc., Model 3062) to reduce RH to $< 5\%$.

4.3.2 Hygroscopic Tandem Differential Mobility Analyzer (HTDMA)

Hygroscopicity as a function of increasing and decreasing RH of 100 nm particles at 298 K is measured using a HTDMA system. For these measurements, dehydrated aerosol particles are size-selected at 100 nm with a differential mobility analyzer (DMA; TSI, Inc. Model 3080). The monodispersed aerosols are directed to hydration chamber where it was equilibrated at different RH values. The RH is adjusted by varying the ratio of wet and dry air supplied by a commercial dry air generator (Parker Balston, Model 75-62). A portion of the dry air is sent through a bubbler to humidify. The dried aerosol and humidified air are combined in the hydration chamber. Then the aerosol particles are directed to a scanning mobility particle sizer (SMPS; TSI, Inc. Model 3936) that consists of a DMA (TSI, Inc., Model 3080) and a condensation particle counter (CPC; TSI, Inc. Model 3025A) where size distribution of the humidified aerosol are measured. Hygroscopicity curves are obtained by measuring the change in particle diameter with increasing and decreasing RH. RH is changed stepwise and size distribution is measured as soon as RH stabilizes after being changed (5-20 min). RH steps are 5-7% in the RH range where no phase transitions is expected and 0.1-0.5% in the RH range close to expected DRH and ERH. Size distribution data are fit to Gaussian curve to obtain particle diameters. At each RH value, the total hygroscopic growth are expressed as the growth factor, $g(\text{RH})$ calculated according to Equation 1:

$$g(\text{RH}) = \frac{D_p(\text{RH})}{D_o} \quad (\text{Eq. 4.1})$$

where $D_p(\text{RH})$ is a particle diameter at a particular RH value and D_o is the diameter of the dry particle. Growth factor is then plotted as a function of RH.

4.3.3 Micro-Raman spectroscopy

For Micro-Raman measurements of the hygroscopic growth of single supermicron-sized aerosol particles (3-12 μm), Raman spectra is collected for 3 to 5 min by placing a quartz disc (Ted Pella Inc., part no. 16001-1) hydrophobically coated using Rain-X¹⁰², a commercially available product, that contains polysiloxanes. The quartz disc is placed on the surface of the impactor installed in front of DMA that is primarily designed to remove large ($>1 \mu\text{m}$) particles. Therefore, this placement is suitable for the collection of supermicron-sized particles. This quartz disc is then placed inside a flow cell (Linkam microscope stage LTS120) that is situated on the motorized stage under the Raman microscope. The flow cell has an inlet and outlet valve to enable the system to be operated under a continuous stream of humidified air with the RH controlled by adjusting the ratio of wet and dry air prior to entering the stage. This design is similar to the RH control system used for HTDMA experiments described above. The flow cell with the sample inside is then placed on motorized microscope stage. Raman spectroscopy is performed using a LabRam HR Evolution Raman spectrometer (Horiba). The spectrometer is equipped with an Olympus BX41 optical microscope. In the experiments described here, the long working distance (7.6 mm) objective lens with 100X magnification is used. Raman scattering is performed using a laser operating at 532 nm. Raman spectra is recorded in the spectral range from 100 to 4000 cm^{-1} , three exposures of 15 s each are averaged to obtain the resulting spectrum.

Raman growth factor is defined as the ratio of integrated area of OH stretching mode of water ($3050\text{-}3700 \text{ cm}^{-1}$)¹⁰³ at each RH (A_{RH}) normalized to that of a dry particle (A_{RH0}). For particles containing AS, the $3350\text{-}3700 \text{ cm}^{-1}$ wavenumber range is used to

avoid any overlap with N-H stretching region for the ammonium ion in AS.¹⁰⁴ Hygroscopic growth curves are obtained by plotting Raman growth factor as a function of RH. Similar to HTDMA experiments, the RH is changed stepwise. At each RH, a Raman spectrum is collected after the RH stabilizes (ca several minutes). Raman maps of individual particles are collected by raster-scanning the laser focal spot and gathering point-by-point spectral data with a step size of 400 nm. AS map is obtained by mapping the intensity of 960-990 cm^{-1} spectral region. For SA and AA maps, the intensity of 920-950 cm^{-1} and 900-930 cm^{-1} spectral regions is used, respectively.

4.3.4 Atomic Force Microscopy (AFM)

For AFM imaging, aerosol particles are collected on silicon wafers (Ted Pella Inc., part no. 16008). Supermicron particles are collected for 3-5 min by placing a silicon wafer in place of impaction surface of the DMA impactor as described above. Small particles are collected after being selected by DMA at 100 nm for 30 min by directing monodisperse particle flow on the substrate. AFM images are obtained using molecular force probe 3D AFM (Asylum Research, Santa Barbara, CA). Phase images are collected using intermittent contact mode (AC mode) and silicon probes (MikroMasch, Model CSC37) with a nominal spring constant of 0.35 N/m and a typical tip radius of curvature of 10 nm. A phase shift in the image is a result of a lag between the excitation oscillation of the cantilever and the output oscillation associated with the tip interacting with the sample surface. Viscosity, chemical composition, adhesion force, and elasticity of the sample are among factors that can cause changes in the phase.^{105,106} Phase imaging therefore allows compositional contrast on heterogeneous surfaces and can reveal spatially resolved information of the sample surface that reflects differences in the

physical state and/or chemical composition associated with a phase separated particle. All images are collected at room temperature and at controlled RH. Samples are placed in a humidity cell described elsewhere and the RH is adjusted to below 10% and allowed to equilibrate for 5-10 min. Low RH improves phase imaging and prevents phase differences around particles due to surrounding water layer.

4.3.5 Ambient Pressure SEM coupled with EDX Spectroscopy

For ambient pressure SEM/EDX mapping, aerosol particles are collected upon exiting the dryers for 3-5 min on WETSEM Capsules (Quantomix, part no. QX-102) to avoid having particles dry out completely under the vacuum environment of the SEM chamber. SEM images and maps are collected using a Hitachi S-4800 SEM. The SEM is coupled with an EDX detector equipped with Iridium Ultra microanalysis software (IXRF Systems Inc.) for elemental analysis. The electron microscope is operated at 20 kV accelerating voltage, 10 μ A current, images are collected at 8 mm working distance.

4.4 Results

4.4.1 Ammonium sulfate and sodium chloride

Raman spectra of AS and NaCl collected at low (3-4%) RH and high (85-89%) RH are shown in Figure 4.1 with quartz spectra (substrate) as a reference. As expected, dry NaCl has no vibrational transitions in 100-4000 cm^{-1} range. Dry AS Raman spectra show SO_4^{2-} vibrational modes at 450, 625, 974 and 1105 cm^{-1} as well as NH_4^+ vibrational modes at 1417, 1665 and 3143 cm^{-1} .²⁴ At RH above deliquescence point a broad band at 3400 cm^{-1} appears for both samples and originates from O-H stretching modes of water.

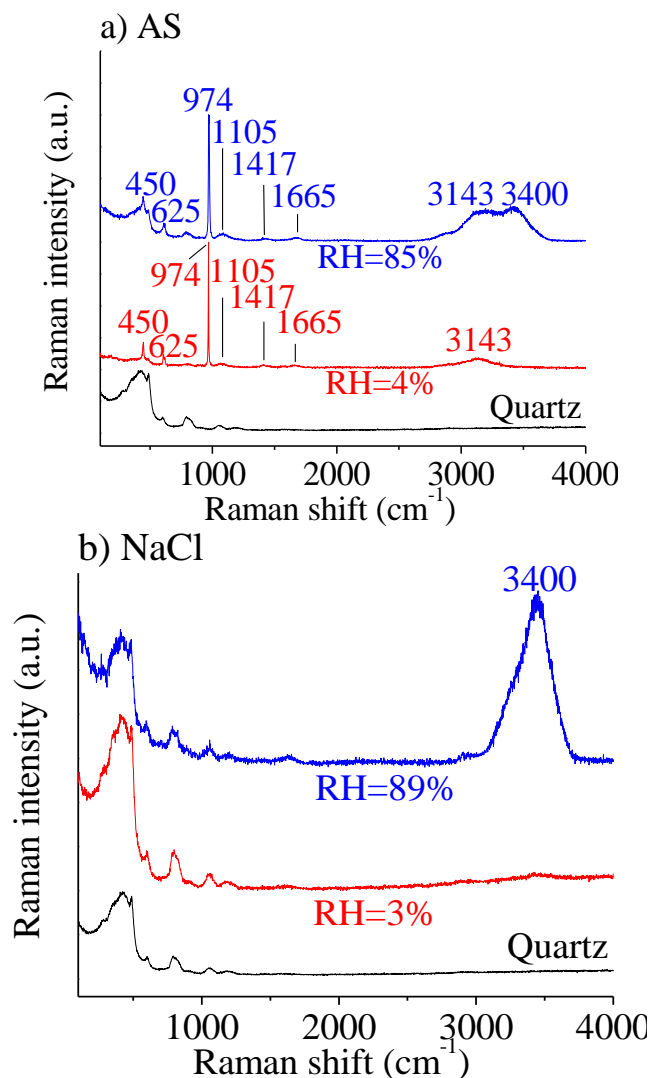


Figure 4.1: a) AS and b) NaCl Raman spectra of dry (red) and deliquesced (blue) particles are shown as representative spectra. Raman spectra of the substrate (quartz) is also shown for reference (black). Raman data was collected by Olga Laskina (Grassian group, University of Iowa).

AS and NaCl hygroscopicity were measured using HTDMA for 100 nm particles and using micro-Raman spectroscopy for substrate deposited supermicron particles. Measured hygroscopicity curves are shown in Figure 4.2. DRH of AS was determined to be $80.4 \pm 0.6\%$ RH using HTDMA and $82.3 \pm 2.5\%$ RH using micro-Raman spectroscopy. The uncertainty in DRH and ERH values for HTDMA are standard deviations of multiple (three to five) measurements. Micro-Raman spectroscopy has been

performed on several individual particles (three to six) and therefore uncertainty in DRH and ERH values are standard deviations in these values of several individual particles. These values agree well between each other and with literature values which range from 77 to 83% RH.^{94,107-109} ERH was measured at $37.7 \pm 4.1\%$ RH for HTDMA and $43.5 \pm 2.1\%$ RH using micro-Raman spectroscopy. These values also agree with range of values in the literature between 33 to 48% RH.¹⁰⁸⁻¹¹¹ In general, there are larger difference in ERH values because ERH is often a kinetically controlled process whereas the DRH is controlled by thermodynamics.¹¹² Therefore, it has been observed that a variety of effects and different conditions (drying rate, the presence of the substrate, particle size) may impact ERH but these do not influence DRH.

DRH values for NaCl were $74.0 \pm 0.2\%$ RH and $77.5 \pm 2.1\%$ RH as probed by HTDMA and micro-Raman spectroscopy, respectively. These values agree well with reported literature values 74 to 76% RH within experimental error.^{94,107,109,113,114} ERH values were $43.0 \pm 1.0\%$ RH and $52.8 \pm 1.1\%$ RH as probed by HTDMA and micro-Raman spectroscopy respectively. These also are close to reported literature values of 44 to 50% RH.^{114,115} DRH and ERH values for these experiments of simple single component systems (AS and NaCl) at two different sizes (i.e. submicron and supermicron) are listed in Table 4.1.

Table 4.1: Measured DRH and ERH values for single component and multi-components particle compositions at two size ranges: 100 nm, submicron, as measured using HTDMA system, and 3-10 μm , supermicron, as measured using micro-Raman spectroscopy. Data was collected by Olga Laskina (Grassian group, University of Iowa).

Sample Mixture	Submicron	Supermicron	Submicron	Supermicron
	DRH (% RH)		ERH (% RH)	
Pure AS	80.4 \pm 0.6	82.3 \pm 2.5	37.7 \pm 4.1	43.5 \pm 2.1
Pure NaCl	74.0 \pm 0.2	77.5 \pm 2.1	43.0 \pm 1.0	52.8 \pm 1.1
NaCl/MA (2/1 molar)	67.0 \pm 4.4	71.8 \pm 5.3	36.2 \pm 0.4	49.1 \pm 1.6
AS/AA (1:1 wt.%)	79.3 \pm 0.5	82.2 \pm 0.6	31.8 \pm 1.7	44.6 \pm 1.3
AS/SA (1:1 wt.%)	73.2 \pm 0.6	82.7 \pm 0.3	29.2 \pm 6.1	45.5 \pm 1.1
Marine chloride mixture	66.1 \pm 0.1	75.3 \pm 1.1	40.0 \pm 1.2	49.0 \pm 0.7

The growth of aqueous solution droplets in humid air can be described by Kohler theory.^{94,116,117} Diameter of the aqueous solution droplet is related to RH according to Equation 2:

$$\% RH = 100 \times a_w \times e^{\frac{4 \times M_w \times \sigma_{sol}}{R \times T \times \rho_w \times D_p}} \quad (\text{Eq. 4.2})$$

where a_w is the water activity, M_w is the molar mass of water, σ_{sol} is the surface tension of solution, ρ_w is the density of water, R is the ideal gas constant, and T is the temperature.

A theoretical growth factor can be calculated using Equation 3:

$$g(RH) = \left(\frac{\rho_s}{\frac{c_{sol}}{100} \times \rho_{sol}} \right)^{1/3} \quad (\text{Eq. 4.3})$$

where ρ_s is the solute density, ρ_{sol} is the solution density, and c_{sol} is the solution concentration. Theoretical growth curve can therefore be calculated by combining Equations 1-3 as described in Gibson et al.¹¹⁸

Hygroscopic growth curves for NaCl and AS were calculated using Kohler theory and are shown in Figure 4.2 (black lines). Overall, as expected, the determined hygroscopicity shows that hygroscopicity curves of AS and NaCl measured by HTDMA and Raman overlap with each other and with corresponding theoretical Kohler curves. DRH and ERH values agree well with each other as well as with literature values. HTDMA and micro-Raman spectroscopy show similar and reliable results for RH values of phase transitions of sub- and supermicron aerosol particles, respectively. Based on these results it can be concluded that both HTDMA and micro-Raman methods can be used to study hygroscopicity. It should be noted here that it is preferable to use hydrophobic substrate in order to measure growth of particles and phase transitions of particles as a function of RH as it has been shown before that hydrophobicity/hydrophilicity of the substrate can influence observed hygroscopicity of inorganic salts and spatial distribution of organic and inorganic phases in mixed substrate deposited particles.^{72,73}

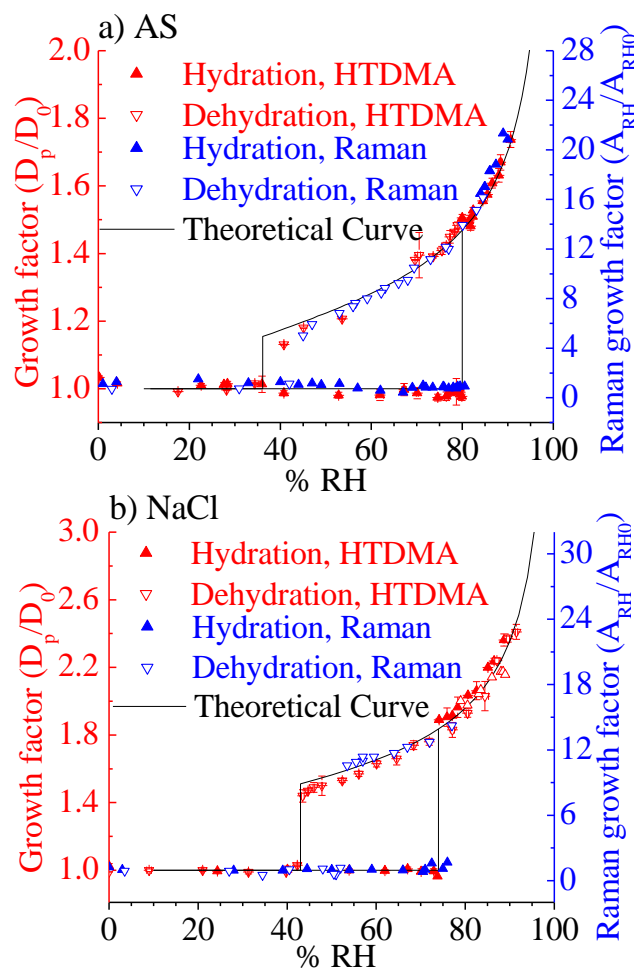
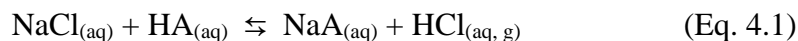


Figure 4.2: a) AS and b) NaCl hygroscopicity measured by HTDMA for 100 nm particles (red triangles) and micro-Raman results for supermicron particles (blue triangles). Theoretical Köhler curves are shown in black. Data was collected by Olga Laskina (Grassian group, University of Iowa).

4.4.2 Sodium chloride mixed with malonic acid, 2:1 molar ratio

It has been shown previously that in aqueous micrometer size droplets NaCl can react with organic acids through acid displacement reactions releasing gas-phase HCl and forming organic salts in the particle phase according to Reaction 4.1 below.¹¹⁹



where HA are atmospherically relevant organic acids.

This reaction may therefore lead to depletion in the chloride levels in the particle due to the formation of hydrogen chloride gas. However, chloride is not completely depleted for the NaCl/MA mixture used here and it has been reported using the same conditions that approximately half of the chloride in the particle is removed through Reaction 1. This is consistent with our results showing 43% reduction of Cl in NaCl/MA acid mixture comparing with NaCl using elemental analysis. Thus, the resulting particles are expected to be a mixture of the excess of NaCl and sodium hydrogen malonate rather than pure sodium hydrogen malonate. AFM phase images of sub- and supermicron size particles are shown in Figure 4.3a. Particles in the submicron size range are shown on the right, supermicron particles are shown on the left. As can be seen from these images, both, submicron and supermicron particles are homogeneous, showing a single value for phase as indicated by the uniform color in the image. SEM/EDX map in Figure 4.3b shows distribution of Cl, Na, C and O in a supermicron particle. As can be seen from the SEM/EDX data, there is a uniform distribution of all these elements which means that NaCl and sodium hydrogen malonate are distributed homogeneously throughout the particle.

Figure 4.3c shows hygroscopicity curves of mixed NaCl/MA particles measured by HTDMA (red) and micro-Raman spectroscopy (blue). Determined DRH and ERH values are summarized in Table 4.1. These particles start to absorb water at approximately 40% and become fully deliquesced at $67.0 \pm 4.4\%$ RH (submicron) and $71.8 \pm 5.3\%$ RH (supermicron) which is lower than DRH of NaCl (74-76% RH). It was shown before that NaCl/MA mixed particles starts to uptake water at RH values below DRH and fully deliquesce between 50 and 75% RH, while hysteresis between

hydration/dehydration cycles diminishes as the ratio between organic and inorganic components increases.^{95,120,121} The decrease in DRH values and homogeneous composition of NaCl/MA particles at submicron and supermicron sizes are also consistent with previous observations that homogeneously mixed inorganic/organic particles decrease DRH of inorganic component.

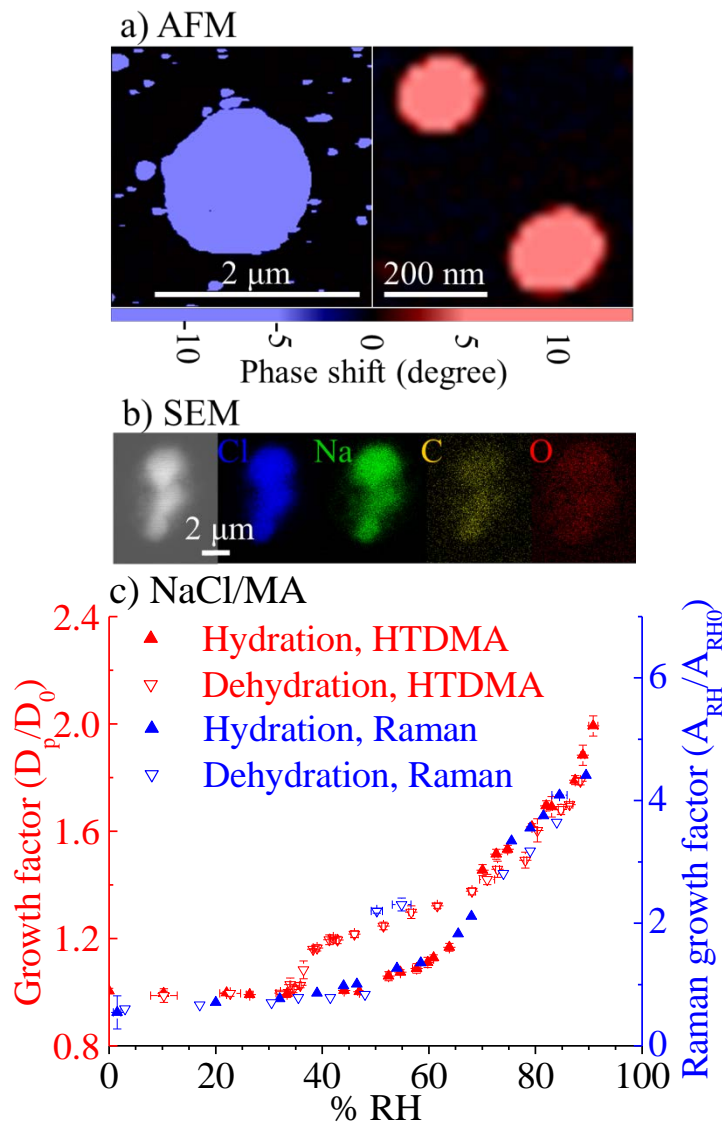


Figure 4.3: a) AFM phase images at 10% RH of submicron and supermicron NaCl/MA (2:1 molar ratio) particles and b) SEM image and Cl, Na, C, O elemental maps of a supermicron particle captured at 20% RH in a WETSEM capsule; c) hygroscopicity measured by HTDMA for 100 nm particles (red triangles) and by micro-Raman spectroscopy for supermicron particles (blue triangles). Hygroscopicity data was collected by Olga Laskina (Grassian group, University of Iowa) and SEM data was collected by Josh Grandquist (Grassian group, University of Iowa).

4.4.3 Ammonium sulfate mixed with adipic acid, 1:1 weight ratio

AFM phase images of sub- and supermicron mixed AS/AA particles are shown in Figure 4.4a, Raman chemical functional map of a supermicron particle is shown in Figure

4.4b. AS map was obtained by mapping the intensity of $960\text{-}990\text{ cm}^{-1}$ spectral region. For AA map the intensity of $900\text{-}930\text{ cm}^{-1}$ spectral region was used. Raman spectra of AS, AA and AS/AA mixture are shown in Figure 4.4. Raman chemical maps were used here instead of SEM/EDX as both, AS and SA are Raman active. In case of NaCl/MA mixture NaCl is not Raman active, therefore elemental maps were used to show spatial distribution of NaCl/MA mixture components. As can be seen in Figure 4.5, both AFM phase imaging data and Raman maps clearly show these particles are heterogeneous and undergo phase separation at both size ranges. Furthermore, Raman maps illustrate that the particle core consist primarily of AS, surrounded by AA. These current results are consistent with earlier reports that show AS/AA particles phase segregate for all sized particles.¹²²

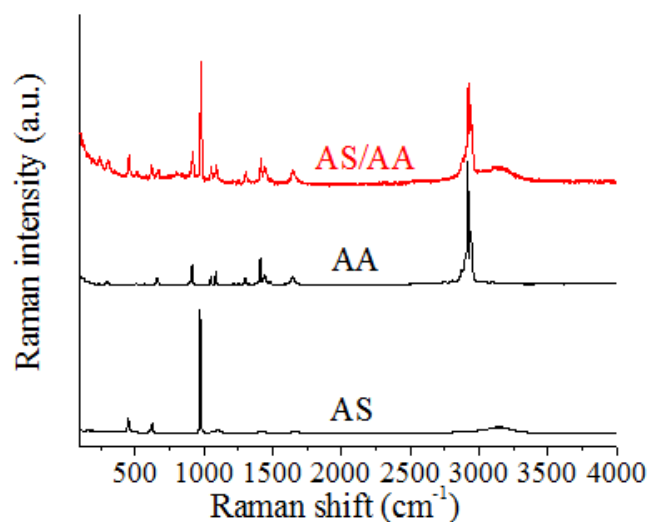


Figure 4.4: Raman spectra of ammonium sulfate and adipic acid particles (black) and ammonium sulfate/adipic acid mixed particles (red). Blue box highlights the region used to construct an adipic acid map ($900\text{-}930\text{ cm}^{-1}$), red box highlights the region used to construct an ammonium sulfate map ($960\text{-}990\text{ cm}^{-1}$). Data was collected by Olga Laskina (Grassian group, University of Iowa).

Figure 4.5c shows hygroscopicity curves of mixed AS/AA particles probed by HTDMA (red) and micro-Raman spectroscopy (blue). DRH and ERH values determined from these experiments are summarized in Table 4.1. The hygroscopic behavior of submicron and supermicron particles are similar with DRH values of $79.3 \pm 0.5\%$ RH (submicron); $82.2 \pm 0.6\%$ RH (supermicron), which is close to DRH values of AS. These results are consistent with our observation that AA and AS form heterogeneous particles, and as it is noted previously, DRH and ERH points of heterogeneously mixed organic/inorganic systems are typically similar to the DRH and ERH of the inorganic salt component.

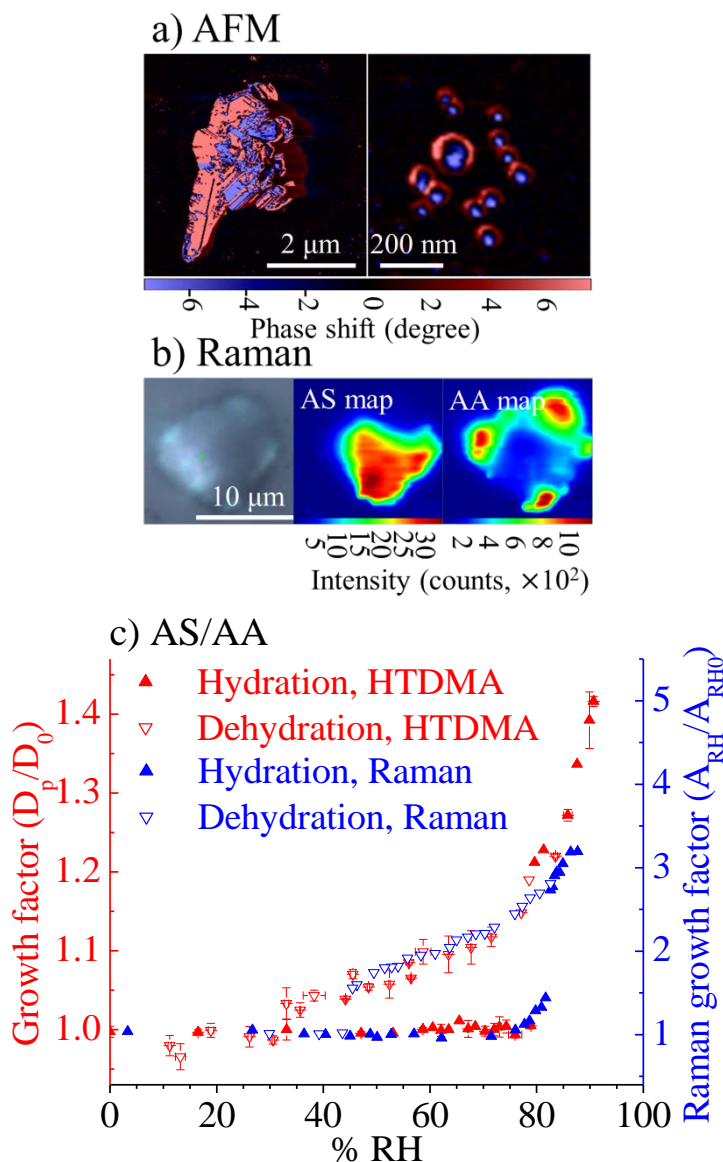


Figure 4.5: a) AFM phase images at 10% RH of submicron and supermicron AS/AA particles and b) Raman image, AS and AA maps of a supermicron particle at 20% RH; c) hygroscopicity measured by HTDMA for 100 nm particles (red triangles) and micro-Raman spectroscopy for supermicron particles (blue triangles). Raman and hygroscopicity data was collected by Olga Laskina (Grassian group, University of Iowa).

4.4.4 Ammonium sulfate mixed with succinic acid, 1:1 weight ratio

AFM phase images of particles aerosolized from AS/SA mixture are shown in Figure 4.6a. Raman image and map of supermicron particle are shown in Figure 4.6b. AS map was obtained by mapping the intensity of 960-990 cm^{-1} spectral region. For SA map

the intensity of $920\text{-}950\text{ cm}^{-1}$ spectral region was used. Raman spectra of AS, SA and AS/SA mixture are shown in Figure 4.7. Raman maps of AS and SA do not overlap which indicates that the components in these particles have clearly phase separated. It is consistent with earlier published results of small AS/SA particles having a homogeneous morphology, whereas larger particles phase separate into a partially engulfed morphology due to crystallization of the organic component before crystallization of AS.

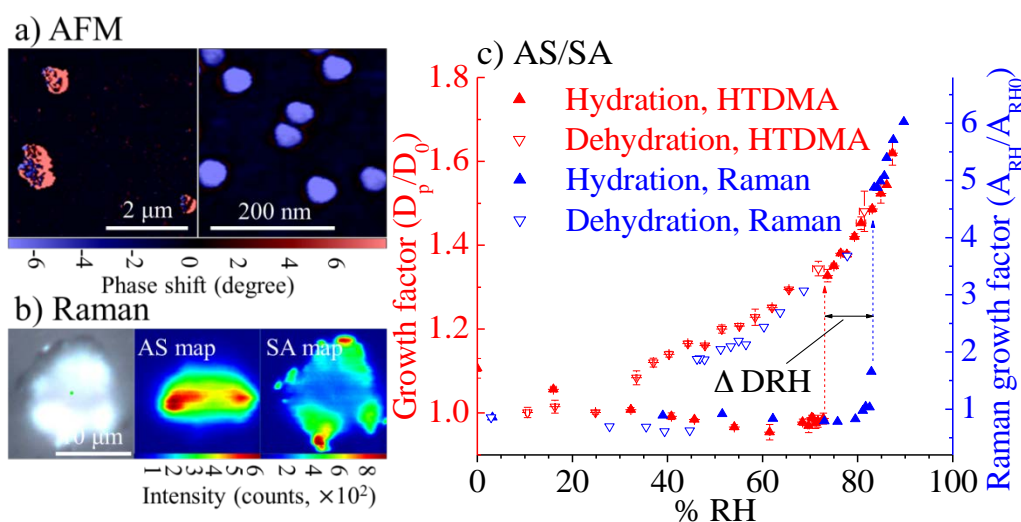


Figure 4.6: a) AFM phase images at 10% RH of submicron and supermicron AS/SA particles and b) Raman image, AS and SA maps of a supermicron particle at 20% RH; c) hygroscopicity measured by HTDMA for 100 nm particles (red triangles) and micro-Raman spectroscopy for supermicron particles (blue triangles). Dashed arrows indicate deliquescence of submicron (red) and supermicron (blue) particles. $\Delta\text{DRH} = 9.5\%$ is the difference between DRH values of submicron and 100 nm particles. Raman and hygroscopicity data was collected by Olga Laskina (Grassian group, University of Iowa).

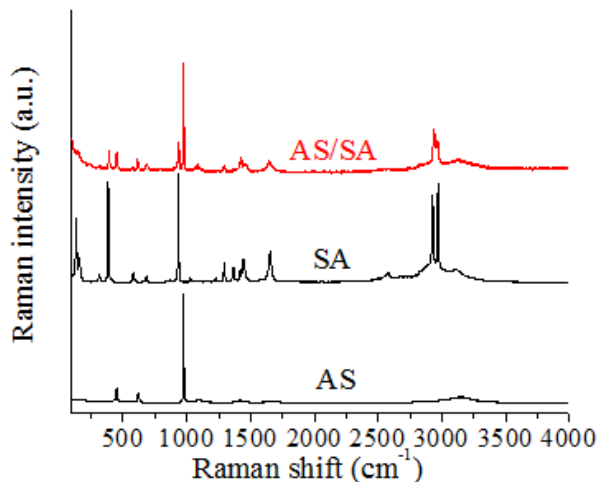


Figure 4.7: Raman spectra of ammonium sulfate and succinic acid particles (black) and ammonium sulfate/succinic acid mixed particles (red). Blue box highlights the region used to construct a succinic acid map ($920\text{-}950\text{ cm}^{-1}$), red box highlights the region used to construct an ammonium sulfate map ($960\text{-}990\text{ cm}^{-1}$). Data was collected by Olga Laskina (Grassian group, University of Iowa).

Hygroscopicity was measured by HTDMA for 100 nm aerosol particles and by Raman for substrate deposited supermicron particles. The results are shown in Figure 4.6c and tabulated in Table 4.1. As can be seen supermicron particles (blue triangles) deliquesce at $82.7 \pm 0.3\%$ RH and effloresce at $45.5 \pm 1.1\%$ RH which is close to deliquescence and efflorescence points of AS ($82.3 \pm 2.5\%$ RH and $43.5 \pm 2.1\%$ RH respectively, measured for supermicron substrate deposited AS particles by Raman). In contrast 100 nm particles deliquesce at $73.2 \pm 0.6\%$ RH and effloresce at $29.2 \pm 6.1\%$ RH which is lower of these values for AS (DRH of AS is $80.4 \pm 0.6\%$ RH and ERH is $37.7 \pm 4.1\%$ RH measured for 100 nm particles by HTDMA). The decrease in DRH values and homogeneous composition of 100 nm AS/SA particles and DRH close to AS DRH of supermicron AS/SA particles are consistent with previous observations that homogeneously mixed inorganic/organic particles decrease DRH of inorganic component

and there is little or no change in DRH and ERH values from those of the salt component in heterogeneous particles.

4.4.5 Marine chloride mixture

AFM phase images of particles aerosolized from Na, Mg, K and Ca chlorides are shown in Figure 4.8a. Particles in the submicron size range are shown on the right whereas supermicron particles are shown on the left. As can be seen from these images, submicron particles are homogeneous while supermicron is not as indicated by the phase image showing very distinct values of the phase shifts. SEM image and SEM/EDX maps of supermicron particle captured in the WETSEM capsule at ambient conditions (20% RH) are shown in Figure 4.8b. Na, Mg, Ca and K elemental maps clearly do not overlap and show clear evidence for phase separation.

Hygroscopicity was measured by HTDMA for 100 nm aerosol particles and by Raman for substrate deposited supermicron particles. The results are shown in Figure 4.8c and tabulated in Table 4.1. As can be seen supermicron particles (blue triangles) deliquesce at $75.3 \pm 1.1\%$ RH and effloresce at $49.0 \pm 0.7\%$ RH which is close to deliquescence and efflorescence points of NaCl ($77.5 \pm 2.1\%$ RH and $52.8 \pm 1.1\%$ RH respectively, measured for supermicron substrate deposited NaCl particles by Raman). In contrast, 100 nm particles deliquesce at $66.1 \pm 0.1\%$ RH and effloresce at $40.0 \pm 1.2\%$ RH which is lower of those value for NaCl (DRH of NaCl is $74.0 \pm 0.2\%$ RH and $43.0 \pm 1.0\%$ RH measured for 100 nm NaCl particles by HTDMA).

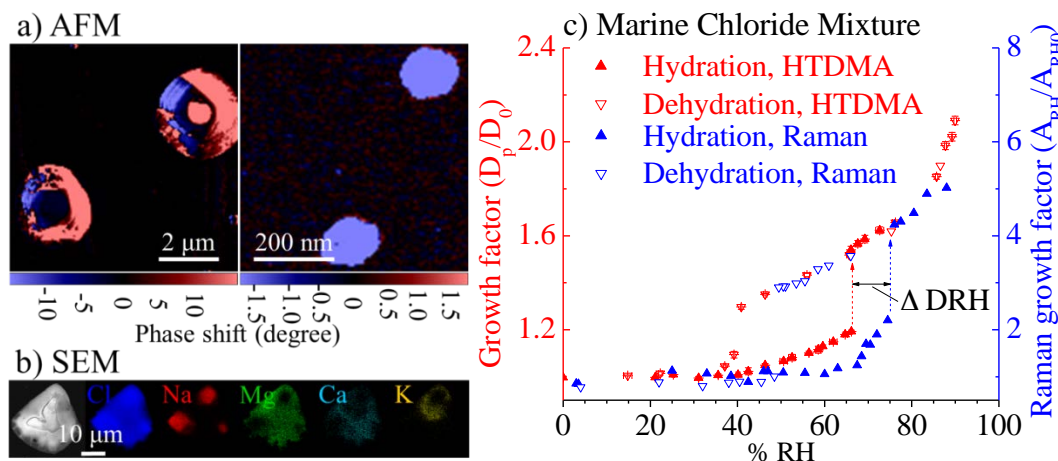


Figure 4.8: a) AFM phase images of marine chloride mixture at 10% RH of submicron (right) and supermicron (left) particles and b) SEM image and Cl, Na, Mg, Ca, K elemental maps of a supermicron particle captured at 20% RH in WETSEM capsule; c) hygroscopicity of mixed chloride particles measured by HTDMA for 100 nm particles (red triangles) and micro-Raman spectroscopy for supermicron particles (blue triangles). Dashed arrows indicate deliquescence of submicron (red) and supermicron (blue). Δ DRH = 9.2% is the difference between DRH values of submicron and 100 nm particles. Hygroscopicity data was collected by Olga Laskina (Grassian group, University of Iowa) SEM data was collected by Josh Grandquist (Grassian group, University of Iowa).

4.5 Discussion

Multi-component aerosols have different hygroscopic behaviors depending on whether they are uniformly mixed particles or if they phase separate. This has been well established in the literature.^{25,69,89,90,92} The main differences observed for these different mixing states are as follows. For homogeneous mixtures of organic matter with an inorganic component, the values of both the DRH and ERH are lower relative to the pure inorganic salt. As a result, these particles can remain in the liquid state for RH range typical in the atmosphere. Other organic molecules tend to phase separate from aqueous inorganic salt causing little to no change in DRH and ERH values.⁹⁰ For AS it was shown that the nature of secondary organic material (SOM) determines if DRH and ERH values are equal or lower than that of the pure ammonium sulfate. For example, products of dark

ozonolysis of α -pinene, do not influence DRH and ERH of ammonium sulfate in mixed particles while SOM produced by photo-oxidation of α -pinene were shown to decrease DRH and ERH of AS particles in mixtures.^{89,90} Interestingly, the morphology of phase-separated particles depends on composition, including organic material, inorganic salt and organic to inorganic ratio.⁹² The actual morphology of organic/inorganic mixed particle can be expected to vary with a dependence on the organic volume fraction, the particle size, and the relative surface tensions of the two phases against air as well against each other.¹²³ The phase-separated morphologies of the submicrometer aerosol particles studied by HTDMA could be different from those of supermicrometer supported particles studied in the microscopy experiments.⁵ In the supermicron mixed polyethylene glycol/AS particles the number of inorganic inclusions in the organic phase was found to depend on the size of the entire particles. Number of AS satellite inclusions in the outer phase decreases with decreasing the size of particles.¹²⁴ Highly polar organic substances with high O:C ratios may increase the solubility of AS in aqueous organic mixtures and thus decrease ERH and DRH of AS. Moreover, high viscosity in organic-rich particles may hinder the crystallization of AS.

SA deliquesces close to 100% RH and has very low solubility in water.¹²⁵ Therefore in AS/SA particles that are phase separated SA acts almost inert during deliquescence of AS. Therefore the deliquescence and efflorescence of an externally mixed AS/SA particle are controlled by AS and DRH and ERH values are close to that of AS. This result is consistent with observations of Choi et al. that were carried out for supermicron mixed AS/SA particles.¹²⁰

One of the factors that determine morphologies of mixed organic/inorganic particles is the surface tension. The shape of a droplet composed of two liquid phases can be calculated using the surface tensions of each of the components. Based on calculations by Song et al., it was shown that the most favorable configurations of supermicron mixed AS/organic particles are core-shell or partially engulfed morphologies with an organic-rich phase being on the outer surface of AS-rich phase. However they note that this prediction is only strictly valid for phases of infinite volume where the surface and interfacial area changes can be approximated as being the same. In cases of finite volumes when the spreading coefficient is close to zero, the morphology predictions may become less reliable.¹¹² Surface tension of aqueous AS solution is 88.8 mN/m at $a_w = 0.8$ (solution saturation of AS).¹²⁶ Surface tension of SA can be calculated from the Equation 4:¹²⁷

$$\sigma = 83.45 - 0.12T \quad (\text{Eq. 4.4})$$

Where T is the temperature in K. At T=293 K, the surface tension of SA is 48.29 mN/m which is significantly lower than that of aqueous AS solution. The morphology of a droplet containing two immiscible liquids will adjust to minimize the surface energy that can be achieved when the liquid with lower surface tension is at the surface,¹²⁴ so in SA/AS particles, the outer phase is expected to be SA-rich phase. This result is in fact supported by the Raman maps shown in Figure 4.5b. However, it can also be seen from the Raman maps that the SA does not completely coat the AS core. Particles composed of an aqueous salt and organic component with limited aqueous solubility preferentially form partially engulfed structures,¹²⁸ however it is also sometimes the result of drying of particles with core-shell morphologies that give this more heterogeneous “patchy” outer

coating.¹¹² Interestingly, a range of partially engulfed structures was observed by Buajarn et al. using decane/NaCl system that was also shown to depend on relative sizes of organic and aqueous droplet.¹²⁹ This result also supported by observation that in spatially separated organic/inorganic particles the outer phase is predominantly organic.⁶⁹

Phase separation does not occur in smaller particles most likely due to different drying rates as small particles have higher surface to volume ratio, higher evaporation rates and therefore dry more rapidly. This rapid drying can inhibit partitioning of the AS and SA into two separate phases. Furthermore, the addition of an organic component in small homogeneous particles leads to a decrease in the solution saturation with respect to AS for a constant RH. This leads to a decrease in the DRH to maintain unity saturation; and in a decrease in the ERH to maintain critical supersaturation.²⁵ It has been shown that for small homogeneous particles dissolution of soluble organic molecules into an aqueous ammonium sulfate phase can inhibit crystallization of the inorganic phase.¹³⁰

The reason for submicron AS/SA being homogeneous while AS/AA being phase separated can be attributed to a difference in their solubility. It has been shown that mixed particles that contain components with different solubility's for inhomogeneous structures.¹³¹ AS is more soluble than both, SA and AA. Additionally AA has lower solubility than SA and therefore AS/AA mixture represent the system with a largest difference in solubility between components that can be the reason for these mixed particles to phase separate at all sizes.

For mixtures of inorganic salts, theoretical predictions show that the DRH of one electrolyte is lowered by the addition of a second electrolyte.¹³² Ge et al. examined the crystallization of droplets of a two-electrolyte system consisting of NaCl/KCl of the

different proportions between NaCl and KCl and showed that their hygroscopic behavior as well as composition and homogeneity of the dried particle depends on relative proportions of NaCl and KCl. In solution, where KCl wt. % is lower than an eutonic composition, a dried particle is composed of a pure NaCl core surrounded by a coating of eutonic composition.¹³³ If this dried particle is subjected to an increase in RH, the particle will remain unchanged until mutual DRH (MDRH) is reached (that is lower than DRH of both NaCl and KCl). The coating, having eutonic composition at the particle surface, is then dissolved in the absorbed water. Further increasing the RH results in more water absorbed into the particle, and part of the pure NaCl solid core is dissolved to maintain the water equilibrium between the solution and the atmosphere. At a certain RH, which is close to but lower than the DRH of pure NaCl solid core, there is complete dissolution, and the particle becomes an aqueous droplet. In solution where KCl wt. % is higher than required to form an eutonic composition, a dried particle is composed of a pure KCl core surrounded by a coating of eutonic composition. When a particle of this composition is introduced to increasing RH, it starts to absorb water at MDRH but completely dissolves at RH between MDRH and KCl DRH. In solution of eutonic composition the particle crystallizes or deliquesces like pure salt at MDRH. The phase transformation either from aqueous to solid or from solid to aqueous occurs abruptly and the dried particles of this composition are morphologically and chemically uniform. Additionally, using surface sensitive techniques Ge et al. detected water adsorbed on the particle surface at RH lower than the MDRH.¹³³ In contrast, it was recently shown that ERH minimum of mixed supermicron NaCl and KCl aerosol particles is different from theoretically expected MERH at the eutonic mixture. It was suggested that efflorescence is driven by

crystallization of a more supersaturated salt and that the degree of KCl and NaCl supersaturation is affected by short-range ionic interactions and common-ion effect.¹³⁴

Hygroscopicity curves for marine chloride mixture derived from HTDMA and micro-Raman spectroscopy experiments indicate that these particles take up water prior to the deliquescence points due to the presence of Mg and Ca chlorides (DRH = 33 and 29% RH respectively).¹³⁵ 100 nm homogeneous particles start to pick up water at approximately 30% RH until finally deliquesce at 66.1% RH after which NaCl homogeneously distributed within a particle gradually dissolves in the solution as RH increases. In supermicron particles, chlorides are spatially separated with NaCl being the predominant phase as expected given the relative concentrations of the chloride mixture used here were for sea water. More hygroscopic components (Mg and Ca chlorides) start to absorb water and deliquesce at RH lower than deliquescence point of NaCl that causing the gradual slope of hygroscopicity curve before NaCl DRH. However, as the majority of the particle is NaCl, the complete deliquescence occur at the DRH of NaCl. It is not clear though why 100 nm particles deliquesce at lower RH and retain water longer than supermicron particles.

One additional consideration in this is that the observed difference in mixing state and hygroscopic properties can potentially be due to differences in particle composition due to an inherent fractionation of chemical components upon aerosol formation. It has been shown for atmospheric samples that larger particles are dominated by inorganics whereas smaller particles are dominated by organics.^{56,78} Remarkably, it has been shown that this effect can depend on aerosol production method. In particular, for sea spray aerosol it has been shown that wave breaking produces aerosol particles that are enriched

with organics in only smaller sizes, whereas aerosol particles produced by forcing air through submerged sintered glass filters are more enriched with organics at all sizes.¹³⁶ Therefore it can be proposed that transfer of the solution components used in this study to the aerosol phase can be depend on the size of the particle. Further studies of chemical fractionation are warranted and may play a role in the composition of aerosols. In this case bigger particles might be organic depleted and therefore retain hygroscopicity behavior similar to the inorganic component, whereas smaller particles might be organic enriched and show different hygroscopic behavior. However this hypothesis is not applicable to the observed difference in mixing state and hygroscopicity of inorganic particles formed from a marine chloride mixture. Thus, further investigations need to consider these particles types, i.e. mixtures of inorganic components, as well.

4.5 Conclusions

In this study, it has been shown that hygroscopicity measured by methods that use substrate deposited particles (micro-Raman spectroscopy) and substrate free approach (HTDMA) as well as different particles sizes (submicron for HTDMA and supermicron in micro-Raman spectroscopy) can be both be used to study particle hygroscopicity. Both methods show reliable results that agree well with literature data and theoretical predictions. Using these two methods, size dependent hygroscopicity of variety of atmospheric aerosol mixtures were measured. A number of multi-component systems were studied here including proxies of SOM (AS with AA and SA) and proxies of sea spray aerosol particles (mixture of Na, Mg, K and Ca chlorides as well as NaCl mixed with MA). Particle heterogeneity was determined using AFM, Raman maps and SEM/EDX maps. Our results show that hygroscopicity behavior of some mixed particles

depends on their size. Interestingly, it was determined that particles composed of AS with SA and of marine chloride mixture typical for marine environment show different hygroscopicity behavior at different sizes that can be related to differences in morphology.

Very often studies of hygroscopicity of atmospherically relevant particles are performed on supermicron particles. However as shown here, hygroscopicity for some particles depend on particle size. Smaller particles in accumulation mode are more typical for long-range transported aerosol. For systems studied here that show size dependent hygroscopicity behavior submicron particles have lower deliquescence and efflorescence RH values than larger particles. Adsorbed water plays important role in the reaction chemistry and therefore revealed morphology dependent hygroscopicity has consequences for heterogeneous atmospheric chemistry as well as for scattering and absorbing solar radiation, and cloud condensation nuclei activity. These results help us better understand the role of aerosol particles in heterogeneous atmospheric chemistry and the Earth's climate system.

5. QUANTIFYING THE HYGROSCOPIC GROWTH OF SUBMICROMETER PARTICLES WITH ATOMIC FORCE MICROSCOPY*

5.1 Abstract

The water uptake behavior of atmospheric aerosol dictates their climate effects. In many studies, aerosol particles are deposited onto solid substrates to measure water uptake, however, the effects of the substrate are not well understood. Furthermore, in some cases, methods used to analyze and quantify water uptake of substrate deposited particles use a two-dimensional (2D) picture of particle to monitor growth by following changes in the particle diameter with relative humidity (RH). However, this 2D analysis assumes that the droplet grows equally in all directions. If particle growth is not isotropic in height and diameter, this assumption can cause inaccuracies when quantifying hygroscopic growth factors (GFs), where GF for a for a spherical particle is defined as the ratio of the particle diameter at a particular relative humidity divided by the dry particle diameter (typically about 5% RH). However, as shown here, anisotropic growth can occur in some cases. In these cases, a three-dimensional (3D) analysis of the growth is needed. This study introduces a way to quantify the hygroscopic growth of substrate deposited particles composed of model systems relevant to atmospheric aerosols using atomic force microscopy (AFM) which gives information on both the particle height and area and thus a three-dimensional view of each particle.

In this study, we compare GFs of submicrometer sized particles composed of single component sodium chloride (NaCl) and malonic acid (MA), as well as binary

* Adapted from Morris, H. S.; Estillore, A. D.; Laskina, O.; Grassian, V. H.; Tivanski, A. V. *Anal. Chem.* Copyright (2016), 88, 3647-3654.

mixtures of NaCl and MA, and NaCl and nonanoic acid (NA) determined by AFM using area (2D) equivalent diameters, similar to conventional microscopy methods, and compared to GFs determined using volume (3D) equivalent diameter. We also compare these values to GFs determined by a hygroscopic tandem differential mobility analyzer (HTDMA) (substrate free, 3D method). It was found that utilizing volume equivalent diameter for quantifying GFs with AFM agreed well with those determined by substrate-free HTDMA method, regardless of particle composition but area equivalent derived GFs varied for different chemical systems. Furthermore, the NaCl and MA mixture was substrate-deposited both wet and dry, revealing that the hydration state of the particle at the time of impaction influences how the particle grows on the substrate upon water uptake. Most importantly, for the binary mixtures different populations of particles can be distinguished with AFM, an individual particle method, whereas HTDMA sees the ensemble average. Overall, this study establishes the methodology of using AFM to accurately quantify the water uptake of individual submicrometer particles at ambient conditions and over a wide range of RH values. Furthermore, the importance of single particle AFM analysis was demonstrated

5.2 Introduction

Understanding water uptake of atmospheric particles is important in order to determine the climate effects of aerosols.¹³⁷ Hygroscopic growth refers to the change in size due to the uptake of water upon changing relative humidity (RH) and is dictated by the chemical composition of the aerosol. Hygroscopicity affects particle morphology,¹³⁸ cloud condensation nuclei activity,¹³⁹ and heterogeneous reactions.¹¹⁸ In addition, particle size changes upon absorbing or releasing water and therefore, alters how the particle

scatters solar radiation.¹³⁸ The quantification of change in the size of a particle due to water absorption or release is called a growth factor (GF) and is defined by Equation 5.1, where $D(RH)$ is the diameter of the particle at a particular RH and D_0 is the diameter of the dry particle

$$GF(RH) = \frac{D(RH)}{D_0} \quad (\text{Eq. 5.1})$$

A common method for studying hygroscopic growth of particles is by using a hygroscopic-tandem differential mobility analyzer (HTDMA).^{137,140–142} HTDMA quantifies water uptake by measuring aerosol size distribution at varying RH. While this method has proven to be reliable, it is limited by the fact that, for a heterogeneous population of particles, the measurement yields an ensemble average of thousands of particle measurements, and doesn't allow careful examination of the extremes of the distribution that are not accurately represented by the average. Thus, it is important to understand particle composition and hygroscopic properties at the single particle level.^{98,143–146} Furthermore, HTDMA is generally restricted to relatively small particle size (<300 nm) due to limitations of the differential mobility analyzer.^{147–150} Raman microspectroscopy (RMS),^{31,151,152} micro-FTIR spectroscopy,³² optical microscopy (OM),^{25,153,154} environmental scanning electron microscopy (ESEM),^{143,155–158} environmental transmission electron microscopy (ETEM),¹¹⁴ and scanning transmission X-ray microscopy (STXM)^{32,159–161} are all established methods capable of giving water uptake data on a single particle basis. Unlike HTDMA, these techniques require particle deposited onto substrates. Work has been performed addressing the effect of the substrate¹⁶² on hygroscopic growth of single particles both experimentally⁷² and theoretically.¹⁶³ Droplets on a substrate are typically aspherical; thus, droplet growth

upon water absorption can be asymmetric and anisotropic along axes within the substrate plane as well as perpendicular to it. Consequently, GFs determined using only 2D diameter changes could be inaccurate.^{72,155} Critically, none of these single particle microscopy techniques discussed here are able to provide direct 3-dimensional (3-D) growth information of submicrometer particles under ambient conditions that is needed to accurately quantify and compare GFs. We note, ESEM can indirectly estimate the volume equivalent diameter of hydrated particles by tilting the samples stage. However, tilting the sample stage can be problematic, causing droplets to move, thus potentially modifying their 3D shape and size.¹⁵⁸

The composition of the particle and the hydrophobicity of the substrate dictate the contact angle of the droplet with the substrate and influence the shape of the droplet (i.e. spherical, half-ellipsoidal). Matsumura et al. used ESEM to measure the contact angle of an ammonium sulfate droplet on a hydrophobic copper substrate in order to calculate a volume equivalent diameter.¹⁵⁸ The results showed that the droplets were spherical cap shaped and the calculated volume equivalent diameter returned GFs that were in agreement with predicted values and were approximately 30% lower than GFs determined by using 2D projected area equivalent diameters, demonstrating the potential inaccuracy of using only 2D data to quantify hygroscopic growth.

In this study, atomic force microscopy (AFM) is established for the first time as quantitative means to study the hygroscopic GFs of individual substrate deposited submicrometer particles. AFM is a highly suitable technique to study hygroscopic growth because it uniquely offers imaging resolution down to the nanometer level, does not require vacuum conditions, can operate under ambient pressure at controlled RH, and

provides direct 3D images of the particles; all of which make it superior to other types of microscopy such as OM, FTIR, RMS, ESEM, ETEM and STXM for morphological studies of individual submicrometer particles. Studies reporting AFM imaging of individual submicrometer sized liquid particles at varying RH are relatively rare.⁹ Bruzewicz et al. examined the formation of a water layer around sodium chloride (NaCl) particles using AFM but did not probe the system at humidity values above deliquescence RH (~75% RH).¹⁶⁴ The lack of AFM data in the literature is likely because imaging at high RH and furthermore, imaging liquid droplets, is difficult due to high capillary forces between the AFM probe and the sample that can cause difficulties in obtaining an image and can rupture the droplets.

For this study, model systems relevant to atmospheric aerosols were analyzed in order to assess the accuracy of AFM growth factor determination. Single component inorganic and organic model systems were composed of NaCl and malonic acid (MA), respectively. NaCl is a major constituent of aerosol generated from breaking ocean waves^{44,56,165} and dicarboxylic acids, like MA, have been found prevalently in atmospheric aerosols.¹⁶⁶⁻¹⁶⁸ More complex model systems consisting of both NaCl and organic species, however, are more realistic of particles originating in the ocean.^{47,169} Therefore, two component model systems composed of NaCl and MA (NaCl/MA, 2:1 mole fraction), and NaCl and nonanoic acid (NA) (NaCl/NA, ~6:1 mole fraction) were studied. The solubility of MA is much higher than the solubility of NA, which is expected to affect the water uptake properties of the particle.¹⁷⁰ Long chain insoluble molecules reside at the ocean-air interface¹⁷¹ and are thought to be enriched in sea spray aerosol (SSA) relative to the bulk seawater. Noteworthy, these two mixtures also have

different particle morphology as demonstrated below. To investigate the accuracy of the AFM method, both 2D and 3D GFs were determined for each model system and compared to GFs determined by HTDMA. Furthermore, to study the effect of particle viscosity upon impaction, NaCl/MA particles were deposited both dry and wet and it has been determined here that the extent of hydration of the particles at the time of impaction affects how the particles grow upon water uptake. The NaCl/NA system was used to give information about how particle morphology affects the growth of droplets on the substrate.

5.3 Experimental

5.3.1 Substrate deposited particles.

All chemicals used were purchased from Sigma Aldrich (reagent grade, 99.99% purity) and prepared in deionized water (18 M Ω ·cm). For AFM studies, aqueous solutions containing model compounds were atomized with a constant output atomizer (TSI, Inc., model 3076), dried by passing through a diffusion dryer (TSI, Inc., model 3062), and impacted onto hydrophobically coated (polysiloxanes) silicon wafers (Ted Pella Inc., part no. 16008), after size-selection with a 10 stage rotating micro-orifice uniform deposit impactor (MOUDI) (MSP Corp., model 110). Particles were deposited on stage 6 of the MOUDI, corresponding to particles with an aerodynamic diameter of 0.56 – 1.0 μ m. NaCl and MA solutions were approximately 0.2 M and 0.1 M, respectively. The NaCl/NA solution was made from a 6:1 NaCl:NA molar ratio solution (0.2 M NaCl). The solution was shaken to dissolve as much NA as possible; however, NA is an oily liquid and did not completely dissolve. For deposition of wet NaCl/NA

particles, the diffusion dryer was bypassed and particles were collected directly from the atomizer.

5.3.2 Hygroscopic Tandem Differential Mobility Analyzer (HTDMA)

HTDMA measurements of the hygroscopicity as a function of increasing RH at 298 K were performed using a Multi-Analysis Aerosol Reactor System (MAARS), which has been described in detail elsewhere.¹¹⁸ For these measurements, dehydrated aerosol particles (<10% RH) were size-selected at 100 nm with a differential mobility analyzer (DMA; TSI, Inc. Model 3080). The monodispersed aerosol stream was directed into the hydration chamber where it was equilibrated at different RH values. The RH can be adjusted by varying the ratio of wet and dry air supplied by a commercial dry air generator (Parker Balston, Model 75-62). A portion of the dry air was sent through a bubbler to humidify. The dried aerosol and humidified air are combined in the hydration chamber. Then the aerosol particles were directed to a scanning mobility particle sizer (SMPS; TSI, Inc. Model 3936) that consists of a DMA (TSI, Inc., Model 3080) and a condensation particle counter (CPC; TSI, Inc. Model 3025A) where size distribution of the humidified aerosol is measured. Size distribution data were fit to Gaussian curve to obtain particle diameters. NaCl/NA acid particles, generated from the same solution mentioned previously, were size selected at 100 and 200 nm and deposited on substrates for AFM imaging.

5.3.3 Atomic Force Microscopy (AFM) and water uptake

Hydrophobically coated silicon wafers containing substrate deposited particles were placed in an AFM humidity cell setup, which is described elsewhere.⁵⁷ Images were collected in AC mode with silicon nitride AFM probes (MikroMasch, Model

CSC37) with a nominal spring constant of 0.35 N/m and a typical tip radius of curvature of 10 nm. For quantifying water uptake at a specific RH, images were taken at low RH (<5%) and again at high RH (>75%), allowing at least 15-20 minutes equilibration time for water uptake at high RH. To obtain hydration and dehydration curves, the RH was changed stepwise and an image was collected at each RH. The free amplitude and set point used for imaging the liquid particles at high RH were relatively large (3-5 V) to achieve optimal imaging without moving or breaking the droplets. Scan rates were between 1.0 – 1.3 Hz. Repeated imaging of the sample area at high RH can be problematic and the data were obtained using the least amount of imaging possible. Area and volume equivalent diameters were determined using build-in Asylum Research particle analysis software for all systems except NaCl. Since NaCl has abrupt and steep features due to its cubic nature, AFM images were not well resolved around the edges of the particles and the volume was found by cross-sectional analysis. GF data is reported as the mean value and error bars represent two standard deviations obtained from typically four individual droplet measurements.

5.4 Results and Discussion

Quantifying hygroscopic GFs of atmospheric particles facilitates determination of their role in cloud formation and RH dependent size and physical phase changes. For field studies, it is often times convenient to deposit particles on substrates for future offline analysis. However, it is not clear if the GFs measured for particles remain free of substrate effects during water uptake or release. Thus, it is not clear if the substrate deposited particle quantification can be directly compared to methods like HTDMA that measure hygroscopic growth of particles without the presence of a substrate and

therefore, if measurements on substrates are comparable to aerosol in the real world that are suspended in the gas phase. This study addresses several phenomena associated with substrate deposited particle growth upon water uptake that can influence the quantification of GFs including: rapid or slow deliquescence and local modification of the substrate due to spreading upon particle impaction, which, we show, depends on the extent of hydration of the particle at the time of collection. AFM has the unique ability to directly measure changes in submicrometer particle growths in three dimensions, allowing 2D and 3D GFs to be quantified and compared simultaneously for different individual particles at varying RH.

Because of the importance and abundance of NaCl in sea spray aerosol (SSA), the hygroscopic growth of individual substrate deposited NaCl particles was quantified with AFM and compared to the value determined by HTDMA. Figure 5.1A shows 3D AFM images of a representative NaCl particle at 5% RH and deliquesced droplet at 80% RH. The morphology of NaCl consists of cubic structure and becomes a round liquid droplet above the deliquescence RH (75%).^{117,163} The area equivalent GF at a particular RH was quantified by determining the 2D projected area of the particle and liquid droplet. Area equivalent diameter, $D_{Area}(RH)$, was then calculated using Equation 5.2, which solves for the diameter of circle from the projected area, $A(RH)$, at a corresponding RH. Area equivalent GF at a particular RH, $GF_{Area}(RH)$, is defined as the ratio of the area equivalent diameter at that RH to the area equivalent diameter at ca 5% RH (Equation 5.3).

$$D_{Area}(RH) = 2 \sqrt{\frac{A(RH)}{\pi}} \quad (\text{Eq. 5.2})$$

$$GF_{Area}(RH) = \frac{D_{Area}(RH)}{D_{Area}(5\%)} \quad (\text{Eq. 5.3})$$

Volume GF determined by AFM is calculated from the particle volume, $Vol(RH)$, at a particular RH. This quantification, as we demonstrate below, is inherently more accurate because it takes into account the substrate effects that may cause the particle to grow unequally in height *versus* diameter as it absorbs water. The volume equivalent diameter at a particular RH is calculated as the diameter of a sphere with the same volume (Equation 5.4). Volume GF, $GF_{Vol}(RH)$, is defined by Equation 5.5, which is the ratio of the droplet volume equivalent diameter, $D_{Vol}(RH)$, to particle volume equivalent diameter at ca 5% RH, $D_{Vol}(5\%)$.

$$D_{Vol}(RH) = \sqrt[3]{\frac{6Vol(RH)}{4\pi}} \quad (\text{Eq. 5.4})$$

$$GF_{Vol}(RH) = \frac{D_{Vol}(RH)}{D_{Vol}(5\%)} \quad (\text{Eq. 5.5})$$

Figure 5.1B shows cross sectional analysis of a NaCl particle (red line) at 5% RH and the corresponding liquid droplet (blue line) at 80% RH. The cross sectional analysis demonstrates how AFM can directly observe the particle growth due to water uptake in three dimensions, which is a unique feature compared to other type of microscopy techniques like OM, SEM and TEM and allows direct determination of a volume GF. The results of AFM area (1.76 ± 0.10) and volume GF (1.96 ± 0.16) quantification for NaCl are reported in Figure 5.1C and Table 5.1, and compared to the GF determined by HTDMA (2.06 ± 0.01).

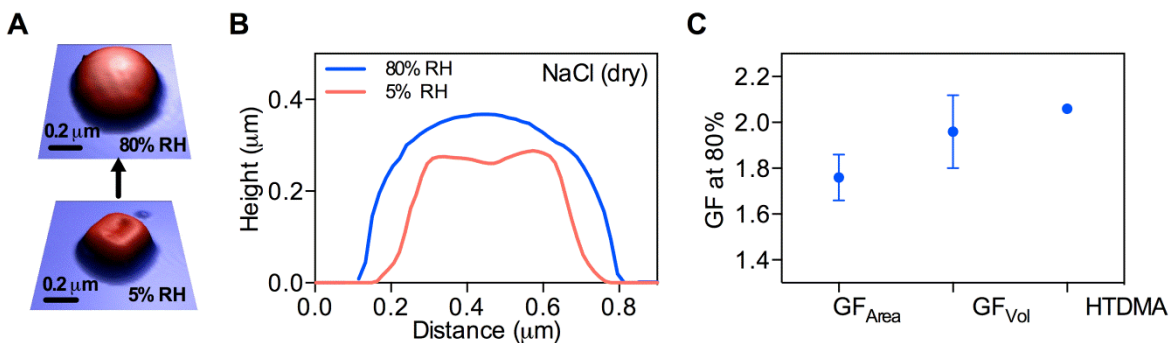


Figure 5.1: A. NaCl dry deposition results. A. 3D AFM images of a NaCl particle at 5% RH and corresponding deliquesced liquid droplet at 80% RH. B. Cross section of particle at 5% RH (red) and corresponding deliquesced liquid droplet at 80% RH (blue). C. Comparison plot of average and two standard deviations of GF determined with AFM area, volume, and HTDMA approaches. Error bar for HTDMA is less than the size of the data symbol. HTDMA data was collected by Armando Estillore (Grassian group, University of Iowa).

Table 5.1: Average and standard deviation of area and volume GFs determined with AFM and compared with the GF determined by HTDMA ($298 \pm 2K$). HTDMA data was collected by Armando Estillore (Grassian group, University of Iowa).

System (RH (%))	GF _{Area}	GF _{Vol}	HTDMA
NaCl (80 ± 2) (Dry deposition)	1.76 ± 0.10	1.96 ± 0.16	2.06 ± 0.01
MA (75 ± 2) (Dry deposition)	1.20 ± 0.09	1.35 ± 0.07	1.37 ± 0.02
NaCl/MA (80 ± 2) (Dry deposition)	1.00 ± 0.02	1.69 ± 0.04	1.69 ± 0.01
NaCl/MA (76 ± 2) (Wet deposition)	1.55 ± 0.23	1.59 ± 0.09	1.56 ± 0.01
NaCl/NA (77 ± 2) (Wet deposition)	1.70 ± 0.06	1.70 ± 0.04	1.69 ± 0.01

Area GFs are clearly lower than the GF determined with HTDMA, while volume GFs that take into account changes in particle height as well as diameter, are in agreement with the GF determined by HTDMA. A combination of the hydrophobic substrate and deformation of the NaCl particle due to impaction upon the substrate likely explains why the area GF is less accurate than the volume GF. The NaCl aerosol was dried before impaction, so it is assumed that the viscosity of the particles was high at the

time of impaction, leading to minor deformation and spreading of the particle within the substrate plane, which can be seen in the red cross-sectional profile in Figure 5.1B. No significant water uptake takes place until $\sim 75\%$ RH, at which a sharp phase transition occurs and particles rapidly uptake a substantial amount of water, resulting in the particle spreading laterally on the substrate, as well as vertically, as shown above. The diameter grows until the edges of the droplet come in contact with the hydrophobic substrate, at which point it's more energetically favorable for the particle to grow more in the vertical direction as compared to lateral spreading along the substrate. The preferential growth in height causes the area GF that is slightly smaller than the volume GF and HTDMA GF.

Since organic species are also an important component of SSA, we did similar analysis for a single component MA model system. Figure 5.2A shows 3D AFM images of a representative MA particle at 5% RH and deliquesced liquid droplet at 75% RH. For MA, both low and high RH particles have rounded morphology. Area and volume GF were determined analogous to that described for NaCl (Equations 2-5).

Representative cross-sectional analysis in Figure 5.2B shows how the MA particle grows upon water uptake. Similar to NaCl, MA particles were dried prior to impaction and are assumed to be viscous droplets at the time of deposition. Interestingly, it is apparent that the droplet grows in height but hardly at all in diameter. Consequently, as seen by the GF quantification in Figure 5.2C and reported in Table 5.1, this phenomena causes area equivalent GFs determined by AFM to be severely underestimated in comparison to the HTDMA GF. The observed preferential height growth for this system is noticeably different from NaCl above and likely because water uptake for MA is a continuous process starting from about 30% RH, allowing the particle sufficient time to

restructure into a minimum energy shape, which apparently is to expand the air-liquid interface and not spread on the substrate. Comparatively, NaCl is likely solid at 5% RH and the deliquescence process of NaCl is much more rapid and causes lateral and vertical droplet growth.

A more relevant model system of aerosols generated from the ocean is a mixture of NaCl and organic species. Therefore, a third model system composed of NaCl and MA was studied. It has been observed that some mixtures of salts with organics can result in particles that have core-shell or partially engulfed morphology. However, the mixture of NaCl and MA studied here results in homogeneously mixed particles and hygroscopic growth does not vary with particle size for this mixture.³¹ This mixture was deposited dry (~20% RH) and hydrated (RH estimated as ~40 – 60%) to compare how the hydration state at the time of impaction affects the hygroscopic growth. The RH in the atmosphere varies greatly depending on location and season.¹⁷² Consequently, during field studies, particles may not always be collected at the same RH. In addition, for laboratory studies, the aerosol is often times passed through a diffusion dryer before collection, which removes the majority of the water from sample (diffusion dryer is ~20% RH). The extent of hydration of the particle is highly dependent on the RH of the surrounding environment, as well as chemical composition of the aerosol. This is important because the hydration state dictates physiochemical properties like viscosity,¹⁷³ surface tension,⁹ and morphology.¹⁷⁴ Therefore, the RH at the time of collection can change how the particles spread upon impacting onto the substrate.¹⁷⁵ For example, a wet aerosol particle will likely spread on the surface upon impaction because it has a relatively low viscosity (compared to solid or semi-solid particles). Depending on the

composition, after spreading, the particle will either restructure back to round particle to minimize surface area or if it is highly viscous, it will remain spread on the surface. On the other hand, if the particle is fully dried, it is most likely solid at the time of impaction and will not spread but suffer minor deformation primarily due to the force of colliding with the substrate surface. The manifestation of both spreading of the particles and minor deformation is evident in AFM aerosol studies because the area equivalent diameter of the particles is usually greater than the height.

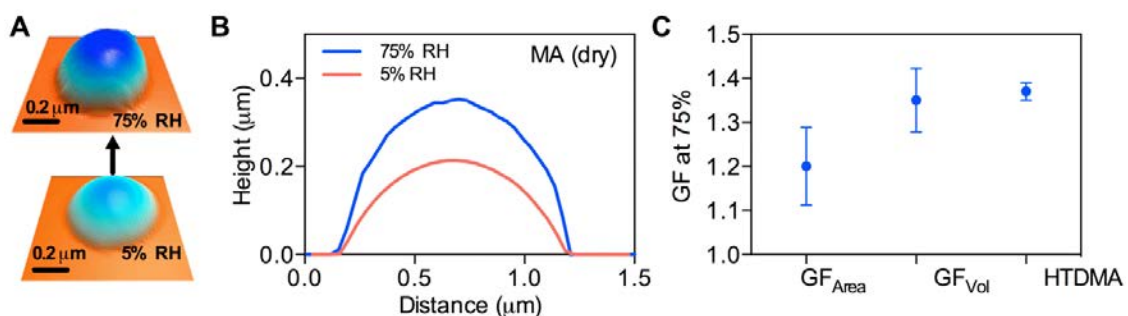


Figure 5.2: MA dry deposition results. A. 3D AFM images of a MA particle at 5% RH and corresponding deliquesced liquid droplet at 75% RH. B. Cross section of particle at 5% RH (red) and corresponding deliquesced liquid droplet at 80% RH (blue). C. Comparison plot of average and two standard deviations of GF determined with AFM area, volume, and HTDMA approaches. HTDMA data was collected by Armando Estillore (Grassian group, University of Iowa).

Figures 5.3A and B show 3D AFM images phase images and cross sectional analysis, respectively, of two component NaCl/MA mixed particles that were deposited dry and the corresponding droplet at 80% RH. The GF quantification results are reported in Table 5.1 and Figure 5.3C. The growth of the particles upon water uptake is similar to the pure MA system; the particles grow preferentially in height and do not spread on the substrate. This results in area GFs determined by AFM that are significantly lower than

that by HTDMA and AFM volume GFs that agree well with substrate free, HTDMA quantification.

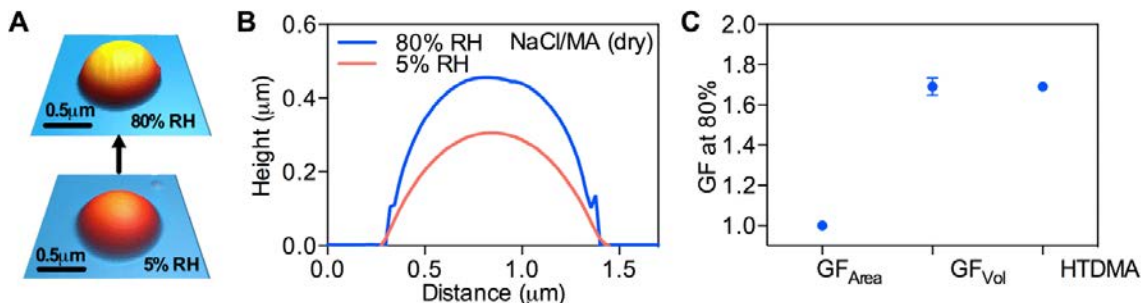


Figure 5.3: NaCl and MA dry deposition results. A. 3D AFM images of a particle at 5% RH and corresponding deliquesced liquid droplet at 80% RH. B. Cross section of particle at 5% RH (red) and corresponding deliquesced liquid droplet at 80% RH (blue). C. Comparison plot of average and two standard deviations of GF determined with AFM area, volume, and HTDMA approaches. Error bar for HTDMA is less than the size of the data symbol. HTDMA data was collected by Armando Estillore (Grassian group, University of Iowa).

The same two component NaCl/MA mixture was prepared by bypassing the diffusion dryer and deposited onto the substrate, presumably, still hydrated. The particles (Figure 5.4A bottom) spread on the substrate upon impaction and then restructured to this morphology. Evidence of the spreading phenomena is apparent by a ring of residue surrounding the particles in the representative phase image in Figure 5.4B (bottom image). The phase shift of the cantilever during AC mode imaging and color change in the phase image is primarily caused by a difference in chemical nature of the sample. The thin coating of material surrounding the particle has a different phase response than the rest of the particle and the substrate. Interestingly, the particles deposited under humid conditions grew relatively uniformly in terms of height and diameter upon water uptake, as seen in Figure 5.4C, whereas the particles that were deposited dry preferentially grew in height and not diameter. Figure 5.4D and Table 5.1 report the

results of the GF quantification and it is apparent that all three methods gave similar average values. The difference in water uptake behavior of the dry and wet samples can be attributed to the hydration state and spreading during the impaction process. Wet particles spread on the substrate, which effectively coats the substrate immediately surrounding the particles with particulate residue of the same composition. Dry particles, on the other hand, impact and do not spread because the higher viscosity does not allow for much deformation. Upon absorbing water, it is favorable for the particles to grow in diameter because the surface is coated in the same material, whereas the dry deposited particles experience the hydrophobic substrate, which causes them to preferentially grow in height and not diameter, as we know in the case of MA particles. In other words, the substrate immediately surrounding wet deposited particles is no longer hydrophobic and the particles expand as easily in diameter as they do in height. The source of larger standard deviation for area GF most likely is due to differences in 3D growth that are not accounted for when only considering the 2D diameter changes.

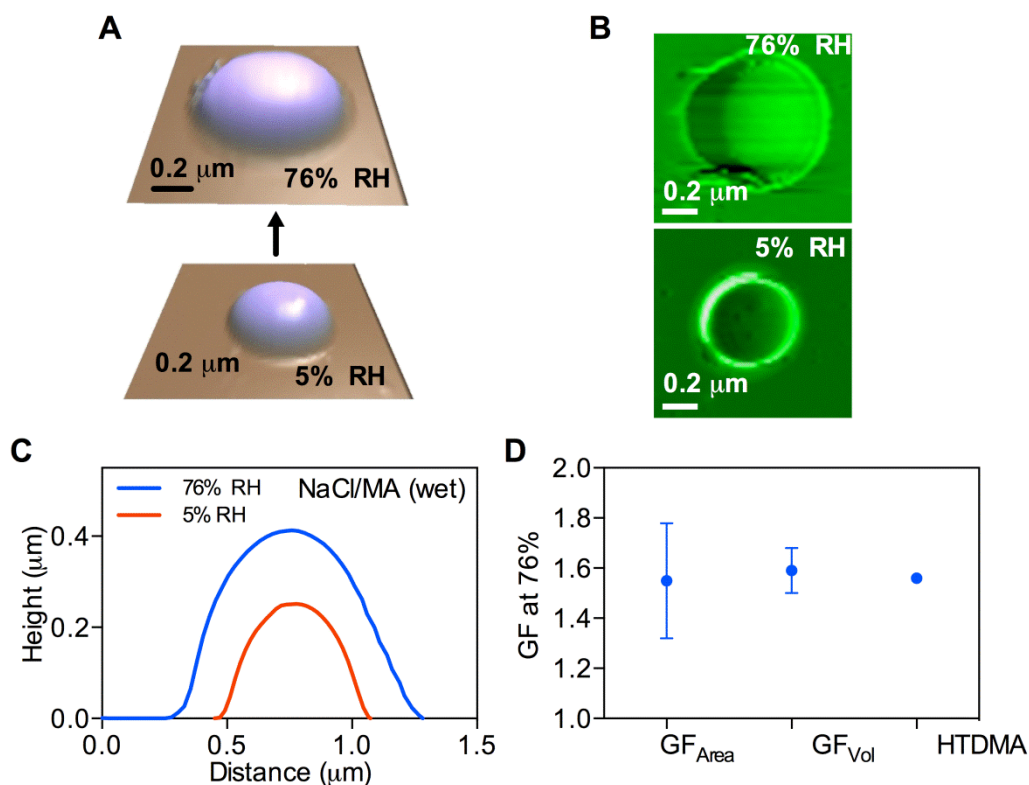


Figure 5.4: NaCl and MA wet deposition results. A. 3D AFM images of a particle at 5% RH and corresponding deliquesced liquid droplet at 76% RH. B. Phase AFM images of a particle at 5% RH and corresponding deliquesced liquid droplet at 76% RH. C. Cross section of particle at 5% RH (red) and corresponding liquid droplet at 76% RH (blue). D. Comparison plot of average and two standard deviations of GF determined with AFM area, volume, and HTDMA approaches. Error bar for HTDMA is less than the size of the data symbol. HTDMA data was collected by Armando Estilloro (Grassian group, University of Iowa).

Quantifying the GF of particles at a particular RH is important for determining the size of the aerosol and optical properties. However, there is also important particle phase transition information in hydration and dehydration curves. Using AFM to obtain these data quantitatively has not been established but is of importance because AFM can explore much smaller particle size ranges than many other microscopy techniques. Figure 5.5 shows hygroscopic growth curves for NaCl obtained with AFM and overlaid with HTDMA data. It is known that NaCl deliquesces at approximately 75% RH¹⁷⁶ and the AFM data is accurate in this respect. HTDMA and AFM growth curves agree well,

suggesting that AFM can be used to accurately obtain hydration curves. There are some minor differences in the dehydration curves, however. Efflorescence is a complex phenomenon because it is a kinetically controlled process that can be initiated by many factors; in our case, the substrate or interaction force of the AFM tip during imaging can cause efflorescence. Consequently, reported efflorescence RH (ERH) values in the literature for NaCl span the range of ~40 - 50%.¹⁷⁶ The observed AFM ERH of 44% falls within this reported range but it should be noted that it is possible to induce particle crystallization during imaging from the contact of the AFM probe.

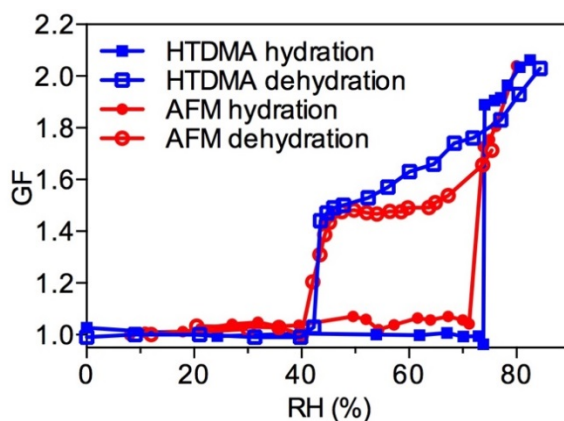


Figure 5.5: Hydration/dehydration GF curves of NaCl obtained using single particle AFM measurements (red data) and HTDMA (blue data). Hydration curves are closed symbols and dehydration curves are open symbols. HTDMA data was collected by Olga Laskina (Grassian Group, University of Iowa).

Overall, this methodology is applicable to a wide variety of aerosol composition, size, and chemical complexity. One unique feature of utilizing AFM for water uptake studies is the ability to observe single particle 3D morphology with corresponding hydration data for a wide range of particle sizes (~10 nm – 2 μ m). Sea spray aerosol is often a complex mixture of particle types with diverse composition and concentration of chemical species⁵⁶ that give rise to particles with different morphologies⁴⁴ and different

hygroscopicity.¹⁷⁷ It was observed in this study that even a simple binary mixture consisting of a relatively insoluble organic species, nonanoic acid (NA), with NaCl results in particles with different hygroscopicity, arising from heterogeneity in the amount of organic and inorganic species in each particle. Furthermore, we observed that particles that were size selected at 100 and 200nm were homogenous (results are not shown), while relatively larger (0.5 – 1.0 μm) NaCl/NA particles were more diverse in terms of morphology, as illustrated below.

Figure 5.6A shows a distribution of volume GFs measured for 40 individual NaCl/NA particles (0.5 – 1.0 μm in (dry) size) with AFM. The most probable AFM volume GF and area GF values of 1.70 ± 0.04 and 1.70 ± 0.06 , respectively, were determined from a Gaussian fit to the distribution of GFs and both are in agreement with the HTDMA GF value of 1.69 ± 0.01 . However, while AFM returns a distribution of GFs, HTDMA gives one value that represents the entire population of thousands of particles, which is often disadvantageous for complex samples. AFM analysis, on the other hand, can identify a sub-population of particles that do not behave like the majority of particles and therefore, are not accurately represented by the most probable value.

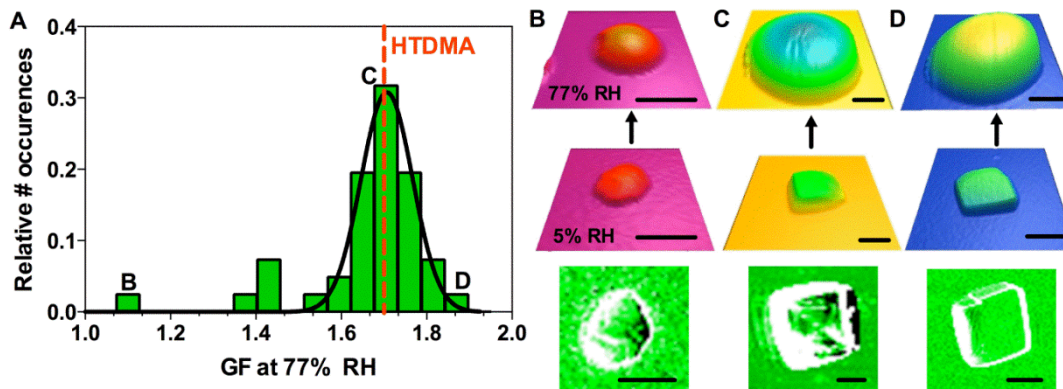


Figure 5.6: A. Volume GF distribution measured for 40 individual NaCl/NA particles. The data was fit to a Gaussian distribution. The red dashed line labels the GF value determined with HTDMA. Letters correspond to particles shown in B-D. B-D. The middle row of images shows dehydrated particles at 5% RH and corresponding deliquesced liquid droplets at 77% RH are shown above. The bottom row is phase images. B corresponds to the extreme left side of the distribution of GFs, while C corresponds to the most probable GF value and is representative of the majority of particles. D corresponds to the extreme right side of the GFs distribution. All scale bars are 500 nm. HTDMA data was collected by Armando Estilloro (Grassian group, University of Iowa).

Based on the distribution of GFs reported for NaCl/NA, it was observed that one particle (out of 40 analyzed) only grew 1.1 times in size and thus, did not take up a significant amount of water compared to the majority of particles that grew to 1.7 times in size, and one particle had a relatively high GF of 1.9. Figure 5.6B-D shows single particle morphology (phase and 3D images) corresponding to the extreme edges of the GF distribution, as well as a representative particle with the most probable GF value. Interestingly, as seen in the phase images in Figure 5.6B-D (bottom row), the particle that does not absorb a significant amount of water does not have a well-defined cubic NaCl core. This suggests that the inorganic and organic species are more homogeneously mixed with likely high amount of organic species relative to inorganic, which suppresses water uptake. Furthermore, the particle that grows the most appears to have a thinner organic coating (Figure 5.6C) as compared to the majority of particles (Figure 5.6B), resulting in enhanced water uptake relative to the most probable value due to increased NaCl content. Suppression in GF with increasing organic coating on NaCl particles is a well-studied

phenomenon. For example, Hansson et al. studied NaCl/lauric acid coated particles and found that mass fractions (lauric acid to NaCl) of 0.01, 0.48, and 1.04 resulted in GFs (80% RH) of approximately 2, 1.5, and 1.3, respectively.¹⁷⁸ Thus, the more organic content associated with the particle the lower the GF. As demonstrated, NaCl/NA particles have varying hygroscopicity that likely arises from differences in the amount of organic and inorganic species in the particle - information that would be lost in an ensemble-averaged measurement of GFs of thousands of particles like HTDMA. This enables the opportunity to observe different particle populations in a complex heterogeneous mixture.

5.5 Conclusions

This study establishes AFM as a reliable and accurate method to quantitatively determine hygroscopic properties of substrate deposited submicrometer size aerosol particles. For all particles of different composition and various mixing and hydration states, AFM-determined 3D volume equivalent GFs agree well with the substrate-free HTDMA method. 2D area equivalent GFs determined by only considering diameter changes, however, showed significant deviations from the HTDMA results depending on the chemical nature of the sample as well as the hydration state at the time of impaction on the substrate. We have demonstrated that AFM has the ability to overcome and account for substrate effects that may be occurring with the ability to observe particle growth in all dimensions and these data can be collected for a wide range of RH, allowing full hydration and dehydration curves to be obtained. Furthermore, we demonstrate the importance of single particle AFM measurements. The ability to distinguish morphology and hygroscopicity simultaneously is powerful for chemically

complex atmospheric samples, where a small population of particles can have large implications on climate. For example, approximately only one out of one million particles has the ability to nucleate an ice crystal in the atmosphere.^{21,179} Ensemble averaged approaches that return one representative value of the most probable response would not have the ability to identify and measure the small percentage of particles that may be the most important (e.g. as in ice nucleation).

6. QUANTIFYING ORGANIC VOLUME FRACTION OF INDIVIDUAL SEA SPRAY AEROSOL PARTICLES

6.1 Introduction

The organic volume fraction of SSA is important because it dictates the particles physical and chemical properties that ultimately determine the particles' effect on the atmosphere. One of the factors that determine morphology of mixed organic/inorganic particles is surface tension.¹¹² Inorganic species tend to be more water soluble and have higher surface tension, while organic species are less hygroscopic and have lower surface tension.³³ Particles of mixed inorganic and organic species with drastically different surface tensions will under-go liquid-liquid phase separation, resulting in particles that have core-shell or totally phase segregated morphologies.¹²⁴ Typically, the species with lower air-liquid surface tension value exists in the shell of the particle (organic species), while the higher surface tension component remains in the core (usually inorganic species). These effects have important implications on atmospheric chemistry processes such as hygroscopicity,³¹ reactivity,¹⁸⁰ and morphology.¹²⁴

One of the disadvantages of AFM is that it provides no specific chemical characterization information. Thus, AFM alone cannot identify chemical species. One way to infer difference in chemical nature of a sample, however, is by monitoring phase shifts in tapping mode imaging. A phase shift in the image is a result of a lag between the excitation oscillation of the cantilever and the output oscillation associated with the tip interacting with the sample surface (Figure 6.1)

. Viscosity, chemical composition, adhesion force, and elasticity of the sample are among factors that can cause changes in the phase.^{105,106} Phase imaging therefore allows compositional contrast on heterogeneous surfaces and can reveal spatially resolved information of the sample surface that reflects differences in the physical state and/or chemical composition associated with a phase separated particle.

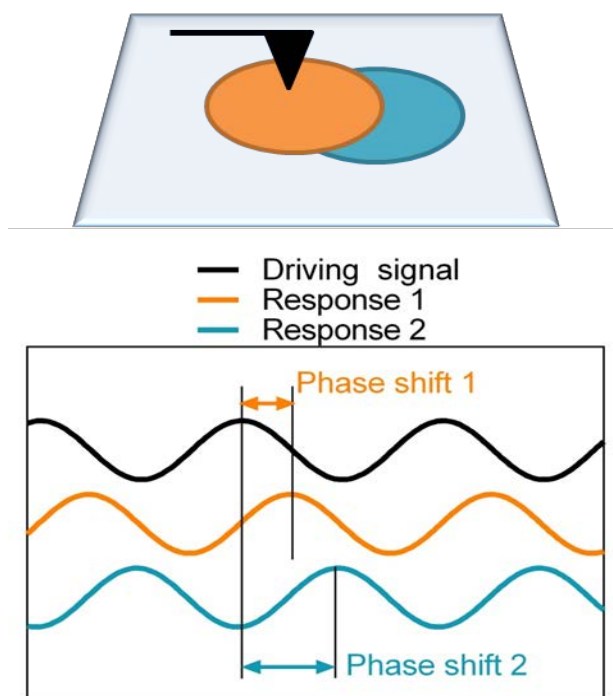


Figure 6.1: Schematic example of a phase shift that can occur during tapping mode AFM imaging. The orange and blue areas on the image represent areas on the sample that are chemically or physically different and cause different phase responses compared to the phase of the drive signal.

Interestingly, it was found that SSA particles display core-shell morphology in AFM phase images that is not observable in height images (Figure 6.2). When organic and inorganic species with different surface tensions mix, liquid-liquid phase separation occurs.⁹² The species with the lowest air-liquid surface tension tends to reside in the coating shell, while the higher surface tension species remains in the center of the

particle. Thus, the core and shell are often times composed of inorganic and organic species, respectively.⁴⁴ This unique morphology facilitates AFM based quantification of inorganic to organic ratio on a single particle basis. Presented here, is organic volume fraction analysis results of both model system and nascent individual submicrometer SSA particles. Furthermore, this method was corroborated with size resolved chemical composition analysis using gas-chromatography mass spectroscopy (GC-MS).

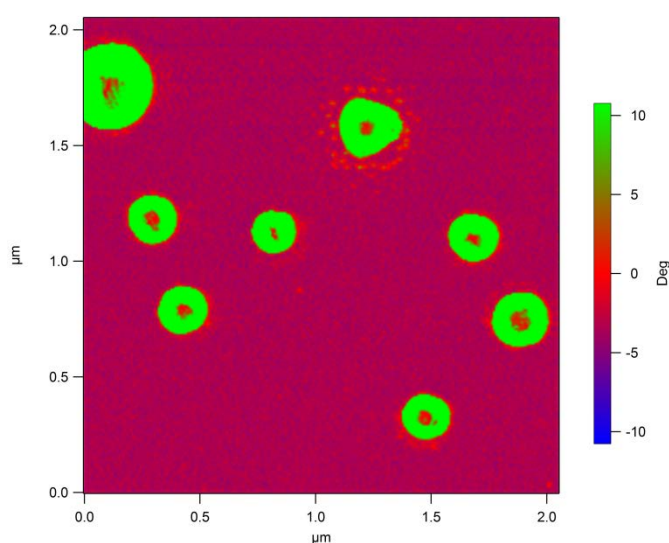


Figure 6.2: Phase image of SSA particles showing core-shell morphology.

6.2 Experimental

6.2.1 Organic volume fraction

AFM phase images were collected with silicon nitride AFM probes (MikroMasch, Model CSC37) with a nominal spring constant of 0.35 N/m and a typical tip radius of curvature of 10 nm. Phase images were used as a guide to draw masks on each particle, which were transferred to the height image for analysis. The height image with the overlaid mask was analyzed with Asylum Research particle analysis software (written by Jason Bemis). Particle volume, height, and area were obtained *via* this analysis.

Organic volume fraction is defined as the volume of the whole particle minus the volume of the particle core, relative to the whole particle volume. Figure 6.3 shows an example mask around the core of the particle (right) and the whole particle (left). This analysis assumes that the particle is homogeneous throughout (beneath) the core and the shell. Additionally, it assumes that the inorganic and organic phases are completely phase separated and not mixed. Considering these assumptions, this organic volume fraction analysis is likely an upper limit in terms of the amount of organic associated with the particles.

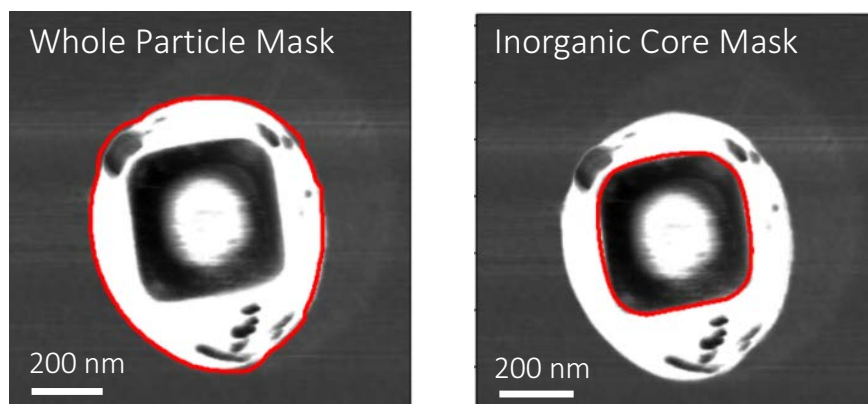


Figure 6.3: Representative AFM phase image of an SSA particle. The left images shows a typical mask surrounding the whole particle and the right shows the mask surround the particle core, used in determining organic volume fraction.

6.2.3 MART

SSA particles were collected from a synthetic phytoplankton bloom conducted in a MART tank. The details of the experiment and method of collection are the same as reported in sections 3.2.1 and 3.2.2.

6.2.3 IMPACTS

Nascent SSA particles were collected during a month long phytoplankton bloom waveflume experiment called the Investigation into Marine PArticle Chemistry and

Transfer Science (IMPACTS). The details of this experiment are reported elsewhere.¹⁵²

Particles were collected with a MOUDI onto hydrophobically coated silicon wafers.

6.3 Results and Discussion

6.3.1 MART

In January of 2013 a phytoplankton bloom experiment was conducted in a MART tank. Particles were collected over the progression of the bloom growth. The collected aerosol was analyzed with AFM for morphology and organic volume fraction. Figure 6.6 shows the progression of the phytoplankton bloom tracked by monitoring fluorescence and the sample collection dates that were analyzed. January 6th represents background, low phytoplankton growth, the 15th is at an intermediate progression of the bloom, the 17th is at the peak of the bloom and 22nd and 28th are after the bloom. Interestingly, it was found that the organic content of the aerosol particles increase steadily with time as the bloom progressed. This can be seen visually in the images in Figure 6.7. Samples collected on January 6th, 15th, and 17th seem to be mostly comprised of inorganics based on their morphology. January 22nd and 28th samples have noticeable organic residue and rings surrounding each particle.

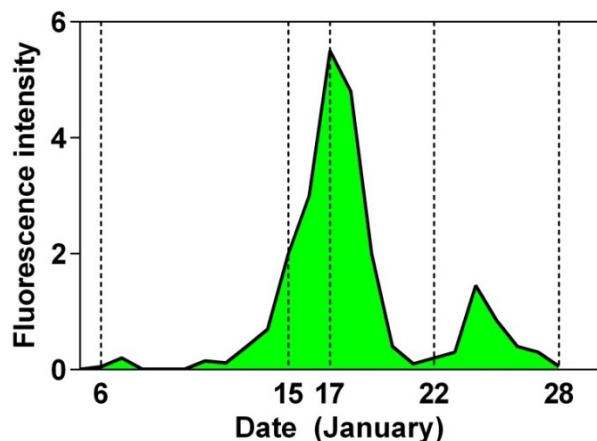


Figure 6.4: Chlorophyll-a measurement tracking the progression of phytoplankton bloom growth. The dates analyzed are labeled on the x-axis. Chl-a concentration measured via fluorescence intensity was measured by Olga Laskina (Grassian Group, University of Iowa) and Camille Sultana (Prather Group, University of San Diego, California).

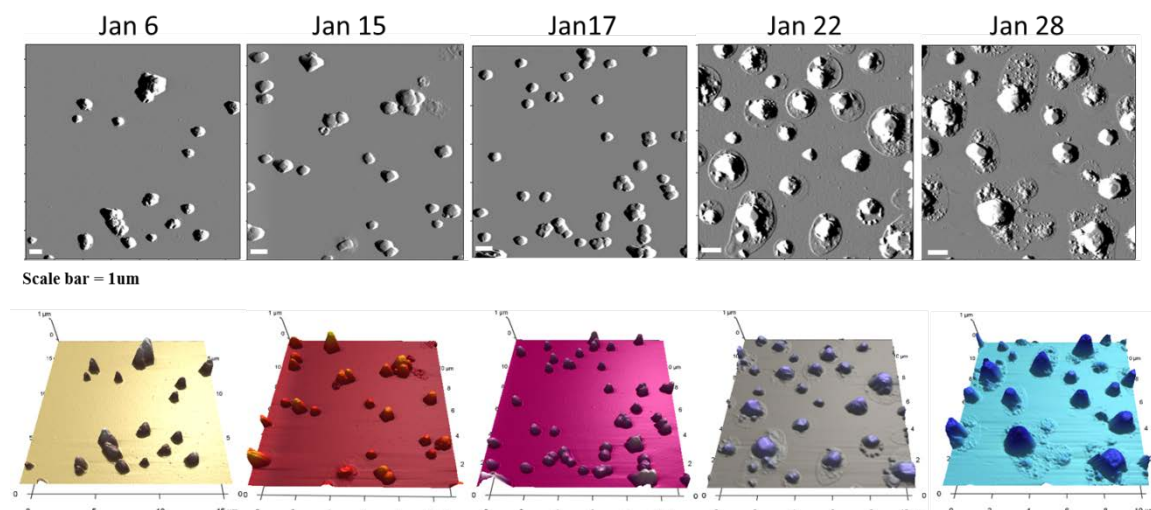


Figure 6.5: Amplitude (top) and 3D images (bottom) of the 5 sample collection days analyzed.

Organic volume fraction analysis was performed on a single particle basis and shows, numerically, the steady increase in organic content. Figure 6.8 reports the results plotted against the chl-a concentration. The organic volume fraction increases steadily over the progression of the phytoplankton bloom and continues to increase as the phytoplankton bloom dies. This reveals that measuring the metric of chl-a alone is not the best predictor of organic fraction in the aerosol. Wang, et al. revealed similar results

and determined that both chl-a and heterotrophic bacteria enzyme activity together are better predictors of the amount of organic in the aerosol.¹⁵²

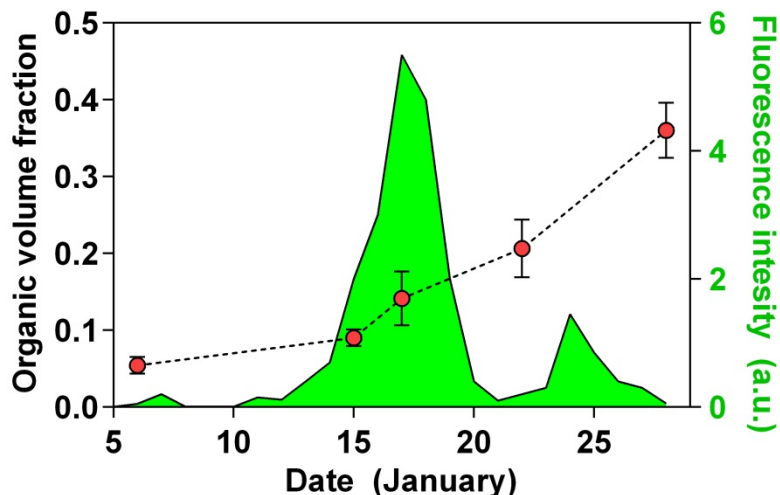


Figure 6.6: Organic volume fraction plotted over the chlorophyll-a fluorescence intensity tracking the progression of the phytoplankton bloom. Chl-a concentration measured via fluorescence intensity was measured by Olga Laskina (Grassian Group, University of Iowa) and Camille Sultana (Prather Group, University of California, San Diego).

6.3.2 IMPACTS

To further study the effects of ocean water biology on the organic content of the emitted aerosol the IMPACTS 2014 experiment was performed, which is the largest scale phytoplankton bloom experiment, reported to date.¹⁵² The progression of the phytoplankton bloom was monitored similarly as described for the MART experiment in the previous section by monitoring chlorophyll-a concentration. Uniquely, as seen in Figure 6.9, there were two distinct peaks in the phytoplankton bloom growth during the month long experiment. Furthermore, the two blooms ejected particles that were chemically different. Aerosol mass spectroscopy (AMS) data (blue data Figure 6.9) for submicron size particles revealed that the aerosol emitted during the first bloom was organically enriched compared to particles emitted during the second bloom growth.¹⁵²

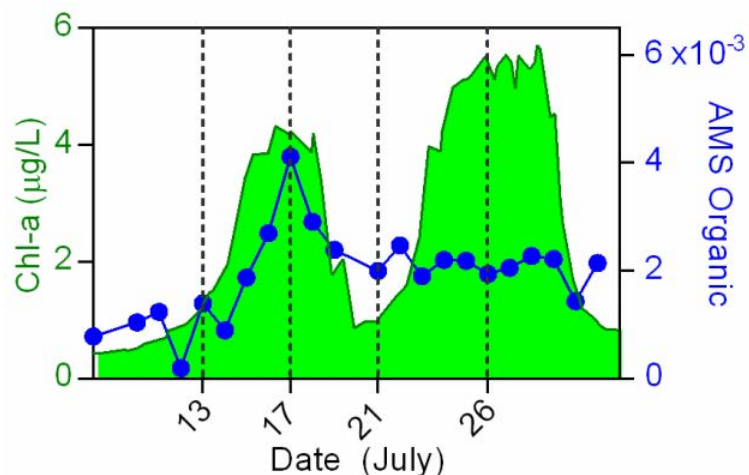


Figure 6.7: Phytoplankton bloom growth during the IMPACTS experiment was tracked by monitoring chl-a concentration (left axis). AMS data is plotted on top of chl-a trace, showing that the organic content of the aerosol increased for the first bloom but remained constant during the second bloom. Chl-a concentration measured was measured by Jon Trueblood (Grassian Group, University of Iowa) and Camille Sultana (Prather Group, University of California, San Diego). AMS Data was collected by Xiaofei Wang (Prather Group, University of California, San Diego).¹⁵²

The majority of particles have core-shell morphology. This morphology is apparent in AFM phase images, and a representative image is shown in Figure 6.10A. Organic volume fraction analysis of particles with sizes ranging from 0.5 – 1.0µm showed differences in the organic content of the particles during the progression of the phytoplankton bloom similar to the AMS data. Particles collected during the peak of the first bloom showed enhanced organic coating and then decreased and leveled out during the second bloom (Figure 6.10B). Chemical analysis reported by Wang et al. revealed that not only does the amount of the organic coating differ as the bloom progresses, but the type of organic changes as well.¹⁵² According to their findings, the first bloom produced aerosol that contained aliphatic rich organics, while the second bloom particles were enriched in oxygenated organics.

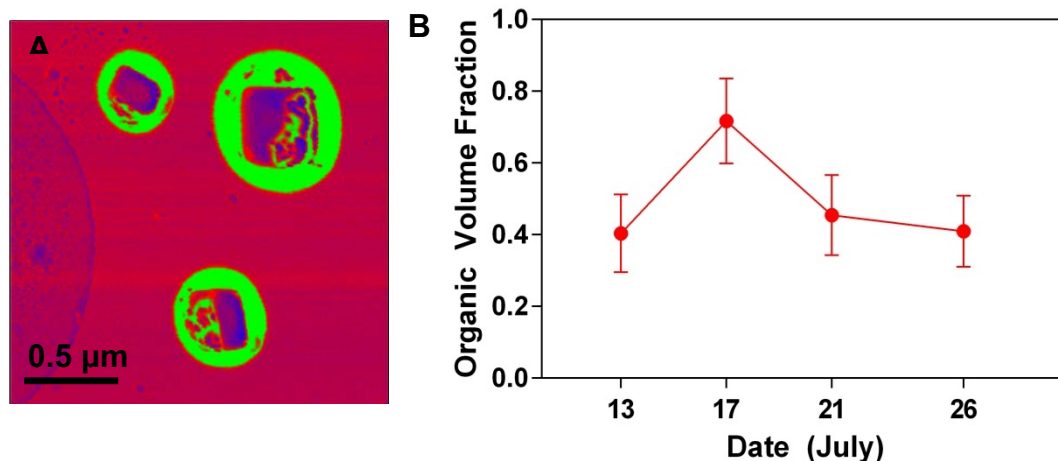


Figure 6.8: A. Representative phase image of core-shell particles collected during the experiment. B. Temporal variation of organic volume fraction for particles 0.5 – 1.0 μm in size. There is an increase in organic content of the aerosol on July 17th that coincides with the peak of the first bloom.

Furthermore, it is known that organic content of SSA can vary as a function of size.⁴⁵ Organic volume fraction as a function of particle size was analyzed for July 17th, see Figure 6.11. There is an apparent linear correlation between the particle size and the amount of organic with a negative slope. Thus, smaller particles have a relatively higher amount of organics.

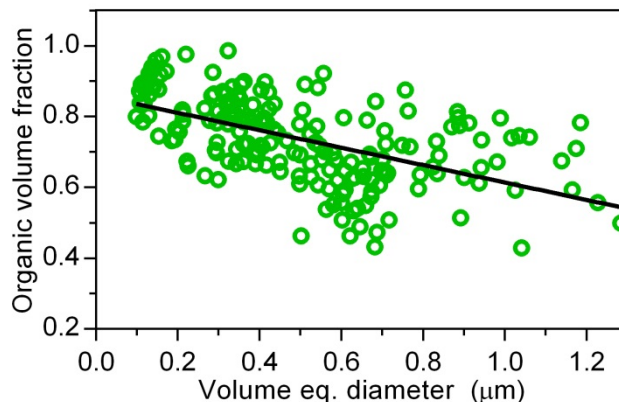


Figure 6.9: Organic volume fraction plotted as a function of volume equivalent diameter for July 17th sample.

6.4 Conclusions

Overall, the methodology of estimating the amount of organic content on a single particle basis with AFM is novel and very advantageous since the microscopy method, in general, provides no direct specific chemical composition information. This allows the potential to correlate the amount of organic fraction with other physiochemical properties of individual particles including but not limited to water uptake, surface tension, and size. The disadvantage of this method is that it is not applicable to particles that contain inorganic and organic species that are homogeneously mixed, as then there will be no obvious differences in the phase images.

What has been learned about SSA by this methodology so far has proven that the processes contributing to the chemical composition of the particles emitted from the ocean are complex and still are not fully understood. We have evidence that ocean biology does contribute to the amount of organic and inorganic species contained in the aerosol but the specific chemical details are still being unraveled. In this work we have observed trends in organic volume fraction that correlate differently with different phytoplankton bloom growths and differ for different methods (MART versus wave channel during IMPACTS). This suggests that there are different processes that can occur resulting in particles that likely have different compositions and/or that the experimental conditions promoted the particle differences. The concentration of species in the MART and IMPACTS experiments differed and produced particles of different concentrations as well.

7. HUMIDITY-DEPENDENT SURFACE TENSION MEASUREMENT OF INDIVIDUAL INORGANIC AND ORGANIC SUBMICROMETRE LIQUID PARTICLES*

7.1 Abstract

Surface tension, an important property of liquids, is easily measured for bulk samples. However, for droplets smaller than a micron in size, there are currently no reported measurements. In this study, atomic force microscopy (AFM) and force spectroscopy have been utilized to measure surface tension of individual submicron sized droplets at ambient pressure and controlled relative humidity (RH). Since the surface tension of atmospheric aerosols is a key factor in understanding aerosol climate effects, three atmospherically relevant systems (NaCl, malonic and glutaric acids) were studied. Single particle AFM measurements were successfully implemented in measuring the surface tension of deliquesced particles on the order of 200 to 500 nm in diameter. Deliquesced particles continuously uptake water at high RH, which changes the concentration and surface tension of the droplets. Therefore, surface tension as a function of RH was measured. AFM based surface tension measurements are close to predicted values based on bulk measurements and activities of these three chemical systems. Non-ideal behavior in concentrated organic acid droplets is thought to be important and the reason for differences observed between bulk solution predictions and AFM data. Consequently, these measurements are crucial in order to improve atmospheric climate

* Adapted from Morris, H. S.; Grassian, V. H.; Tivanski, A. V. Copyright (2015) Chem. Sci. 6, 3242–3247.

models as direct measurements hitherto have been previously inaccessible due to instrument limitations.

7.2 Introduction

The effect of aerosols on the earth's climate represents one of the biggest areas of uncertainty and understanding of factors that control our environment. Particles and liquid droplets in the atmosphere are chemically diverse,⁸² and they influence the radiative balance by scattering and absorbing solar radiation, and play an important role in cloud formation.^{181,24} One important property of aerosol droplets is surface tension, which is a key component in Köhler theory and climate models.^{181,30,182,116} For example, Equation 8.1 is the Kappa-Köhler expression that is utilized to determine the supersaturation ratio, S , over a droplet.¹³⁹ The value of surface tension of the droplet (σ) is an important component of the exponential term (other parameters are: d = droplet diameter, D_p = dry particle diameter, κ = hygroscopicity parameter, M_w = molecular weight of water, R = gas constant, T = temperature, ρ_w = density of water).

$$S = \frac{d^3 - D_p^3}{d^3 - D_p^3(1 - \kappa)} \exp\left(\frac{4\sigma M_w}{RT\rho_w d}\right) \quad (\text{Eq. 8.1})$$

Surface tension depression of aqueous particles relative to pure water due to the presence of organic species can alter the aerosol's ability to act as cloud condensation nuclei (CCN).^{30,183,184} Phenomena that may occur in submicron size liquid droplets such as interior concentration depletion due to surface partitioning of organic species^{30,183} and size effects¹⁸⁵ are still not well understood. Importantly, as addressed in detail here, there are no experimental methods that can directly measure the surface tension of droplets that are on the size range at or below one micron. Aerosols in this size range are highly important due to their prolonged life time in atmosphere.¹⁸⁶ Consequently, surface

tension values used in models are often times assumed to be that of pure water or that of concentrated bulk solution.¹⁸⁷ Realistically, these assumptions can cause inaccuracies, especially when considering water-soluble chemical concentration, and therefore, surface tension change as a function of relative humidity (RH)^{188,189} in the atmosphere, which varies greatly depending on location and conditions.¹⁷²

Particle size is a major factor and sometimes obstacle of understanding aerosol climate affects. Analysis of breaking ocean waves,¹⁹⁰ as well as laboratory controlled wave action^{40,56} has shown that the majority of sea spray aerosol (SSA) particles are less than 1 μm in diameter.¹⁹¹ Considering this size scale, nanotechnology and nanoscopic methods are necessary in the effort to understand properties of SSA. Atomic force microscopy (AFM) has proven to be an excellent method for studying systems at the nanoscale.⁶ Highly resolved force sensing capabilities and sub-nanometer 3D spatial resolution make AFM a powerful investigation tool for studying nanoparticles. Vacuum conditions, which may alter particles, are not required, and experiments can be performed under controlled RH.⁵⁷ While AFM is frequently used to study nanoparticle morphology¹⁷⁵ and size,¹⁹² the efforts of this study were to develop AFM based methodology to measure the surface tension of submicron sized liquid droplets at controlled RH. Optical tweezers has been used to indirectly estimate the surface tension of micrometer sized NaCl droplets but the value observed is lower than expected, assumedly due to adsorption of trace species from the gas phase.¹⁷³ AFM based surface tension measurements have been previously performed on bulk solutions,¹⁹³ thin liquid layers,¹⁹⁴ and micrometer sized oil droplets and bubbles in water.^{195,196} To the best of our knowledge, there are no studies that directly measure the surface tension of droplets

smaller than several microns in size and furthermore, no studies that investigate surface tension as a function of RH of small, atmospherically relevant droplets.

For simplicity in developing this methodology, we have chosen single component chemical model systems of atmospheric relevance. NaCl is a major constituent of SSA and was chosen as an inorganic model system.^{44,165} Besides inorganic salts, organic enrichment in SSA is an important aspect of aerosol chemistry^{197,198} and greatly influences surface tension, thus atmospherically relevant organic compounds were selected as well. Low molecular weight dicarboxylic acids such as glutaric acid (GA) and malonic acid (MA) are prevalent chemical species in atmospheric particles.^{199,200} Dicarboxylic acids are water-soluble, surface active molecules and have been shown to alter hygroscopic properties of aerosols, which causes surface tension depression and changes in actual and predicted CCN activity.^{166,167,168,201} Thus, organic model systems used in the method development are GA and MA.

7.3 Experimental

7.3.1 Sample preparation

Aerosols were generated with a constant output atomizer (TSI, Inc., model 3076) from 100 – 200 mM aqueous stock solutions. All chemicals used were reagent grade (99.99% purity, Aldrich) and dissolved in deionized water (18 M Ω ·cm). The aerosol was passed through a diffusion dryer (TSI, Inc., model 3062), then size selected and deposited by impaction with a micro-orifice uniform deposit impactor (MOUDI) (MSP, Inc., model 110) onto hydrophobically coated silicon wafers.¹⁰² The particles in this study were collected on stage 6 of the MOUDI, which has an aerodynamic size cutoff of 1 μ m at 50% collection efficiency and particle size range of 0.56-1.0 μ m. In most cases, the

substrate deposited particles were prepared and studied at the same day to avoid possible sample aging.¹⁶²

7.3.2 AFM based force spectroscopy

A molecular force probe 3D AFM (Asylum Research, Santa Barbara, CA) was used for all force spectroscopy and imaging. The silicon wafer containing particles was placed in a custom-made humidity cell,⁵⁷ attached to the AFM head. High aspect ratio, constant diameter Ag₂Ga nanoneedles (NN-HAR-FM60, NaugaNeedles) with nominal spring constant of 3.0 N/m were used for surface tension measurements and particle imaging. The AFM probe was first calibrated by determining the inverse optical linear sensitivity and spring constant with a thermal noise calibration method.²⁰² The sample was imaged in AC mode to locate individual particles, then the RH was slowly raised, and force-distance plots were collected at the center of the droplet. After each change in RH, and before taking AFM measurements, the cell was allowed to equilibrate for ca. 15 minutes. For GA, the relative humidity was raised quickly at the beginning of the experiment, and then slowly decreased while performing the force spectroscopy at different RH on the dehydration cycle. A tip velocity of 1 $\mu\text{m/s}$ was found to give the most stable force data and was used for all measurements. Approximately 20-30 force plots were collected at each RH on several individual droplets. The probe was either cleaned in deionized water between experiments or a new probe was used because crystals were observed (via electron microscopy) to solidify on the end of the needle after being subjected to the concentrated solutions, which effectively changes the diameter of the probe and therefore, the surface tension quantification.

7.3.3 Bulk surface tension measurements

Bulk surface tension measurements were performed with a Kibron AquaPi tensiometer. The tensiometer was calibrated with deionized water before each use and the dyne probe was clean with ethanol, water and flame between experiments. All chemicals (NaCl, GA and MA) used were dissolved in deionized water (18 MΩ·cm). Serial dilutions were performed to obtain surface tension as a function of a solute concentration.

7.4 Results and Discussion

7.4.1 AFM surface tension measurements

Utilizing the AFM as a tensiometer was first reported by McGuiggan et al. in 2006, using a quartz rod.²⁰³ The production and commercialization of constant diameter Ag₂Ga nanoneedles grown on AFM tips have made it possible to probe droplets as small as several hundred nanometers in size.²⁰⁴ The surface tension (σ) of individual submicron sized droplets is calculated by quantifying the retention force (F_{Ret}) between the nanoneedle and the liquid droplet, and by knowing the radius (r) of the probe (Equation 8.2), assuming that the liquid meniscus is parallel to cylindrical probe at maximum force.¹⁹³

$$F_{Ret} = \pi\sigma r \quad (\text{Eq. 8.2})$$

The retention force is the amount of force required to break the meniscus pinned at the end of the cylindrical probe from the liquid interface. A pictorial representation of an example force plot on a droplet is shown in Figure 8.1. The needle starts at a position above the droplet (A) and then approaches the droplet vertically, in the z-direction, until it comes in contact with the liquid, causing spontaneous formation of a meniscus to rise

on the cylinder, bending the probe downward, and resulting in a negative force (B). The horizontal portion of the force plot between B and C is a result of the needle moving through the liquid droplet and coming into contact with the substrate at point C. When a predefined maximum amount of force is reached, the tip retracts back away from the sample (D). At point E, the probe experiences a large attractive force due to the liquid meniscus holding the needle at the surface of the droplet. Once the meniscus is broken, the tip quickly retracts back to zero force and returns to an equilibrium distance above the sample. The retention force is defined as the absolute value of the difference in force when the tip jumps away from the droplet and back to zero force. The jump-away point occurs when the gradient of interaction forces becomes less or equal to the spring constant of the cantilever.

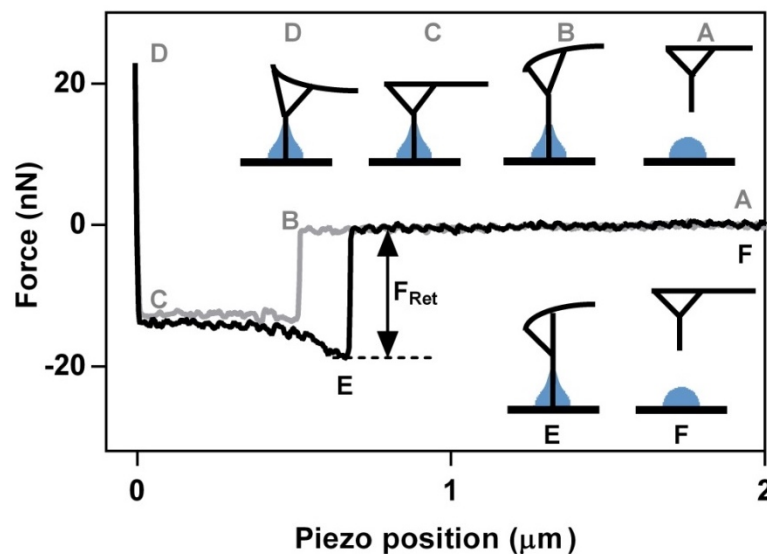


Figure 7.1: Typical AFM force plot measurement depicts the series of events that occur during approach (grey) and retract (black) cycle of the AFM cantilever on the submicron-sized droplet. The retention force (F_{Ret}) is used to quantify the surface tension.

At the start of the experiment, a silicon wafer containing substrate-deposited particles is placed in a humidity cell and the RH is slowly raised. The phase transition from a solid particle to a liquid droplet (deliquescence) and the reverse transition (efflorescence) depend on chemical composition. The deliquescence point of NaCl and GA is a relatively sharp transition at approximately 75%¹⁶⁷ and 83-85%¹⁸⁶ RH, respectively. MA is highly hygroscopic and steadily uptakes water from as low as 10% RH.¹⁸⁶ These hygroscopic properties dictated the range of RH that was probed for the surface tension experiments and are discussed in more detail below.

An initial important control study was performed to verify that bulk AFM surface tension measurements of pure water agree with bulk tensiometer results. For the AFM, a petri dish containing ~50 ml of DI water was placed on the AFM stage. Once the nanoneedle was in the vicinity of the water, force plots were collected, displaying profiles consistent with the needle contacting the liquid surface, resulting in large retention force (See SI for details). Based on 20-30 force measurements of the retention force and utilizing Equation 8.2, AFM based surface tension of water was determined to be 72.6 ± 0.5 mN/m, which agrees within standard deviation with the bulk tensiometer value of 73.2 ± 0.1 mN/m. Slight discrepancy between the two numbers is likely due to error associated with the value of the radius of the nanoneedle used in the AFM calculation, as this value is estimated from an SEM image. We note that such experiment can be used as a calibration step to determine the exact diameter of the needle or to investigate if the tip is damaged or contaminated.

7.4.2 NaCl AFM results

The first system studied was NaCl. Figure 8.2A shows 3D AFM images that demonstrate the phase transition of a solid NaCl particle at low RH (~10%) to a liquid droplet at 80% RH. The observed phase transition is also apparent in the morphological change from a cubic NaCl crystalline solid to a round liquid droplet, which is approximately two times larger than the solid particle. The force plot in Figure 8.2B is collected at the approximate center of a NaCl droplet. While NaCl deliquesces at ~75% RH,¹⁸⁸ the surface tension measurements were complicated by the fact that a solid core was still observed in the force profile until ~79% RH, which led to inconsistencies in the data. The presence of a solid core at RH above 75% has also been observed by others.²⁰⁵ At relatively high RH (above 88% in this case) the droplets become unstable under the mechanical force of the AFM cantilever during imaging. Consequently, imaging was performed initially under low RH to locate the particle and then minimally at higher RH to avoid damaging the droplet. Taking these issues into consideration, the range of RH probed for NaCl was between 78-88%.

At RH values above the deliquescence humidity of NaCl the deliquesced droplet continually takes up water, which effectively dilutes the salt concentration. Since surface tension is highly dependent on solute concentration,^{185,186} measurements of the retention force and determination of the surface tension using Equation 8.2 were performed as a function of RH. Figure 8.2C shows experimentally determined surface tension values collected on several representative submicrometer size droplets as a function of RH (bottom axis) and concentration (top axis). For all model systems, 2-3 droplets were probed and at least 20 force measurements were performed at each RH. A noticeable

change in the surface tension is observed (82-79 mN/m), even for a relatively small change in RH, due to dilution of the NaCl upon the uptake of water, hence decrease in the concentration of solute with increasing RH. In order to verify that the single droplet AFM method is accurate, we compared our results to bulk surface tension measurements at concentrations relevant to the RH range that was probed. Water activity data were utilized to determine solute concentration at a particular RH¹⁸⁵ (see SI for details) and the predicted relationship is represented in Figure 8.2C as the solid line. The close overlap between the AFM-based surface tension measurements on individual submicrometer droplets with the bulk values provides strong evidence that AFM based tensiometer measurements are accurate and reliable. Predicted data obtained using the Extended AIM Aerosol Thermodynamic Model (AIM model)²⁰⁶⁻²¹⁰ also display close overlap between bulk surface tension predictions and AFM measurements (see SI). The NaCl concentration range associated with the AFM surface tension measurements for the data shown in Figure 8.2C is approximately 3-5 M, indicating that the droplets are highly concentrated and nearing their saturation solubility point.

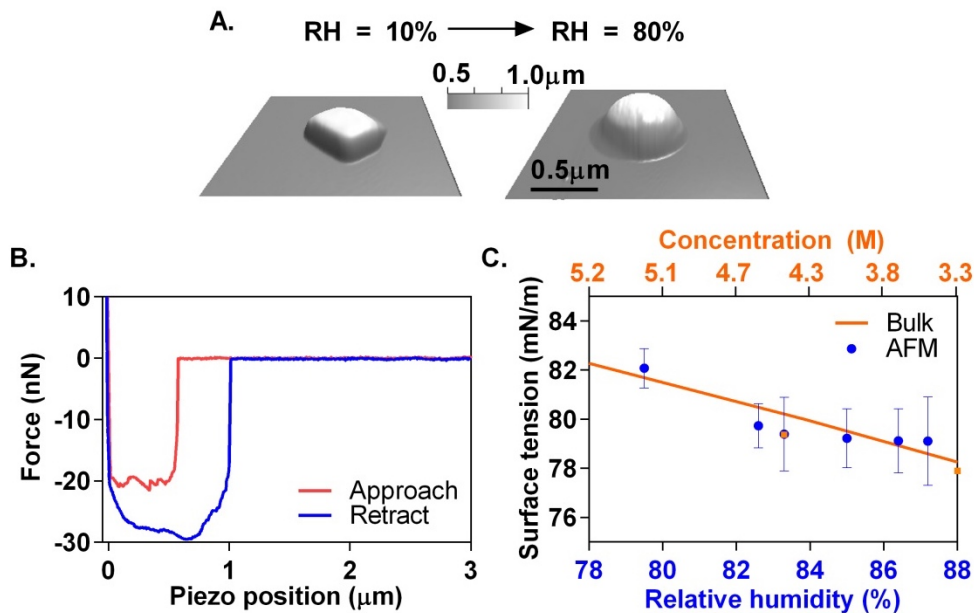


Figure 7.2: Experimental results of AFM based surface tension measurements of a ~500 nm NaCl droplet. A. 3D image of a solid NaCl crystal at 10% RH and deliquesced NaCl particle at 80% RH. B. Experimental force plot on a NaCl droplet. The approach data is in grey and the retract data is in black. C. Surface tension measurements (average and standard deviation) as a function of RH (bottom axis) and solute concentration (top axis). Predicted data is obtained from bulk solution surface tension measurements and is shown as the solid line.

7.4.3 GA and MA AFM Results

Having validated AFM-based surface tension measurements on NaCl salt, we extended our measurements to model organic systems, GA and MA, using a similar approach. Figure 8.3A shows a typical GA particle at 10% RH and corresponding deliquesced droplet at 90% RH. Hence, as a result of water uptake, round amorphous GA particle with diameter of 0.7 μm and height of 0.25 μm (10% RH) became a liquid droplet with diameter of 0.9 μm and height of 0.4 μm (90% RH). The morphology of MA particles and submicrometer droplets are similar to that of GA (images are not shown). Experimental force plots collected on GA and MA droplets are shown in Figures 8.3B and 8.3D, respectively. Both GA and MA droplets were similar in height (~ 400 nm) at approximately 85% and 70% RH, respectively.

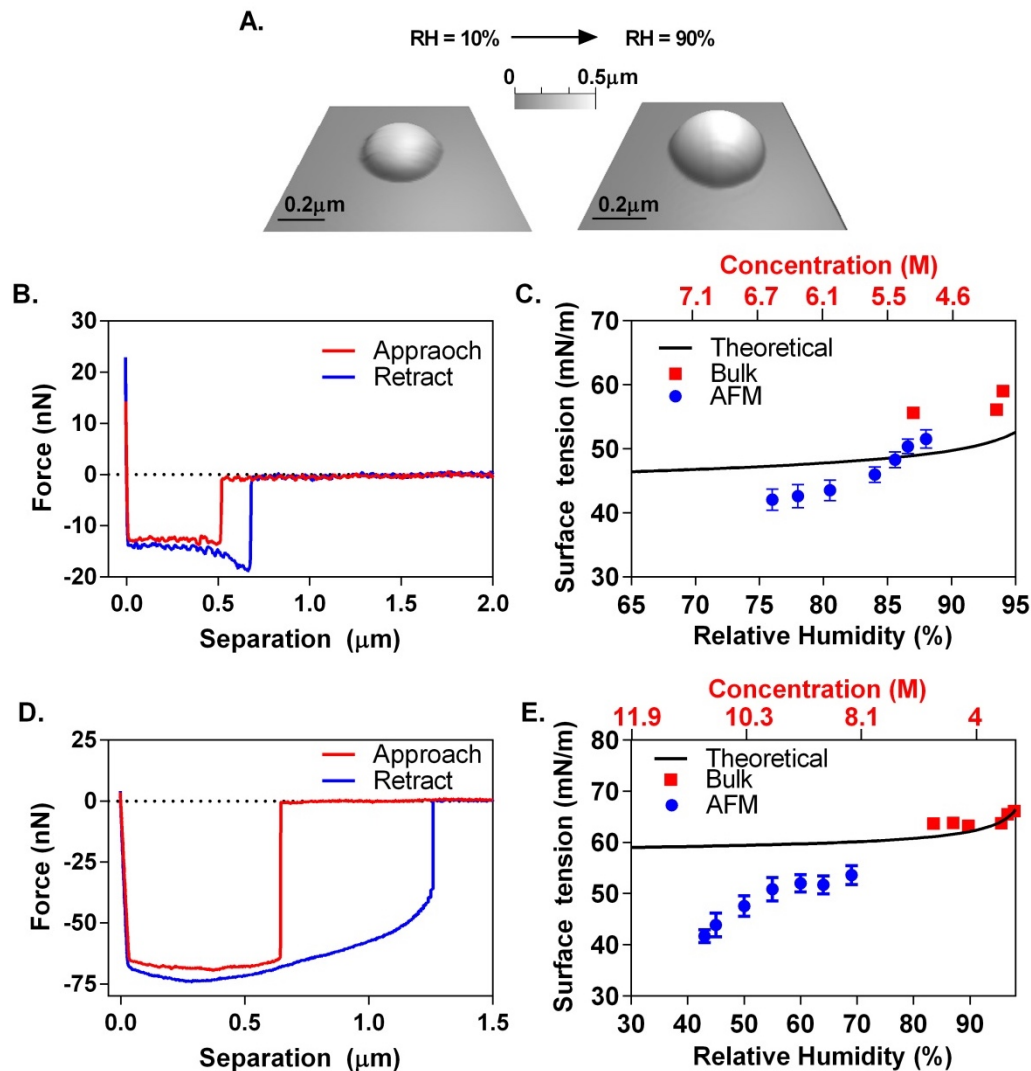


Figure 7.3: Experimental results of AFM based surface tension measurements of GA and MA. A. 3D images of a solid GA particle at 10% RH and deliquesced GA particle at 90% RH. B,D Experimental force plots on GA (B) and MA (D) droplets. The approach data is in grey and the retract data is in black. C,E. AFM based surface tension measurements (average and standard deviation) as a function of RH (bottom axis) and solute concentration (top axis) of GA (C) and MA (F). Predicted data (solid lines) are obtained from bulk solution surface tension measurements.

The RH range differed for each chemical system due to different hygroscopic properties. GA was probed in the range of approximately 75-90% RH, while MA was measured over the range of approximately 40-70% RH. Since GA does not absorb a significant amount of water until above 83%,¹⁸⁹ the RH was first raised to 90% in order to deliquesce the particles and force measurements were taken during the dehydration

cycle so that a larger range of RH could be probed.²¹¹ MA was measured on the hydration cycle since it steadily takes up water from relatively low RH.^{189,211} AFM surface tension measurements at different RH values for GA and MA are reported in Figures 8.3C and 8.3E, respectively. The predicted surface tension dependence as a function of RH and concentration (solid lines in Figures 8.3C,E) was obtained using bulk solution surface tension measurements as a function of solute concentration. However, since concentrations of the droplets measured with AFM were much higher than what is accessible by bulk measurements (due to solubility limits) the surface tension was extrapolated using a predictive model^{33,36} for highly concentrated solutions (details in SI).³⁵ The water activity of GA and MA were obtained using the online modeling programs Aerosol Inorganic Mixtures Functional groups Activity Coefficient (AIOMFAC model)^{189,212,213} and the AIM model to establish the concentration of the droplets as a function of RH.²⁰⁶⁻²¹⁰ The results of the AFM based surface tension for both GA and MA submicrometer droplets agree reasonably well both in terms of absolute values and with the predicted trend of surface tension as a function of RH due to changes in concentration upon uptake or release of water. We note, however, that both GA and MA show noticeable deviation from the bulk solution prediction at lower RH, which corresponds to higher solute concentrations. The origin of the deviation is likely due to non-ideal behavior of solutions at such high concentrations, which likely results in incorrect predictions obtained from the bulk solution data.

7.5 Conclusions

This study provides a quantitative way to measure the surface tension of submicron size atmospherically relevant droplets under ambient pressure. Previously, there had been no reported methods that could directly probe the surface tension of submicron size droplets and furthermore, as a function of changing RH. The implications of this method, as well as subsequent future surface tension studies, are that the understanding of the role of atmospheric aerosols in cloud formation could be significantly improved and thus should advance the field of atmospheric chemistry and atmospheric science, as well as improve predictive power through more accurate models and theories that utilize surface tension. Now that the method has been shown to work on both organic and inorganic model systems, measurements can be performed on more complex multi-component systems, as well as authentic SSA and any water-soluble substrate deposited particles in the size range from ~300 nm up to few micrometers. Nanoscale phenomena such as surface partitioning and size-effects can be addressed by directly probing surface tension and not just modeling it; as models typically assume ideal behavior which is often not the case for these highly concentrated solutions that are typical of atmospheric aerosol.

8. SIZE-DEPENDENT SURFACE TENSION DEPRESSION OF INDIVIDUAL SUBMICROMETER SEA SPRAY AEROSOL CORRELATES WITH ORGANIC ENRICHMENT DURING A PHYTOPLANKTON BLOOM

8.1 Abstract

Surface tension of aerosol particles in the atmosphere dictates their cloud forming properties but direct measurements of surface tension for submicron sized particles of atmospheric relevance have been difficult to measure. In this study, atomic force microscopy (AFM) is utilized to measure the surface tension of substrate deposited, individual submicron sized sea spray aerosol (SSA) particles. The data indicate that SSA contains a significant amount of organic species, which significantly decreases the surface tension of particles from that of a pure sea salt and that the largest depression in surface tension correlates with phytoplankton activity in the sea water. In particular, surface tension measurements are shown to correlate with organic volume fraction analysis and there is a size dependent organic volume fraction and enhanced surface tension depression associated with a phytoplankton bloom. Through direct measurements of surface tension for a range of submicron sized, chemically complex liquid droplets collected from a realistic ocean environment reveals that absolute values are as much as 30 to 40% lower than the surface tension of pure NaCl and water, respectively. This indicates there may be large discrepancies in predictive climate models that utilize simplistic assumptions of particle composition and surface tension values.

8.2 Introduction

The ocean is a major source of atmospheric aerosols, releasing a chemically complex mixture of particles that are composed of salts, organic species and biological

components. However, this complexity is often lacking in atmospheric chemistry and climate models. One of the most widely used models for predicting the supersaturation relative humidity (RH) required for cloud droplet activation is Kohler theory (Eq. 8.1)¹¹⁶. In Eq. 8.1, the natural log of the supersaturation relative humidity, S , is shown to be influenced by two terms. The Kelvin term, shown as the first term on the right-hand side of Eq. 8.1, is dependent on the surface tension (σ) of the droplet at activation and dry particle size (D) (M_w is the molecular weight of water, ρ_w is the density of water, R is the universal gas constant, and T is temperature). The second term on the right-hand side of the equation 8.1 is a Raoult's term, takes into account dissolved solutes, where n_s is the moles of solute.

$$\ln(S) = \frac{4M_w\sigma}{RT\rho_w D} - \frac{6n_s M_w}{\pi\rho_w D^3} \quad (\text{Eq. 8.1})$$

Typically, the properties of particles emitted from the ocean are assumed to be pure sodium chloride (NaCl) or a mixture of inorganic salts.²¹⁴ In addition, at supersaturation RH, the droplets are assumed to be very dilute.²¹⁴ However, it has been well established that sea spray aerosol (SSA) contain significant amounts of organic species, especially in the submicron size range,⁴⁸ which is the size range that is important for cloud condensation nuclei. Assuming aerosol particles have surface tension of water or pure salt solutions and ignoring any surface tension depression due to the presence of organic species can severely affect the predictive accuracy of models like Kohler theory. For example, upon observing a 30% decrease in surface tension of fog aerosol extract relative to that of water, Facchini et al. demonstrated that this can translate to as much as -1 Wm^{-2} error when predicting radiative forcing contributions from cloud albedo, globally.³⁴ Furthermore, assuming that the surface tension of aerosols can be predicted from bulk

solution measurements may be inaccurate. After measuring surface tension values of marine particle extracts as low as 30-40 mN/m, Gérard et al. emphasized that the Szyszkowski equation does not accurately represent the relationship between surface tension and organic concentration based on their aerosol measurements.²¹⁵ The implications of this is that SSA particles maintain low surface tension up until the point of activation, which makes the particles more susceptible to cloud activation. To improve the accuracy of these models, surface tension of atmospheric particles must be better understood over a wide range of particle composition, size, and atmospheric conditions such as RH, temperature, and anthropogenic influences. While several attempts have been made to account for the presence of surface active organic molecules in predicting CCN activity,^{35,166,216} experimental measurements are lacking on actual submicron sized liquid droplets. .

Measurements on particles in the submicron size range have remained inaccessible for direct single-particle measurements for several reasons including the inability of conventional techniques to probe such small liquid volumes. Here we report the first surface tension measurements performed on individual, chemically complex, submicron size nascent SSA particles deposited onto hydrophobic substrates. Furthermore, single-particle measurements are a vital tool for better understanding the properties of atmospheric aerosols because the unique response from individual complex particles is lost in an ensemble average of thousands of particles that returns one “representative” value. Here we have measured surface tension of SSA particles generated in a unique ocean-atmosphere facility. The amount of organic species was estimated on a single particle basis and is shown to be directly related to surface tension

as well as particle size. Large particle-to-particle diversity was observed for SSA surface tension values which correlated with large differences in particle composition as determined by a suite of chemical characterization techniques in effort to gain single particle chemical information linking composition to surface tension.

8.3 Experimental

The SSA collected in this study were generated from a waveflume containing a phytoplankton bloom and the details of the experiment are reported elsewhere.¹⁵² Surface tension measurements were performed with constant diameter needle tips (NaugaNeedles) on particles that were 0.5 – 1.0 μm in size (dry diameter). Force-distance cycles were found to be reproducible at different retraction velocities and were collected at 1 $\mu\text{m/s}$. Particles were deposited with the MOUDI onto hydrophobically coated Si substrates.

8.4 Results and Discussion

8.4.1 SSA generation

SSA studied here were collected from a sealed wave simulation channel containing a laboratory grown phytoplankton bloom to generate and collect SSA in a manner similar to natural wave action, and therefore, aerosol production in the ocean. Phytoplankton blooms are a common occurrence in the ocean and studies have shown that aerosols generated during a bloom can have altered composition and chemical properties (from that of pure salt) due to increased organic content and therefore, the surface tension of the particles can vary drastically. The progression of the phytoplankton bloom was monitored by measuring the chlorophyll-a (chl-a)

concentration over the course of the campaign (Figure 8.1, green data). Chl-a is a commonly used tracer for biological activity in the ocean and high concentrations have been shown to be associated with SSA that is enriched in organics^{45,217}. As seen in Figure 8.1, during the IMPACTS experiment, chl-a concentration peaked on the 17th of July, followed by a decrease the next 4 days, and then increased again on July 25-28th. Based on the trend in chl-a concentration, samples generated on four important campaign dates were analyzed; July 13th (low chl-a concentration), July 17th (chl-a peak), July 21st (chl-a concentration decreased), and July 26th (2nd peak in chl-a concentration).

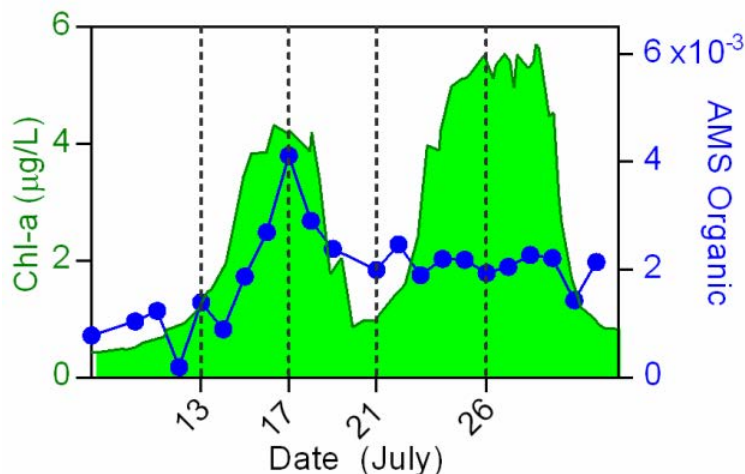


Figure 8.1: Temporal progression of the phytoplankton bloom. Chlorophyll-a concentration is in green and AMS 43m/z data is in blue. Dashed lines correspond to the selected dates of SSA collection that were analyzed in the present work. Chl-a concentration measured was measured by Jon Trueblood (Grassian Group, University of Iowa) and Camille Sultana (Prather Group, University of California, San Diego). AMS Data was collected by Xiaofei Wang (Prather Group, University of California, San Diego).¹⁵²

An online aerosol mass spectrometer (AMS) analyzed SSA particles generated by the waveflume in real time.¹⁵² The organic content of the aerosol was estimated for particulate matter less than 1 μm in size (PM_{1}) by monitoring mass to charge ratios associated with organic species. This data are shown temporally, overlaid with the chl-a

concentration in Figure 8.1. An increase in AMS organic content in the particles occurs during the first peak in chl-a concentration (July 17th), indicative of organically enriched SSA due to biological activity. Interestingly, there is no organic enrichment in the SSA, according to the AMS data, corresponding to the second peak in chl-a concentration (26th-28th).

8.4.2 Particle morphology and organic volume fraction

Submicron sized SSA particles were imaged with AFM. Particle morphology on the four days chosen for analysis was very similar and a representative particle is shown in the 3D AFM image in Figure 8.2A. The vast majority of particles have core-shell morphology (~98% of all particles studied (approximately 600 total)), consisting of a phase separated cubic-shaped core, surrounded by a coating. SSA with similar morphology has been reported previously in atmospheric particles as well as synthetic particles composed of model systems^{175,52}. AFM phase imaging shows a more detailed view of the core-shell particle morphology (Figure 8.2B). The difference in phase between the coating and the cubic shaped core of the SSA particles is strong evidence that the two regions of the particles are chemically different because they interact differently with the AFM cantilever, causing different degrees of phase shift.

STXM and NEXAFS were used to elucidate spatially resolved single particle chemical information. Figure 8.2C shows a spatially resolved singular value decomposition map obtained from using the Carbon pre-edge absorbance of 278 eV and comparing with the carbon post edge absorbance at 320 eV. With this analysis it is possible to estimate regions of higher carbon absorbance (green) and regions that do not absorb show significant difference in the absorbance between 320 and 280 eV, which is

classified as inorganic. The representative spectra that were used to define regions of organic species is shown in Figure 8.2D. The spectrum shows absorbance for carboxylic acid (288.6 eV), carbonate (290.5 eV) and potassium (297 and 299 eV).^{145,218} STXM/NEXAFS mapping suggests that the coating of the particles is organic in nature but cannot give specific chemical composition data on the core of the particles. SEM/EDX data reported in Figure 8.2E (collected by Olga Laskina at Pacific Northwest National Laboratory (Grassian Group, University of Iowa) elucidates that the core of the particles is NaCl. By pairing these complementary microscopy techniques a complete understanding of these particles is realized, which is a NaCl core surrounded by organic coating.

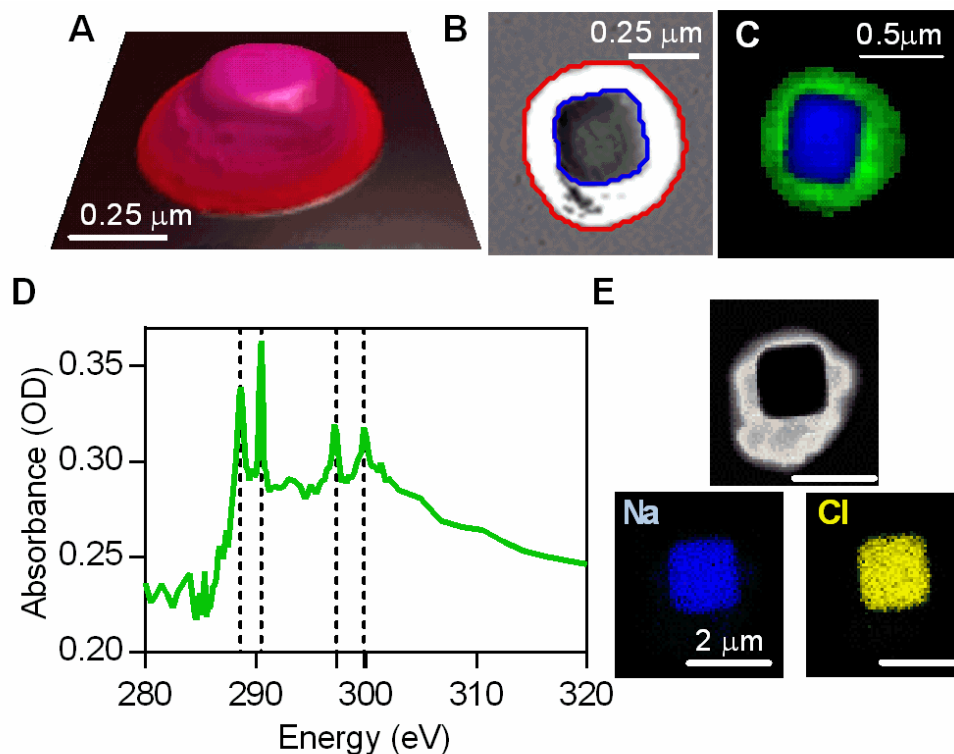


Figure 8.2: **A.** Representative 3D AFM image a SSA particle. **B.** AFM phase image of a SSA particle. The red outline gives an example of the mask used to obtain the volume of the whole particle and the blue outline gives the volume of the core. **C.** STXM/NEXAFS image of a singular value decomposition map obtained from using the carbon pre-edge absorbance at 278 eV and comparing with the carbon post-edge absorbance at 320 eV. Green maps primarily organic species. **D.** Representative NEXAFS spectrum of the carbon K edge (278-320eV) used to identify regions of organics. The spectrum shows absorbance for carboxylic acid (288.6 eV), carbonate (290.5 eV) and potassium (297 and 299 eV). **E.** The top image is the backscattered electron image of a representative particle. The bottom left is the EDX map of Na and the bottom left image is the EDX map of Cl. SEM/EDX data was collected by Olga Laskina at Pacific Northwest National Laboratory (Grassian Group, University of Iowa). STXM/NEXAFS data was collected by Don Pham (Moffet Group, University of the Pacific).

AFM phase imaging was used to quantify, by volume, the organic content of particles based on their core-shell morphology. A mask was used to define the whole particle area (Figure 8.2B red outline) and inorganic core area (Figure 8.2B blue outline), corresponding to the phase image. Organic volume fraction was then calculated by finding the difference of the whole particle volume and volume of the core and normalizing to the whole particle volume. The amount of organic coating changed as a

function of biological activity in the water and a representative amplitude and phase image from each date is shown in Figure 8.3A. Approximately 50 particles were analyzed for each sample and organic volume fraction quantification is plotted temporally in Figure 8.3B and overlaid with the AMS data. Both AFM and AMS show higher organic content in the aerosol on July 17th which coincides with high chl-a concentration. Previous studies have shown that high biological activity in the ocean during a phytoplankton bloom results in SSA that has higher organic enrichment in the SSA.^{48,198} Interestingly, the organic volume fraction in the aerosol does not increase during the second phytoplankton bloom. Wang et al. found that the aerosol organic composition differed between the two phytoplankton blooms, which may account for the difference in amount of organic coating at times of increased biological activity. Aliphatic rich organics were shown to dominate the aerosol during the first phytoplankton bloom, while more oxygenated organics dominated during the second phytoplankton bloom¹⁵². Aliphatic rich organic species are more likely to reside at the air-water interface because they are relatively less soluble than oxygenated organics and become enriched in the emitted aerosol upon bubble formation and bursting during wave action.

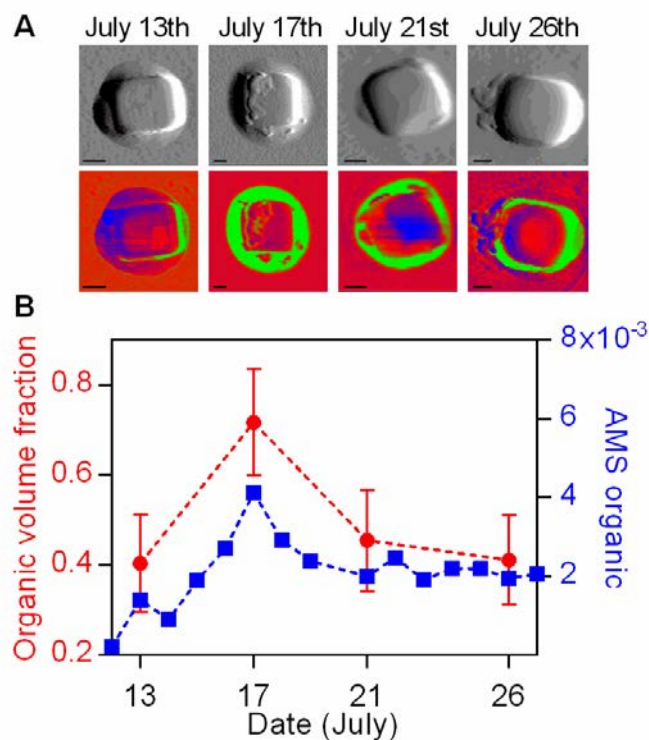


Figure 8.3: **A.** Organic volume fraction is plotted as a function of size. Solid line represents fit to a line (slope is $-0.25 \mu\text{m}^{-1}$) for illustrative purpose. The particles that fall in the size range for stage 6 and 7 are labeled. **B.** Line plots of surface tension distribution for particles on stage 6 (red) and stage 7 (blue). The inset shows individual particle measurements for each stage. AMS Data was collected by Xiaofei Wang (Prather Group, University of California, San Diego).¹⁵²

8.4.3 AFM surface tension measurements

The ability to measure the surface tension of a liquids using AFM has been established in the past decade.^{9,193,204} In previous work we further established the methodology of using AFM to measure the surface tension of submicron size droplets as a function of relative humidity (RH).⁹ The quantification of interaction force between the AFM probe and a droplet allow surface tension to be calculated via Equation 8.2, where F_{Ret} is the retention force, σ is surface tension, and r is the radius of the AFM probe.¹⁹³ It is crucial that the radius of the AFM probe be known in order to accurately quantify surface tension. Therefore, a constant (and known) diameter nanoneedle (NauGANeedles) was used for all AFM surface tension measurements.

$$F_{Ret} = 2\pi\sigma r \quad (\text{Eq. 8.2})$$

Surface tension measurements of submicron sized SSA droplets were performed on 40-50 different individual deliquesced particles at 80 ($\pm 1\%$) RH for each of the four days analyzed. A representative image of particles at low RH and corresponding liquid droplets at 80% RH is shown in Figure 8.4A. The results of AFM surface tension measurements of particles in the size range of 0.56 - 1.0 μm are reported in Figure 8.4B-C. A representative force plot taken on a liquid droplet is shown in Figure 8.5B, as well as pictorial representation of the events of the force cycle and the retention force used to quantify surface tension is labeled. Figure 8.4C shows line plots of the distribution of surface tension values from each day analyzed and the inset in Figure 8.5C shows single particle measurements (each data point represents the surface tension of one droplet). The range of surface tension values on each day is broad (± 10 mN/m), which reflects the fact that the particles, result in aerosol that is chemically complex and gives rise to particle to particle variation in terms of chemical composition and concentrations – properties that severely dictate the surface tension of liquids. Inorganic salts, like NaCl cause negative surface excess resulting in an increase in surface tension relative to water. Organic species in sea water are often times amphiphilic and prefer to reside at the air-water interface resulting in positive surface excess and decrease surface tension of water. The average and standard deviation of measured surface tension values are reported in Table 8.1. The large observed range of observed values demonstrates the necessity of single particle measurements. Especially considering the average value on most dates analyzed is approximately 68-71 mN/m – a result that, on its own, would suggest that the

particles have surface tension values close to pure water, when in reality these values are a result of complex mixtures of both organic and inorganic species.

Table 8.1: Average and standard deviation surface tension values of particles 0.56 – 1.0 μm in size.

Date	Surface tension (mN/m)
July 13	71 ± 9
July 17	58 ± 9
July 21	69 ± 9
July 26	68 ± 10

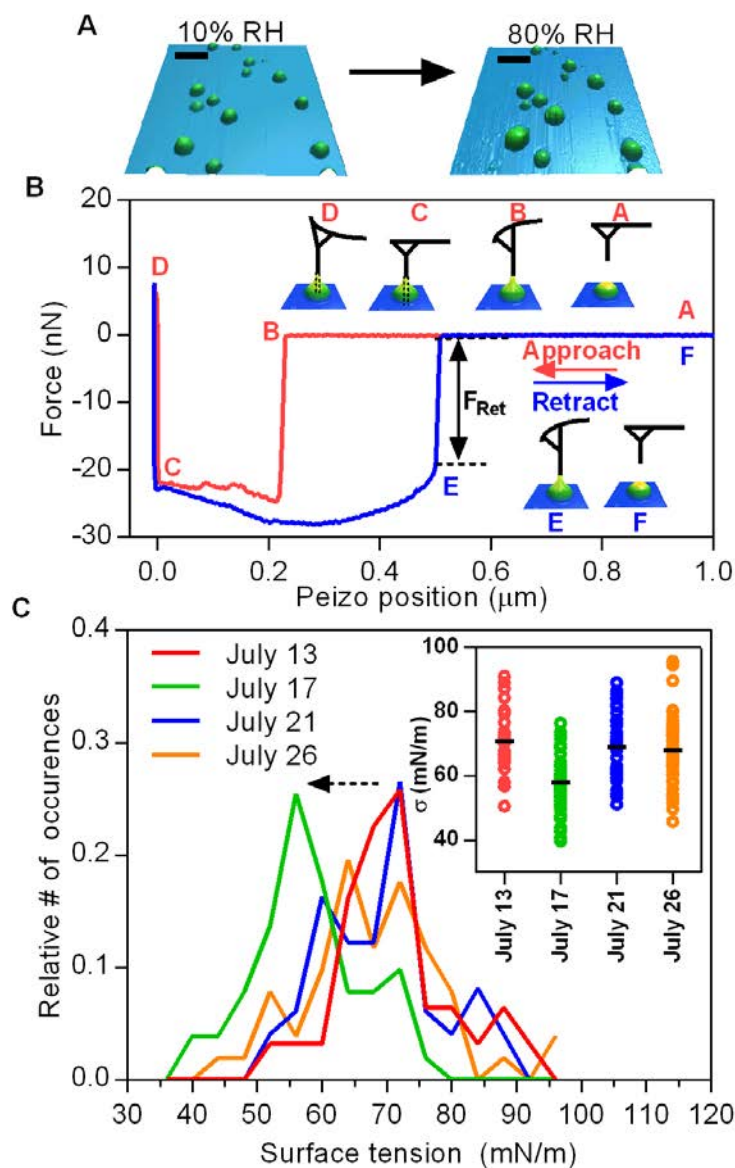


Figure 8.4: **A.** Representative 3D AFM images of solid particles at low RH (left) and corresponding liquid droplets at 80% RH (right). **B.** Experimental force plot taken on 250nm size SSA droplet (July 13). The retention force used for quantifying surface tension is labeled. **C.** Line plot of surface tension distributions. The inset shows surface tension values of individual SSA droplets and the black line represents the average value.

The average surface tension on all days analyzed, as well as the vast majority of the single particle measurements are lower than the expected surface tension of NaCl (80 ± 2 mN/m) at 80%RH, a finding that coincides with the fact that virtually all particles have some amount of organics associated with them (observed in AFM phase images).

Noticeably, the average surface tension value on July 17th (58 ± 9 mN/m) is much lower than the surface tension of particles on the other days analyzed and is about 20% lower than the surface tension of water. This observation is a consequence of higher organic content in the aerosol, as observed in the AMS data and the AFM organic volume fraction analysis. An increase in organics in the aerosol during the peak of a phytoplankton bloom and high chl-a has been reported in several other studies based on bulk solution measurements of aerosol extracts but has never been directly measured on a single particle basis.⁴⁸ These measurements show direct correlation between higher organic content of the aerosol and depressed surface tension of the resulting liquid droplets during high biological activity in the ocean water. However, there is not increased surface tension depression corresponding to the second phytoplankton bloom because oxygenated species, which dominate during the later bloom, have a less severe effect than aliphatic-rich molecules that dominate during the first bloom. The specific mechanisms of biological activity that lead to changes in the water and aerosol composition is discussed in detail elsewhere.¹⁵² Consequently, the vast majority of absolute surface tension values are significantly lower than what are often times assumed for droplets in the atmosphere and used in climate models.

8.4.4 Particle size dependence

It has been observed that the organic content of SSA can vary with particle size.^{43,44,198} O'Dowd et al. showed that SSA collected in the North Atlantic during a plankton bloom in the size range of 1 – 0.5 μ m was approximately 50% organic, by mass, but particles smaller than 500nm were approximately 90% organic, by mass.⁴⁸ A broad size range of SSA particles collected during IMPACTS was analyzed for the July 17th

collection date in order to investigate the size dependence of organic volume fraction. This analysis, organic volume fraction plotted as a function of dry particle size, is shown in Figure 8.5A. This data reveals that there is, in fact, relatively higher organic content for smaller particle size collected during increased biological activity.

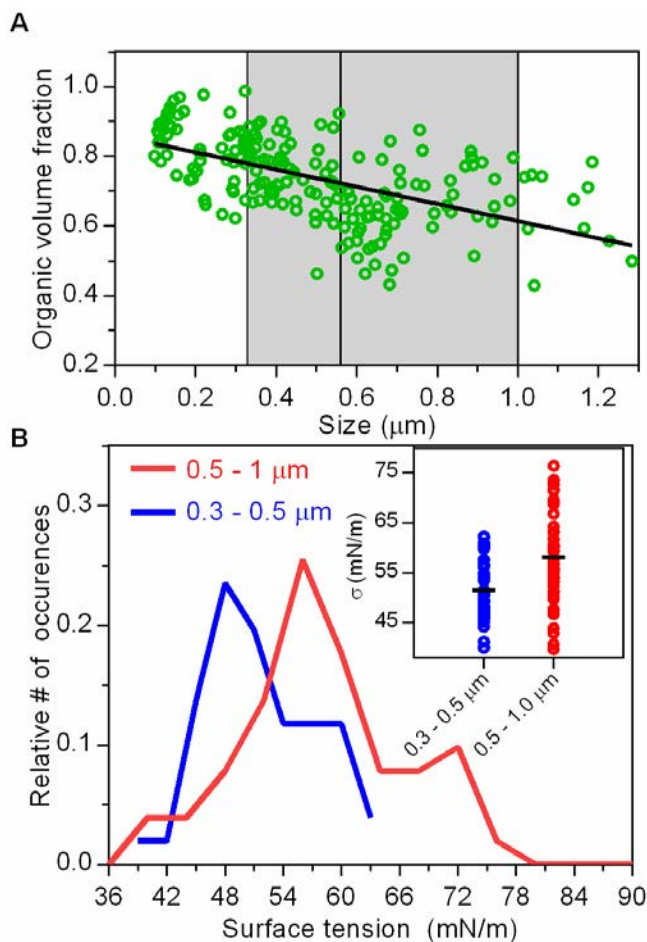


Figure 8.5: **A.** Organic volume fraction is plotted as a function of size. Solid line represents fit to a line (slope is $-0.25 \mu\text{m}^{-1}$) for illustrative purpose. The particles that fall in the size range for stage 6 and 7 are labeled. **B.** Line plots of surface tension distribution for particles on stage 6 (red) and stage 7 (blue). The inset shows individual particle measurements for each stage.

Furthermore, the surface tension of two different particle size ranges, (size range $1.0 - 0.5\mu\text{m}$ and $0.36 - 0.5 \mu\text{m}$) were compared and reported in Figure 8.5B. The average organic volume fraction for larger particles is 0.7 ± 0.1 and 0.8 ± 0.08 for the smaller size

range. Surface tension data for approximately 50 particles was collected for each size. Interestingly, the average surface tension of smaller particles is even lower than the surface tension on of particles in the larger size range (Figure 8.5B). As seen in the line distributions in Figure 8.5B there is a noticeable shift to lower surface tension values for smaller particles. The average and standard deviation of surface tension is 58 ± 9 mN/m and 51 ± 6 mN/m, for particles in the size range $1.0 - 0.5\mu\text{m}$ and $0.36 - 0.5 \mu\text{m}$, respectively. This size analysis reveals that the surface depression is more severe for smaller particles and introduces another aspect of complexity for naturalistic SSA. Thus, the surface tension of particles changes as a function of size because of increased organic species and possibly different organic species all together. Thus, size dependent composition and surface tension should be realized when predicting cloud droplet activation.

8.5 Conclusions

For the first time, surface tension of individual submicron size chemically complex aerosol particles was measured with AFM. The plot in Figure 8.7 shows temporal changes in surface tension overlaid with changes of organic volume fraction. There is an undeniable correlation between increased organic content of the aerosol and surface tension. The complexity of naturalistic submicron size aerosol is realized by the fact that there is large particle-to-particle variation, changes with biological activity, and particle size dependence. While these relationships have been suspected to be present in the past, we demonstrate here novel single particle surface tension data as evidence of this phenomenon.

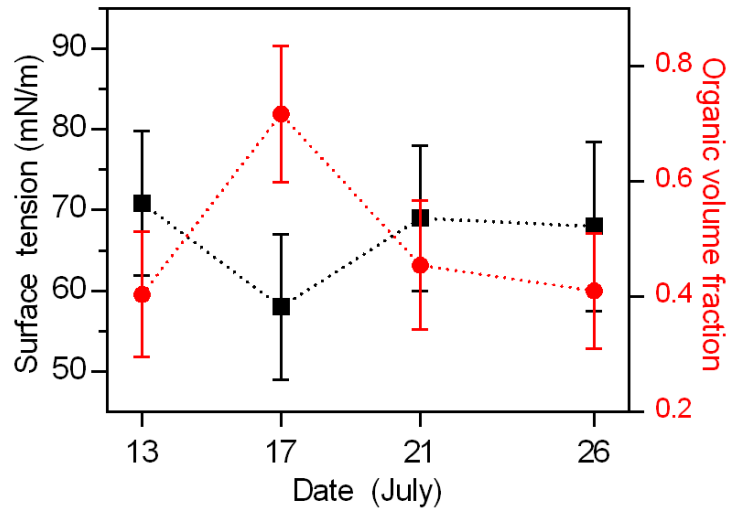


Figure 8.6: Surface tension measurements plotted with organic volume fraction. Data points represent the mean and error bars represent standard deviation.

9. PROBING SINGLE MOLECULE ENZYME-DRUG INTERACTION WITH MOLECULAR RECOGNITION FORCE SPECTROSCOPY

9.1 Abstract

Investigating single-biomolecule interactions requires great precision and control over the experimental environment and is important to elucidate molecule-to-molecule properties that can be convoluted or hidden in bulk measurement responses. The high spatial and force resolution provided by Atomic Force Microscopy (AFM), as well as the ability to perform experiments in liquid, have been utilized in this study to quantify single-molecule biological forces associated with the enzyme *escherichia coli dihydrofolate reductase* (DHFR) binding its inhibitor, methotrexate (MTX). Immobilization techniques of DHFR to the substrate and MTX to the AFM probe that utilize linking molecules greatly improve the accuracy and precision of the measurement. We have compared a well established linker, poly-ethylene glycol (PEG) to a novel linking procedure involving double-strand DNA (dsDNA). This work presents dsDNA as a viable, linker in MRFS experiments. Distribution of forces measure with dsDNA linkers has the same precision of PEG but is structurally rigid.

9.2 Introduction

Enzymes are one of the main regulators in a living organism as they can selectively catalyze a large number of chemical reactions necessary for life.²¹⁹ The selective inhibition of critical enzymes from infectious organisms and in altered disease states is an attractive means of drug development for many diseases.²²⁰ Rational drug design is strongly facilitated by the knowledge of enzyme-drug interactions that are typically studied indirectly from kinetic measurements.²²⁰⁻²²³ However, methods allowing

direct drug-enzyme interaction monitoring have become an important tool in modern drug discovery and studies of enzymes.²²¹ Traditional bulk biophysical techniques suffer drawbacks, as they only report on an average effect. In contrast, with single-molecule experiments, distributions in molecular properties are directly measured, thus offering fundamental insights into the molecular dynamics of enzymes.^{222,223}

Single-molecule force spectroscopy can quantitatively determine the interaction strength of ligands and their receptors.^{224–226} Molecular recognition force spectroscopy (MRFS) is a specific application of Atomic Force Microscopy (AFM) that measures the strength of bio-molecular interactions, such as that between an enzyme and its inhibitor, by covalently binding them to the surface and AFM tip, respectively.^{225,227–229} The ligand-receptor interaction is directly probed by pulling the tip away from the formed ligand-receptor complex until the applied force overcomes the binding interaction, leading to dissociation of the complex. Polyethylene glycol (PEG) is a common flexible linker used to tether the ligand to the AFM tip and biomolecules to the surface, while ensuring its separation and retaining its functionality.^{230–232} However, the use of flexible linkers can be disadvantageous in studies of enzyme folding, dynamics, or ligand dissociation as the response can become convoluted by the unfolding of the linker itself.^{233,234} In particular, the polydispersity and nonlinear elasticity of the linker can affect the dissociation rates and magnitudes of unbinding interactions,²³⁵ and the structural flexibility of the linker obscures the specific orientation of the protein necessary for the correct ligand-active site orientation needed for MRFS experiments. Two options that can potentially alleviate this problem are compared in this work: (i) binding the protein directly to the surface as a

homogeneous monolayer, with all active sites facing away from the surface, or (ii) using a rigid spacer for single-molecule measurements.

Our previous work demonstrated the viability of formation of a self-assembled enzymatic monolayer directly bound to a gold surface without the use of spacers and quantified the dissociation forces involved in the rupture of a drug directly-bound to the AFM tip from the immobilized enzyme.⁵⁵ While the approach is appealing in terms of relative simplicity, the main disadvantage was a contribution of non-specific interactions towards measured dissociation force.

Here, we present a new single molecule approach for the investigation of a drug - enzyme interaction. We report the use of double stranded DNA (dsDNA) as a rigid linker to immobilize an enzyme on a solid support, while retaining its catalytic activity.²³⁶ Furthermore, we demonstrate that dsDNA is a viable linker for MRFS measurements, providing just as much accuracy as PEG linkers.

9.3 Experimental

9.3.1 Materials

All reagents were purchased from Sigma-Aldrich, unless otherwise noted. *E. coli* DHFR was expressed, purified, and stored as discussed elsewhere.^{237,238} Amine and thiol functional 140 base pair dsDNA linker preparation was described by Singh, et al.²³⁶ Substrate functionalization procedures were described by Ditzler et al.⁵⁵ for DHFR monolayer on gold, and by Singh et al.²³⁶ for DHFR with dsDNA spacer on mica. The latter is described in more details below.

9.3.2 AFM imaging and force spectroscopy

An Asylum Research molecular force probe (MFP-3D) AFM (Santa Barbara, CA) was used for all imaging and subsequent force spectroscopy experiments. Bruker (SNL-10) silicon nitride AFM probes with a nominal spring constant of 0.06 N/m were used for functionalization procedures, force spectroscopy, and imaging in AC mode. All experiments were performed in MTEN buffer (50 mM MES, 25 mM Tris, 25 mM ethanolamine, and 100 mM sodium chloride pH 7.4) using a fluid cell at room temperature in order to reduce non-specific forces associated with capillary adhesion and to stabilize DHFR for the duration of the data collection. The spring constant and optical linear sensitivity were calibrated at the beginning of each experiment.²⁰² AFM probes were always newly functionalized before each experiment and used only once within 1 hour of finishing the functionalization procedure. Each experimental scenario was subject to at least two independent preparations and set of measurements – typically with two different functionalized tips and two different surfaces per each linking scenario. Distributions of rupture forces obtained using different tips and/or substrates were analyzed with Gaussian fits and independent data sets for each scenario were statistically the same.

For all data reported in the main text, a tip velocity of 1 $\mu\text{m/s}$ was used with maximum loading force of 500 pN. An optimal dwell time was found for each immobilization scenario that displayed sufficient binding probability (10-40%) with the majority of the force profiles indicative of single rupture events. The experiment with directly bound methotrexate (MTX) does not allow a method of separating non-specific forces; hence all force plots that showed a rupture event were analyzed. For experiments

utilizing a linker on the AFM probe, the force plots used for quantification were sorted based on the tip-sample separation distance at which the rupture event occurred as described in the text. The number of force plots comprising the force distributions in Figure 9.2 is reported in Table 9.1.

Table 9.1: The number of individual force measurements for the distributions reported in the main text.

Linking Scenario	Number of data points
A	5000
B	1400
C	250
D	235
E	170

9.3.3 Directly bound MTX - AFM probe functionalization procedure

The directly bound MTX functionalization procedure was described by Ditzler, et al.⁴ In short, ethanolamine in dry dimethyl sulfoxide (DMSO), 35% (v/v), was heated to 70 °C, cooled, and then molecular sieve beads were added. The tip was incubated in this solution overnight then washed for 5 minutes in DMSO and 5 minutes in ethanol, leaving an amine terminated probe.⁶⁻⁸ Approximately 10 ml 0.5 mM MTX in dry DMSO was mixed with 10 ml 5 mM 1-ethyl-3-(3-dimethylaminopropyl)carbodiimide (EDC) and 1 mM N-hydroxysuccinimide (NHS) in water and the pH of the solution was adjusted to a pH of 8.2 using NaOH.^{239,240} The amine terminated probe was incubated for approximately 1 hour and then rinsed for 5 minutes in DMSO and 5 minutes in ethanol and dried in air for approximately 10-15 minutes.

9.3.4 PEG bound MTX - AFM probe functionalization procedure

Silicon nitride probes were also functionalized with a polyethylene glycol (PEG) linker (Layson Bio, Inc.) between the AFM tip and MTX.^{241,242} The PEG3400 linker contained amine functionality at both ends of the polymer strand and a second, shorter PEG2000 was used as a blocking agent. A summary of the functionalization steps are as following: starting with, an amination step, followed by addition of the homo-bifunctional crosslinker, 1,4 phenylene diisocyanate (PDITC), addition of PEG3400 with biamine functionality, then by a blocking step of PEG2000 (only one amine functional end), and finally, MTX addition. In detail, ethanolamine in dry DMSO, 35% (v/v), was heated to 70 °C, cooled, then molecular sieve beads added. The tip was incubated in this solution for 5 hours followed by washing for 5 minutes in DMSO and ethanol.^{230,239,240} Then it was incubated for 2 hours in solution containing 10 mg PDITC dissolved in 10% (v/v) pyridine in dry DMSO¹¹ and washed again. A small amount of PEG3400 (0.1-0.2 mg) was dissolved in 10% (v/v) pyridine in dry DMSO in which the tip was submerged for 1 hour, followed by the washing procedure. A minimal amount of PEG3400 was used to keep the surface coverage low, which promotes single binding events. Then, 10 mg of PEG 2000 was dissolved in 10% (v/v) pyridine in dry DMSO to block any unbound sites and the tip was incubated in this solution overnight and washed in DMSO and ethanol. Finally, the MTX was bound via as in the directly bound MTX functionalization procedure described above.^{239,240}

Mass spectrometry measurements were performed on PEG 3400 to determine the length of the fully extended PEG linker and to access its polydispersity. The study was performed to ensure that the commercial PEG3400 is sufficiently monodisperse to allow

the force data to be filtered based on separation distance of rupture events, which directly relates to the length of the fully extended PEG linker. Mass spectrometry (Waters Q-TOF Premier) was performed and the distribution of mass to charge is reported in Figure 9.1. Fitting the data to a Gaussian distribution gave the mean MW and standard deviation of 3470 ± 160 g/mol. This corresponds to a fully stretched length of 24 ± 1 nm. The polydispersity index (PDI) was determined by the Equation 9.1:

$$\text{Polydispersity Index (PDI)} = \frac{M_w}{M_n} \quad (\text{Eq. 9.1})$$

M_w = Weight average molecular weight

M_n = Number average molecular weight

A perfectly monodispersed sample returns a PDI value of 1. The PDI for PEG3400 was determined to be 1.01, which implies that the PEG is sufficiently monodisperse.

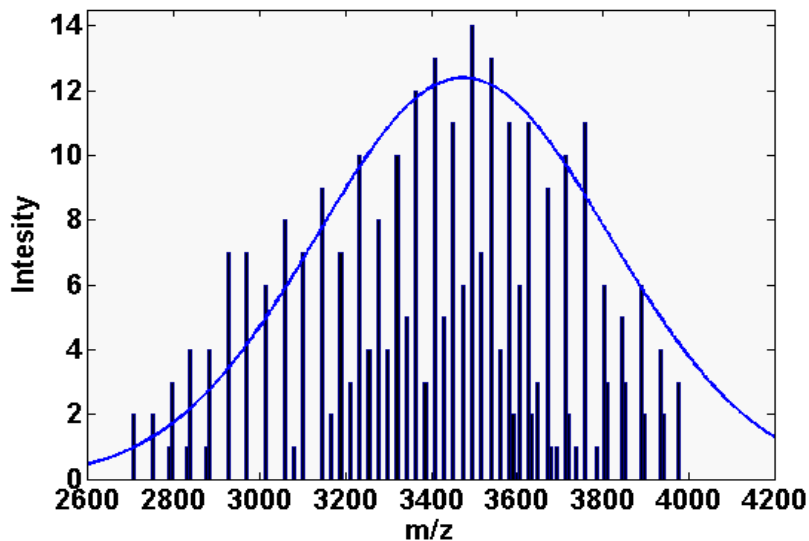


Figure 9.1: Distribution of mass spectrometry data used to assess the monodispersity and length of PEG3400.

9.3.5 dsDNA bound MTX - AFM probe functionalization procedure

dsDNA was also used to link MTX to the AFM probe. Amine and thiol terminated, 140 base-pair dsDNA was synthesized to be used as the linker as described elsewhere in the context of binding the enzyme to the substrate.²³⁶ First, ethanolamine in dry DMSO, 35% (v/v), was heated to 70 °C, cooled, then molecular sieve beads added. The tip was incubated in this solution for 4 hours followed by washing for 5 minutes in DMSO and ethanol.^{230,239,240} Then it was incubated for 2 hours in solution containing 10 mg PDITC dissolved in 10% (v/v) pyridine in dry DMSO and washed again.²⁴³ Next, 15 µl of dsDNA (0.7µM) was added to 5ml of 10% (v/v) pyridine in dry DMSO and the tip was incubated overnight causing functionalization via the amine group on the dsDNA to already bound PDITC. The tip was washed with DMSO and ethanol for 5 minutes each. Then, a blocking step was performed to bind any remaining open binding sites on the tip with ethanolamine for 1 hour followed by washing with DMSO and ethanol. Since the chemical procedure to attach MTX by an amine terminated probe was already established,^{239,240} an additional step before MTX attachment was added, utilizing a small molecule, cysteamine (Aldrich, 95% purity), which formed a disulfide bond with the thiol on dsDNA, leaving the tip amine terminated. In detail, 10 mg of cysteamine was dissolved in approximately 5 ml of 8 ng/µl tris(2-carboxyethyl)phosphine (TCEP) aqueous solution²⁴⁴ and the tip was incubated for 1 hour, then washed in water for 5 minutes. Finally, the tip was exposed to the same MTX solution used for other procedures for 30-60 minutes, followed by washing in ethanol for 5 minutes, and then dried in air for 10-15 minutes.^{239,240}

9.3.6 Substrate functionalization procedure of dsDNA on mica

This procedure has been described briefly by Singh et al.²³⁶ but is presented below in more details, including various controls used to verify the successful construction of the design..

Synthesis

Muscovite mica (V-I grade, SPI Supplies, Westchester, PA) was first cleaved with tape, leaving a clean, atomically flat surface for functionalization. Ethanolamine in dry DMSO, 35% (v/v), was heated to 70 °C, cooled, then molecular sieve beads added.^{230,239,240} The mica was incubated in the ethanolamine solution for 5 hours, then overnight in solution containing 10 mg PDITC dissolved in 10% (v/v) pyridine in dry DMSO.²⁴³ Approximately 3 µL dsDNA was dropped onto the mica plate and allowed to incubate for 1 hour. Small amounts of ultra-pure water were added to the plate periodically to prevent the solution from evaporating and drying. Next, approximately 8 µL ethanolamine, 10 µL TCEP (8ng/uL),²⁴⁴ and finally 10 µL activated wild type E. coli DHFR in MTEN buffer (200mM, pH 7.4) were exposed to the plate sequentially, each for one hour. The plate was rinsed (by submersion) after the first two steps with dry DMSO and ethanol, and between all other steps with ultra-pure water. The plates were used immediately. An activity assay found that the specific activity of the immobilized DHFR is not significantly different than that in solution.²³⁶

9.3.7 Control Experiments

Imaging dsDNA

For force spectroscopy experiments involving the dsDNA bound DHFR on mica, imaging of the substrate was first required in order to locate the individual dsDNA-

DHFR “pillars” on the surface. Representative height AFM image is show in Figure 9.2A. As seen in the representative cross section in Figure 9.2B, the height of the dsDNA was about 40nm, which agrees with the theoretical length of the 140 base pair dsDNA.

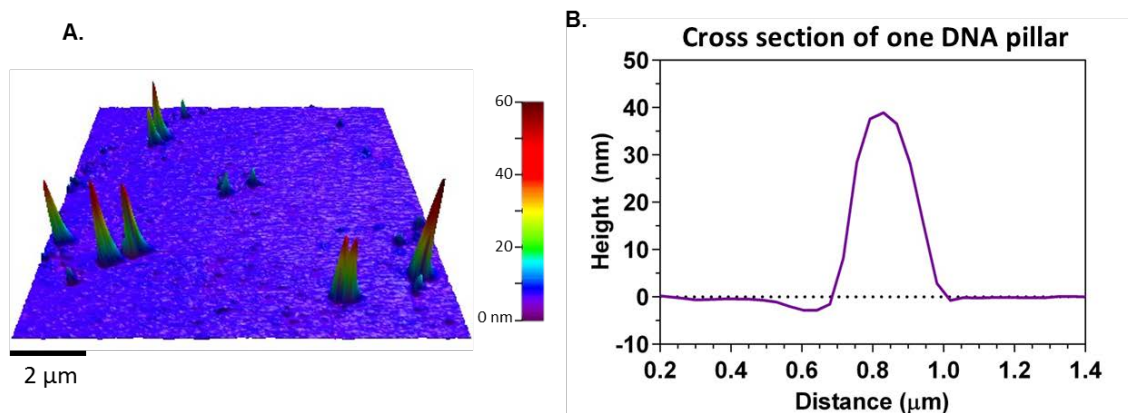


Figure 9.2: A. Representative AFM image of dsDNA pillars on gold. B. Typical cross section of one dsDNA pillar.

Measuring melting force of dsDNA

This dsDNA linking procedure on mica appears to result in robust areas of dsDNA-DHFR linked aggregates on the mica surface. The dsDNA plates reproducibly and repeatedly survived multiple rinsing cycles during the functionalization procedure and AFM (AC mode) imaging in liquid, which gave support to covalent attachment because molecules that were only physisorbed to the surface would likely be rinsed away.

To verify the covalent attachment of the dsDNA to the mica surface and to measure the melting force of dsDNA, the functionalization procedure was performed up until the point of activation of the DNA but before adding the enzyme. In other words, the surface was functionalized with dsDNA pillars with the thiol groups still exposed. A schematic of this setup is shown in Figure 9.3A for clarity. A gold-coated AFM tip was used to probe the exposed thiol and measure the interaction force. A representative force-distance cycle is shown in Figure 9.3B. The mean rupture force between the tip and functionalized areas of the surface was determined to be $1.0 \pm 0.05\text{nN}$ (Figure 9.3C), which is similar in magnitude of single thiol-gold interactions reported in the literature.²⁴⁵ Although, it should be noted that we cannot be certain which bond in the molecule construct is ruptured. This experiment was performed in both water and buffer and the

same result was achieved. Approximately 5% of all force plots collected for this control study had a small second adhesion event preceded by a horizontal feature in the force distance cycle (Figure 9.4). We attribute this to the two strands of DNA separating and sliding along each other creating the horizontal friction-link feature in the force plot.

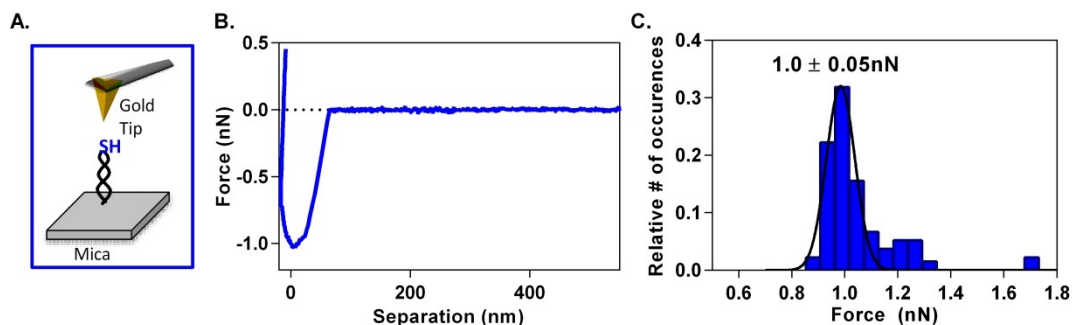


Figure 9.3: A. Cartoon of control experiment; dsDNA was functionalized on mica surface with thiol exposed. Interaction force was measured with a gold tip. B. Representative force plot. C. Distribution of forces between gold tip and dsDNA.

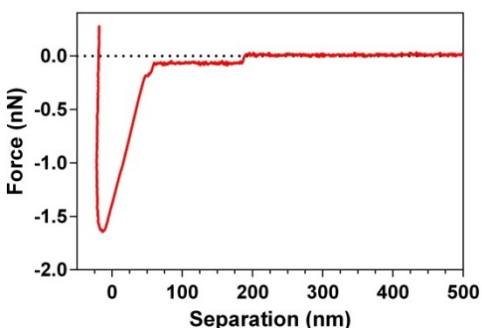


Figure 9.4: Additional force-distance profile (5% of total) observed for scenario deposited in Figure 9.3.

Furthermore, in order to verify that the forces associated with the experiment discussed above were not due to a large non-specific interaction, an additional control study was performed. The orientation of the dsDNA was essentially inverted (cartoon in Figure 9.5A). A solution of dsDNA was exposed to an ultra-flat gold surface for approximately one hour. In this type of functionalization, the thiol binds to the gold surface leaving the amine end of the DNA exposed. The force measurements were

repeated on this construct in buffer. Figure 9.5B shows a typical force distance profile between the gold tip and dsDNA. Figure 9.5C reports the distribution of forces associated with this experiment. It's apparent from the low magnitude of mean force (33 ± 12 pN) that the interaction forces measured here are purely non-specific, background force measurements. This supports the assumption that the interaction force measured in the previous control (Figure 9.4) is a specific interaction resulting from the thiol on the DNA binding to the gold tip.

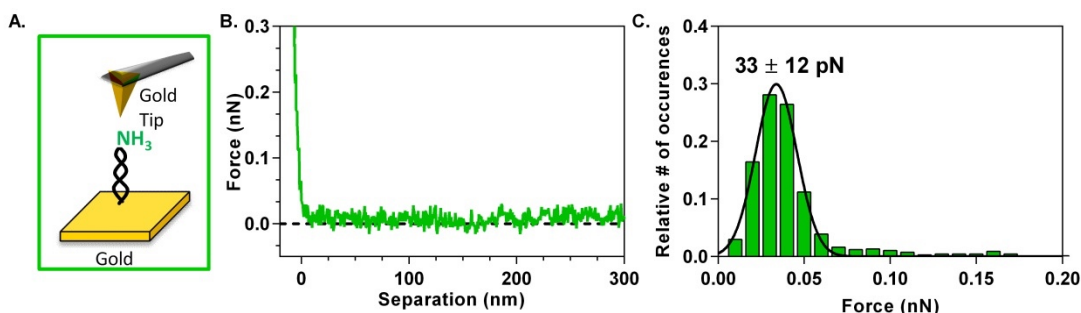


Figure 9.5: A. Pictorial representation of the control study performed; dsDNA was bound to a gold surface via the thiol end, leaving amine exposed. A gold tip was used to probe the interaction force between the DNA and tip. B. Representative force measurement. C. Distribution of forces.

The control studies reported here lead us to believe that the dsDNA used has a melting point $\geq 1.0 \pm 0.05$ nN. Thus, the DNA will not melt before MTX is ruptured from the active sight of DHFR.

Confirmation of MTX-Tip functionalization

Another concern with the construct in Figure 2E of the main text was confirming that MTX covalently binds the dsDNA on the AFM probe. A control study was performed by quantifying adhesion forces of the construct in Figure 9.2E without MTX (Figure 9.6A). Similar to procedure reported in the main text, the data was filtered to remove large adhesion events that occurred at <20 nm away from the surface. Two

representative force plots from this measurement are reported in Figure 9.6B and the distribution of forces is reported in Figure 9.6C. The mean rupture force is 52 ± 17 pN, which is much smaller than the interaction forces measured when MTX was present on the probe (195 ± 60 pN). Force plots with large adhesion event close to the surface comprised approximately 10% of the force plots (Figure 9.6D). We attribute this to the dsDNA on the tip interacting with either the DHFR or the dsDNA on the surface. This large non-specific interaction force was also present for construct reported in the main text in Figure 9.8. This measurement gives us confidence that the measurements reported in Figure 9.8E of the main text are specific to DHFR-MTX binding. For comparative purposes, Figure 9.6E shows force distance profiles overlaid for measurements with and without MTX covalently bound on the tip. As can be seen, when MTX is present there is a relatively large adhesion event that occurs at about 70nm away from the surface, which we attribute to the specific MTX-DHFR rupture event and is absent in the control study force profiles without MTX.

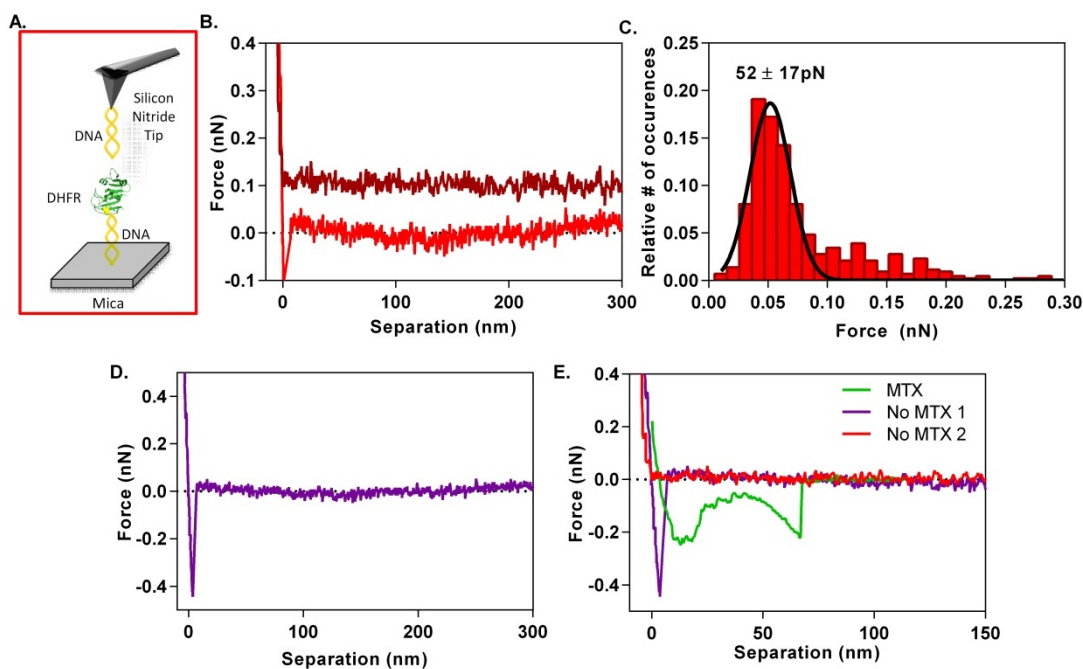


Figure 9.6: A. Pictorial representation of the control study performed; dsDNA-DHFR was bound to a mica surface and measured against a dsDNA functionalized AFM probe. B. Two representative force measurements. The dark red (top) force plot is offset by 100pN for clarity. C. Distribution of forces. D. Approximately 10% of the force plots showed a large nonspecific adhesion event near the surface which is attributed to dsDNA interacting with the DNA or DHFR on the surface. E. Three force plots are shown simultaneously for comparative purposes. The red and purple force profiles are from the scenario where no MTX is bound the end of the probe. The green force plot is from the experiment where MTX was present on the tip.

9.4 Results and Discussion

Escherichia coli Dihydrofolate reductase (DHFR) was selected as a model system for the study. DHFR is a key enzyme in the biosynthesis of DNA nucleotides and the target of the chemotherapeutic drug methotrexate (MTX), a tight-binding inhibitor of DHFR.²⁴⁶ Because it is a small monomeric enzyme, it has been utilized for many theoretical and experimental studies,^{247–256} making it an excellent model system to illustrate validity of the dsDNA linking approach for protein-drug interaction.

Force induced dsDNA melting has been the subject of many studies.^{103,257–262} Melting forces reported for dsDNA range from 17pN²⁶⁰ – 1.5nN²⁵⁸. Number of base pairs,²⁵⁸ loading rate,²⁵⁹ and sodium chloride concentration¹⁰³ directly affect the magnitude of force required to melt the DNA. Thus, it is highly dependent on the specific DNA sequence and experimental conditions. The melting force of the dsDNA used in this study was found to be $\geq 1.0 \pm 0.1$ nN (details of the control experiments are reported in section 9.3). Importantly, since the magnitude of rupture force of DHFR and MTX is around 200pN, the dsDNA won't melt before removal of MTX from the active site.

DHFR was covalently immobilized on mica surface using labelled dsDNA linkers. The 5' end of one strand of DNA was labelled with a thiol while the 5' end of the complementary strand was labelled with an amino group. DHFR from *E. coli* has two cysteine residues: one at the outer surface (C152), remote from the active site, and another deep inside an embraced region of the protein (C85). The amino end of the dsDNA was covalently tethered to an activated mica surface, while the thiol end formed a disulfide bond with the exposed cysteine (C152) of the enzyme. The C85 is unlikely to participate in binding while the enzyme is folded in its globular conformation. Additionally, a linker bound to C85 would abolish enzymatic activity and drug binding capacity, and thus will not affect the measurements presented below. One advantage of dsDNA-DHFR linked surface over an enzymatic monolayer is that the sample can be imaged to locate the dsDNA pillars (containing enzymes) (Figure 9.2), allowing data collection locations to be determined, which greatly facilitates efficient and site-specific force measurements.

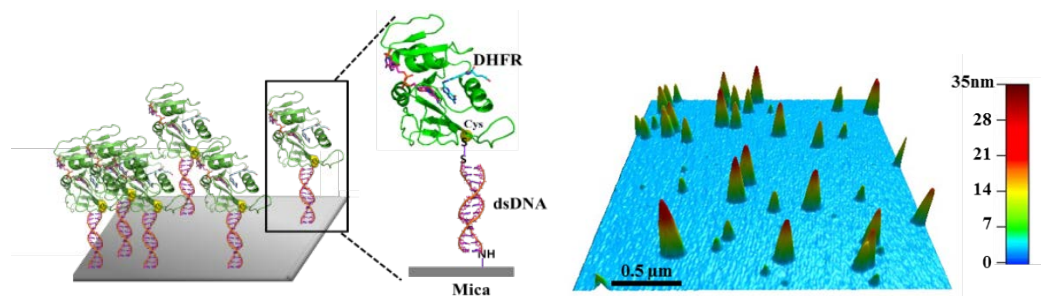


Figure 9.7: Left: Scheme of DHFR immobilization on mica with dsDNA spacer: the surface cysteine of DHFR is bound via a disulfide bond to 5'-thiol-labeled dsDNA. The dsDNA is bound to mica via amine at the 5'-terminal of the complementary strand. Reprinted with permission from the Analytical Biochemistry.²³⁶ Right: 3D AFM height image of dsDNA pillars on mica surface.

Given that any enzyme-immobilization may alter enzyme activity compared to solution, it was important to determine the catalytic activity of the immobilized enzyme. In the case of the DHFR monolayer on gold surface, we previously reported a k_{cat} value of $8.8 \pm 1.2 \text{ s}^{-1}$,⁵⁵ which is similar to that of DHFR in solution ($10\text{-}12 \text{ s}^{-1}$).²⁶³ For the dsDNA bound substrate, the surface coverage of the enzyme is much lower, thus determination of active site concentration was challenging. A novel method was developed and reported elsewhere,²³⁶ yielding measured k_{cat} of $6.7 \pm 0.6 \text{ s}^{-1}$, which indicates that immobilizing DHFR with dsDNA linker does not significantly change its catalytic activity.

The MRFS studies were performed and compared for 5 different linking scenarios, illustrated in Figure 9.8, A-E. Specifically, three different methods of covalently immobilizing MTX on the AFM tip were studied, and two of them were also compared for two different enzyme immobilization methods. The tip functionalization methods include a direct attachment, and also via a flexible PEG linker and a rigid dsDNA linker. The surface immobilization consisted of an enzymatic monolayer and

enzymes tethered via dsDNA. MRFS studies involved multiple force measurements collected at various sample positions. Upon retraction of the probe from the surface, the intermolecular contacts between surface-tethered DHFR and AFM tip bound MTX are ruptured. The force required to remove the probe from the contact with the sample is defined as the rupture force. A combination of force-distance profiles and values of the rupture forces are utilized here for the comparison between five different linking scenarios.

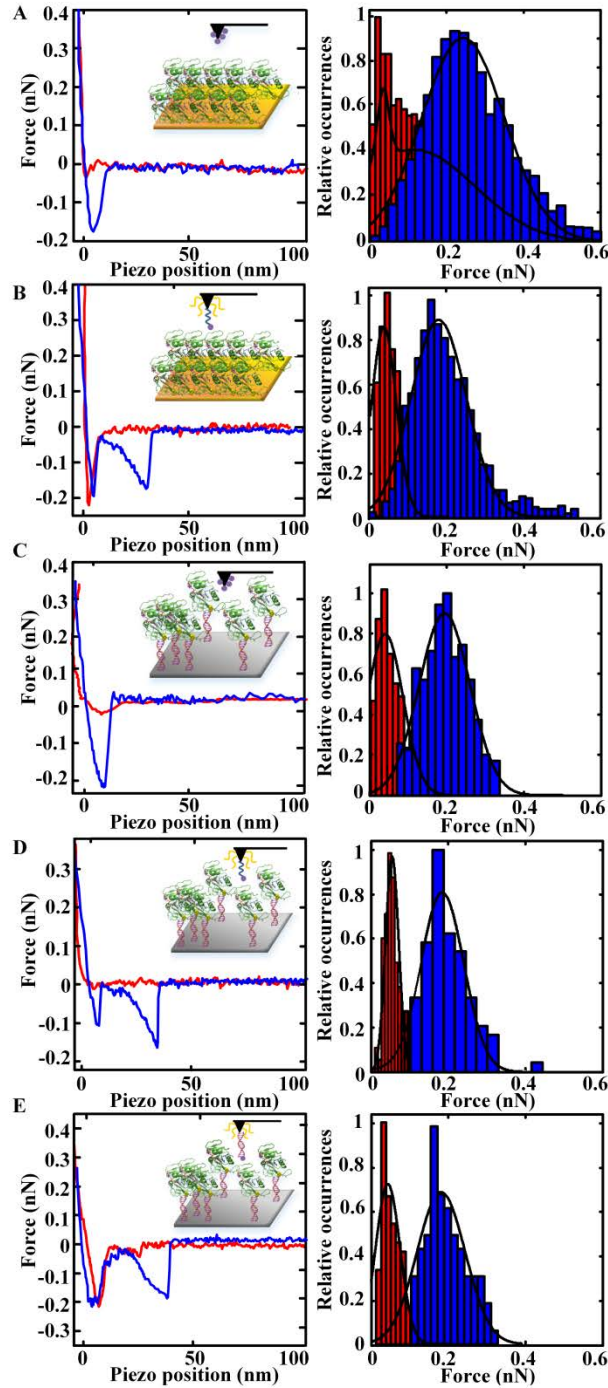


Figure 9.8: The left column shows typical force measurements (retract data only) and the right column presents distribution of rupture forces of DHFR and MTX (blue lines and bars) and MTX blocking study (red lines and bars) for the five immobilization scenarios illustrated in the inserts. Gaussian fits are shown by solid black lines. The data are summarized in Table 9.2.

Figure 9.8 presents a typical force-distance profile for experiments A-E (left panel, blue line), with the corresponding distribution of rupture forces to the right (blue histogram). Each histogram was fit to a single Gaussian, yielding the mean rupture force and standard deviation summarized in Table 9.2. Data was filtered based on theoretical tip-sample separation rupture distance dictated by the linkers on the tip. Tip contact with the top of the enzyme is defined as zero tip-sample separation and the experimental mean and standard deviation of rupture distances for each scenario are reported in Table 9.2. Scenario B has a rupture distance of 32 ± 8 nm, which is reasonable considering the length of a fully stretched PEG (~24 nm) and accounting the size of the enzyme (4 nm) and possibility of a partial unfolding prior to rupture. Scenario C has a short rupture distance of 6 ± 5.5 nm, consistent with the MTX directly bound on the tip. Scenarios D&E have rupture distances of 40 ± 15 nm and 49 ± 17 nm, respectively, both consistent with the lengths of fully stretched PEG (24 nm) and dsDNA (40 nm). Overall, the average rupture distances are consistent with what is expected from the dimensions of linkers on the tip or substrate.

Table 9.2: Rupture distances and mean rupture forces measured for the 5 linking scenarios before and after MTX blocking control study.

Linking Scenario	Rupture distance (nm)	Mean rupture force MTX-DHFR (pN)	Mean rupture force after MTX blocking (pN)
A ¹⁸	> 20	245 ± 120	100 ± 120
B	32 ± 8	230 ± 85	80 ± 65
C	6 ± 5.5	195 ± 60	90 ± 80
D	40 ± 15	185 ± 55	65 ± 55
E	49 ± 17	195 ± 60	45 ± 50

To ensure the measured forces are active-site specific, an important blocking control study is performed at the end of every data collection. In this control, the surface containing DHFR is submerged in ~200 μM MTX solution in MTEN buffer (pH 7.4) for approximately 20 minutes to saturate all active sites, and then force measurements are performed once again. The distribution of forces after blocking all enzymes active sites with MTX arises from non-specific interaction forces. When analyzing this control the same range of tip-sample separations (determined from piezo positions) was used as for the active-site specific analysis, which dramatically reduced the uncertainty when spacers were added to the tip (scenarios B, D, and E). Additionally, for dsDNA-modified surfaces, force data was also collected on areas in the AFM image that appeared to contain no dsDNA pillars. Thus, the adhesion forces are non-specific and arise from the tip interacting with the bare substrate and the distribution of forces is significantly lower ($35 \pm 20\text{pN}$) compared to specific binding collected on the dsDNA-enzyme spots.

A typical force-distance profile obtained before (blue) and after (red) the blocking control is presented at the left column of Figure 9.8, with the corresponding distribution at the right. Noticeably, while the non-specific force distribution (red) has lower force values, it nonetheless overlaps to different degrees with the force distribution of DHFR-MTX in the active site specific rupture experiment (blue). This overlap is maximal in scenario A and dramatically reduced in scenarios D and E. Additionally, the standard deviation associated with the quantification of specific rupture forces is also decreasing from scenarios A to E, indicating broad distribution of states in the former. This demonstrates the distribution of behaviors of individual enzyme molecules that can only be examined in a single molecule experiments. Additionally, in the experimental scenario

A (directly-bound MTX tip and enzymatic monolayer), the width of the distribution likely reflects more than a single dissociation event. In order to more precisely quantify the specific binding forces, non-specific forces must be separated and minimized, which is the goal of the examination of the different scenarios.

In scenario B, a PEG-bound MTX tip is tested against enzymatic monolayer. The most noticeable difference between the directly bound MTX tip data in A and the PEG bound force plot in B is that PEG has a non-linear stretching characteristic and the rupture event occurs at a larger distance from the surface. This is advantageous as it allows separation between the interaction force of DHFR and MTX from the majority of non-specific forces that occur when the tip is in close proximity to the sample surface. Only force plots that demonstrated the non-linear characteristic stretching of PEG and DHFR were analyzed. Furthermore, the force plots used for quantification were sorted based on the piezo position in which the rupture event occurred. Since non-specific interactions typically occur at small tip-sample separation distances, force plots containing ruptures occurring at a piezo position of 5 nm or less were eliminated from the data. Since the maximum distance where the rupture event could occur at is governed by the length of a fully-stretched PEG linker (and ~5-10 nm associated with the enzyme stretching), events occurring at tip-sample separation distances of approximately 35 nm or larger were also eliminated. The PEG-bound MTX tip returns essentially the same average dissociation force as the directly bound MTX scenario (230 ± 85 vs. 245 ± 120 pN). However, a significant decrease in the standard deviation indicates the quantification is more precise. Another noticeable improvement is that the distribution of rupture forces for scenario B after blocking of active sites with free MTX is much smaller

than in scenario A, and only slightly overlaps with the specific DHFR-MTX force distribution, indicating a decrease in contribution from non-specific interactions.

In scenario C (directly-bound MTX tip and dsDNA bound DHFR on mica), the rupture event occurs when the tip is still relatively close to the surface and therefore, non-specific forces contribute to the measurement. However, despite this disadvantage, relative to scenario A there is still a significant decrease in both the standard deviation of the measurement, as well as decreased overlap of the force distributions before and after the MTX blocking. In scenarios C-E, the presence of single molecules bounded through dsDNA decreases the possibility of probing multiple bound complexes, as indicated by the lower quantification of mean rupture force than scenarios A and B (see Table 9.2).

Scenario D combines the advantageous of scenarios B and C by using a PEG linker on the AFM tip and the dsDNA linker on the mica substrate. The PEG linker on the probe, again, presented a separation of the force plots based on separation distance of the rupture force, which can be seen in the experimental force plot in Figure 9.8D. Interestingly, the distribution of states was the same as in the Scenario C (judging from the standard deviation). The distribution after treatment with free MTX, however, was substantially reduced, indicating the advantage of separating the MTX from the tip using a spacer.

Finally, in Scenario E dsDNA linkers were employed on both the surface and the AFM tip. The experimental force plots show a relatively large non-specific interaction event at small tip-sample separation distance, likely due to interactions between the two dsDNA linkers, followed by a second rupture event at larger tip-sample separation. This non-specific contribution force typically occurred at separation distances less than 20 nm

and also occurred when the construct in E was measured without MTX present on the dsDNA tip. This interpretation is further supported by the fact that this interaction is not affected by the free MTX blocking (see red and blue traces in Figure 9.8E, left column). Therefore, the forces used for quantification of the mean rupture force were the stretching events that occurred at approximately 40 nm tip-sample separation distance and the average experimental rupture distance was 49 ± 17 nm. In this fashion, the mean rupture force was determined to be the same as in scenarios C and D (195 ± 60 pN), but the MTX blocking resulted in significant shift to smaller rupture force (45 ± 50 pN), indicating a significant advantage using the rigid dsDNA for the separation of the MTX from the tip.

9.5 Conclusions

In conclusion, we have demonstrated that examining single enzyme molecules with rigid dsDNA spacers on both the surface and the tip yield similar uncertainty in the distribution of forces compared to the PEG linker. However, the dsDNA linker offers more rigidity than PEG. Consequently, a dsDNA linker could be employed in MRFS experiments where it is advantageous to engineer the system so that the enzyme's active site is readily accessible, for example. Or, if it is not ideal for the linker to unfold before the probe is removed. This methodology is not limited to enzyme–drug interactions, and can be adaptable to study many types of ligand-receptor systems.

10. CONCLUSIONS AND FUTURE WORK

10.1 SSA Single Particle Measurements

The overarching theme of work performed here on single particle SSA focusses on developing new AFM methodologies to characterize physiochemical properties of aerosols. Several new methodologies have been developed and validated including surface tension measurements, morphology analysis, water uptake, and organic volume fraction. These measurements can be applied to complex aerosol particles of unknown composition in the future.

Surface tension measurements on single component model systems have being performed and compared to the expected bulk responses. Organic model systems deviate from the expected responses at low RH and high concentration values. These phenomena need to be further explored. More single component model systems should be explored as well as mixtures of salts and organics. These include magnesium sulfate, mixtures of chlorides, sucrose, glucose, lipopolysaccharide, and long chain carboxylic acids like palmitic acid. AFM based 3D morphological analysis and aspect ratio of particles is being further developed to help facilitate distinguishing between particles of different chemical compositions. This methodology development needs to be performed and closely studied on model systems and then applied to nascent SSA. The methodology to accurately measure the water uptake of individual SSA particles has been established and factors that influence the growth of droplets upon absorbing water have been established. This methodology has being applied to complex aerosol particles and data analysis is currently underway.

All of these methodology development techniques can also be performed as a function of temperature. Since, the temperature of the atmosphere can be drastically different than ambient temperature, it is important to understand these phenomena at more relevant and diverse temperatures. A temperature cell attached to the AFM head allows temperature dependent AFM studies. Future studies should focus on examining water uptake and surface tension as a function of temperature, which will allow insight into the CCN ability of particles. Furthermore, the process of ice nucleation in the atmosphere is poorly understood. Low temperature AFM studies on single particles could reveal what types and sizes of particles are efficient at nucleating ice. A single molecule approach measuring the free energy of binding of freezing and antifreezing proteins to ice surfaces could allow some fundamental insights on ice nucleation and protein-ice interactions. It should also be noted that to accurately perform the studies mentioned here, RH and temperature will have to be monitored and controlled simultaneously and the experimental cell is currently being developed.

10.2 Molecular Recognition studies

The methodology developed here facilitates future studies on other biochemical systems and the improved accuracy allows detection of small rupture forces without the influence of non-specific interaction forces. The interaction strength between DHFR and folate and other ligands could be probed in the future, as well as in the presence of cofactors, which may affect the binding strength of the ligand.

The ultimate goal of this research is to be able to monitor force-controlled motions associated with enzymatic function in real time. To facilitate these measurements, a rigid linker was necessary. The work reported here has established rigid

dsDNA as a viable linker in MRFS experiments and can be utilized in the future to tether molecules to both the AFM probe and the surface. To perform these experiments, the thermal drift of the AFM tip must be minimized, as even a small motion will disrupt the sensitive measurement. A heating unit has been added to the AFM chamber in order to minimize thermal drift. This system needs to be optimized for the enzymatic measurement for future studies.

REFERENCES

- (1) Zavala, G. *Colloid Polym. Sci.* **2007**, *286*, 85–95.
- (2) Alessandrini, A.; Facci, P. *Meas. Sci. Technol.* **2005**, *16* (6), R65–R92.
- (3) Gan, Y. *Surf. Sci. Rep.* **2009**, *64* (3), 99–121.
- (4) Diebold, U. *Surf. Sci. Rep.* **2003**, *48* (5-8), 53–229.
- (5) Jandt, K. *Surf. Sci.* **2001**, *491*, 303–332.
- (6) Butt, H. J.; Cappella, B.; Kappl, M. *Surf. Sci. Rep.* **2005**, *59* (1-6), 1–152.
- (7) Binnig, G.; Rohrer, H. *Surf. Sci.* **1982**, *126* (126), 236–244.
- (8) Prior, M.; Makarovski, a.; Finkelstein, G. *Appl. Phys. Lett.* **2007**, *91* (5), 053112.
- (9) Morris, H. S.; Grassian, V. H.; Tivanski, A. V. *Chem. Sci.* **2015**, *6*, 3242–3247.
- (10) Hansma, P. K.; Cleveland, J. P.; Radmacher, M.; Walters, D. A.; Hillner, P. E.; Bezanilla, M.; Fritz, M.; Vie, D.; Hansma, H. G.; Prater, C. B.; Massie, J.; Fukunaga, L.; Gurley, J.; Elings, V. *Appl. Phys. Lett.* **1994**, *64* (13), 1738.
- (11) McMurry, P. H. *Atmos. Environ.* **2000**, *34* (12-14), 1959–1999.
- (12) Williams, J.; de Reus, M.; Krejci, R.; Fischer, H.; Ström, J. *Atmos. Chem. Phys. Discuss.* **2002**, *2* (1), 43–74.
- (13) Lowe, D. C.; Zealand, N. *Change* **2007**, *30* (22), 129–234.
- (14) Kanakidou, M.; Seinfeld, J. H.; Pandis, S. N.; Barnes, I.; Dentener, F. J.; Facchini, M. C.; Van Dingenen, R.; Ervens, B.; Nenes, a.; Nielsen, C. J.; Swietlicki, E.; Putaud, J. P.; Balkanski, Y.; Fuzzi, S.; Horth, J.; Moortgat, G. K.; Winterhalter, R.; Myhre, C. E. L.; Tsigaridis, K.; Vignati, E.; Stephanou, E. G.; Wilson, J. *Atmos. Chem. Phys.* **2005**, *5* (4), 1053–1123.

- (15) Penner, J.E. and Andreae, M. and Annegarn, H. and Barrie, L. and Feichter, J. and Hegg, D. and Jayaraman, A. and Leaitch, R. and Murphy, D. and Nganga, J. and Pitari, G. *Clim. Chang. 2001 Sci. c Basis. Contrib. Work. Gr. I to Third Assess. Rep. Intergov. Panel Clim. Chang. [Houghton, J.T., al. (eds.)].* **2001**, 289–348.
- (16) Ghahremaninezhad, R.; Norman, A.-L.; Abbatt, J. P. D.; Levasseur, M.; Thomas, J. L. *Atmos. Chem. Phys. Discuss.* **2016**, No. February, 1–27.
- (17) CHARLSON, R. J.; SCHWARTZ, S. E.; HALES, J. M.; CESS, R. D.; COAKLEY, J. A.; HANSEN, J. E.; HOFMANN, D. J. *Science (80-.).* **1992**, 255 (5043), 423–430.
- (18) Ogren, J. a.; Charlson, R. J. *Tellus B* **1983**, 35B (4), 241–254.
- (19) Charlson, R. J.; Lovelock, J. E.; Andreae, M. O.; Warren, S. G. *Nature* **1987**, 326, 655–661.
- (20) Tang, J.; Wang, P.; Mickley, L. J.; Xia, X.; Liao, H.; Yue, X.; Sun, L.; Xia, J. *Atmos. Environ.* **2014**, 84, 244–253.
- (21) Rosinski, J.; Haagenson, P. L.; Nagamoto, C. T.; Quintana, B.; Parungo, F.; Hoyt, S. D. *J. Aerosol Sci.* **1988**, 19 (5), 539–551.
- (22) Farmer, D. K.; Cappa, C. D.; Kreidenweis, S. M. *Chem. Rev.* **2015**, 150313151440005.
- (23) Kohler, H. *Trans. Faraday Soc.* **1936**, 32 (1152), 1152.
- (24) Sun, J.; Ariya, P. a. *Atmos. Environ.* **2006**, 40 (5), 795–820.
- (25) Bertram, a. K.; Martin, S. T.; Hanna, S. J.; Smith, M. L.; Bodsworth, a.; Chen, Q.; Kuwata, M.; Liu, a.; You, Y.; Zorn, S. R. *Atmos. Chem. Phys.* **2011**, 11 (21), 10995–11006.

- (26) Dennis-Smith, B. J.; Hanford, K. L.; Kwamena, N. O. a; Miles, R. E. H.; Reid, J. *P. J. Phys. Chem. A* **2012**, *116* (24), 6159–6168.
- (27) Morris, H. S.; Estill, A. D.; Laskina, O.; Grassian, V. H.; Tivanski, A. V. *Anal. Chem.* **2015**, *2016* (1).
- (28) Thornton, J. A.; Braban, C. F.; Abbatt, J. P. D. *Phys. Chem. Chem. Phys.* **2003**, *5* (20), 4593–4603.
- (29) Ovadnevaite, J.; Ceburnis, D.; Martucci, G.; Bialek, J.; Monahan, C.; Rinaldi, M.; Facchini, M. C.; Berresheim, H.; Worsnop, D. R.; O’Dowd, C. *Geophys. Res. Lett.* **2011**, *38* (21), 1–5.
- (30) Prisle, N. L.; Raatikainen, T.; Sorjamaa, R.; Svenningsson, B.; Laaksonen, A.; Bilde, M. *Tellus, Ser. B Chem. Phys. Meteorol.* **2008**, *60 B* (3), 416–431.
- (31) Laskina, O.; Morris, H. S.; Grandquist, J. R.; Qin, Z.; Stone, E. a.; Tivanski, A. V.; Grassian, V. H. *J. Phys. Chem. A* **2015**, *119* (19), 4489–4497.
- (32) Ghorai, S.; Tivanski, A. V. *Anal. Chem.* **2010**, *82* (22), 9289–9298.
- (33) Aumann, E.; Hildemann, L. M.; Tabazadeh, a. *Atmos. Environ.* **2010**, *44* (3), 329–337.
- (34) Facchini, M. C.; Mircea, M.; Fuzzi, S.; Charlson, R. J. *Nature* **1999**, *401* (6750), 257–259.
- (35) Prisle, N. L.; Asmi, a.; Topping, D.; Partanen, a. I.; Romakkaniemi, S.; Dal Maso, M.; Kulmala, M.; Laaksonen, a.; Lehtinen, K. E. J.; McFiggans, G.; Kokkola, H. *Geophys. Res. Lett.* **2012**, *39* (5), 1–5.
- (36) Topping, D. O.; McFiggans, G. B.; Kiss, G.; Varga, Z.; Facchini, M. C.; Decesari, S.; Mircea, M. *Atmos. Chem. Phys. Discuss.* **2006**, *6* (6), 12057–12120.

- (37) Tuckermann, R. *Atmos. Environ.* **2007**, *41* (29), 6265–6275.
- (38) Tuckermann, R.; Cammenga, H. K. *Atmos. Environ.* **2004**, *38* (36), 6135–6138.
- (39) Textor, C.; Schulz, M.; Guibert, S.; Kinne, S.; Balkanski, Y.; Bauer, S.; Bernsten, T.; Berglen, T.; Boucher, O.; Chin, M.; Dentener, F.; Diehl, T.; Easter, R.; Feichter, H.; Fillmore, D.; Ghan, S.; Ginoux, P.; Gong, S.; Grini, A.; Hendricks, J.; Horowitz, L.; Huang, P.; Isaksen, I.; Iversen, T.; Kloster, S.; Koch, D.; Kirkevåg, A.; Kristjansson, J. E.; Krol, M.; Lauer, A.; Lamarque, J. F.; Liu, X.; Montanaro, V.; Myhre, G.; Penner, J.; Pitari, G.; Lamarque, J. F.; Liu, X.; Montanaro, V.; Myhre, G.; Penner, J.; Pitari, G.; Reddy, S.; Seland, Ø.; Stier, P.; Takemura, T.; Tie, X. *Atmos. Chem. Phys.* **2006**, *6*, 1777–1813.
- (40) Stokes, M. D.; Deane, G. B.; Prather, K.; Bertram, T. H.; Ruppel, M. J.; Ryder, O. S.; Brady, J. M.; Zhao, D. *Atmos. Meas. Tech.* **2013**, *6* (4), 1085–1094.
- (41) Of, J.; Oceanography, P.; Engineering, O. **2002**, No. Wu 1989, 3286–3290.
- (42) Burrows, S. M.; Ogunro, O.; Frossard, A. A.; Russell, L. M.; Rasch, P. J.; Elliott, S. *Atmos. Chem. Phys. Discuss.* **2014**, *14* (5), 5375–5443.
- (43) Cavalli, F.; Facchini, M. C.; Decesari, S.; Mircea, M.; Emblico, L.; Fuzzi, S.; Ceburnis, D.; Yoon, Y. J.; O’Dowd, C. D.; Putaud, J. P.; Dell’Acqua, A. *J. Geophys. Res. D Atmos.* **2004**, *109* (24), 1–14.
- (44) Ault, A. P.; Moffet, R. C.; Baltrusaitis, J.; Collins, D. B.; Ruppel, M. J.; Cuadra-Rodriguez, L. a.; Zhao, D.; Guasco, T. L.; Ebben, C. J.; Geiger, F. M.; Bertram, T. H.; Prather, K. a.; Grassian, V. H. *Environ. Sci. Technol.* **2013**, *47* (11), 5603–5612.

- (45) Gantt, B.; Meskhidze, N.; Facchini, M. C.; Rinaldi, M.; Ceburnis, D.; O'Dowd, C. *D. Atmos. Chem. Phys.* **2011**, *11* (16), 8777–8790.
- (46) Garcia, E.; Hill, T. C. J.; Prenni, A. J.; DeMott, P. J.; Franc, G. D.; Kreidenweis, S. *M. J. Geophys. Res. Atmos.* **2012**, *117* (17), 1–12.
- (47) Leck, C.; Bigg, E. K. *Tellus, Ser. B Chem. Phys. Meteorol.* **2005**, *57* (4), 305–316.
- (48) O'Dowd, C. D.; Facchini, M. C.; Cavalli, F.; Ceburnis, D.; Mircea, M.; Decesari, S.; Fuzzi, S.; Yoon, Y. J.; Putaud, J.-P. *Nature* **2004**, *431* (7009), 676–680.
- (49) Leck, C.; Bigg, E. K. *Tellus, Ser. B Chem. Phys. Meteorol.* **2008**, *60 B* (1), 118–126.
- (50) Elliott, S.; Burrows, S. M.; Deal, C.; Liu, X.; Long, M.; Ogunro, O.; Russell, L. M.; Wingenter, O. *Environ. Res. Lett.* **2014**, *9* (6), 064012.
- (51) Mochida, M.; Kitamori, Y.; Kawamura, K.; Nojiri, Y.; Suzuki, K. *J. Geophys. Res. Atmos.* **2002**, *107* (17).
- (52) Ault, A. P.; Zhao, D.; Ebben, C. J.; Tauber, M. J.; Geiger, F. M.; Prather, K. a; Grassian, V. H. *Phys. Chem. Chem. Phys.* **2013**, *15* (17), 6206–6214.
- (53) Wang, M. D.; Schnitzer, M. J.; Yin, H.; Landick, R.; Gelles, J.; Block, S. M. *Science* **1998**, *282* (5390), 902–907.
- (54) Duf r ne, Y. F.; Mart nez-Mart n, D.; Medalsy, I.; Alsteens, D.; M ller, D. J. *Nat. Methods* **2013**, *10* (9), 847–854.
- (55) Ditzler, L. R.; Sen, A.; Gannon, M. J.; Kohen, A.; Tivanski, A. V. *J. Am. Chem. Soc.* **2011**, *133* (34), 13284–13287.

- (56) Prather, K. a; Bertram, T. H.; Grassian, V. H.; Deane, G. B.; Stokes, M. D.; Demott, P. J.; Aluwihare, L. I.; Palenik, B. P.; Azam, F.; Seinfeld, J. H.; Moffet, R. C.; Molina, M. J.; Cappa, C. D.; Geiger, F. M.; Roberts, G. C.; Russell, L. M.; Ault, A. P.; Baltrusaitis, J.; Collins, D. B.; Corrigan, C. E.; Cuadra-Rodriguez, L. a; Ebben, C. J.; Forestieri, S. D.; Guasco, T. L.; Hersey, S. P.; Kim, M. J.; Lambert, W. F.; Modini, R. L.; Mui, W.; Pedler, B. E.; Ruppel, M. J.; Ryder, O. S.; Schoepp, N. G.; Sullivan, R. C.; Zhao, D. *Proc. Natl. Acad. Sci. U. S. A.* **2013**, *110* (19), 7550–7555.
- (57) Baltrusaitis, J.; Grassian, V. H. *J. Phys. Chem. A* **2012**, *3*, 9001–9009.
- (58) Satsangi, P. G.; Yadav, S.; Pipal, A. S.; Kumbhar, N. *Atmos. Environ.* **2014**, *92*, 384–393.
- (59) Sobanska, S.; Falgayrac, G.; Rimetz-Planchon, J.; Perdrix, E.; Brémard, C.; Barbillat, J. *Microchem. J.* **2014**, *114*, 89–98.
- (60) Jung, H.-J.; Eom, H.-J.; Kang, H.-W.; Moreau, M.; Sobanska, S.; Ro, C.-U. *Analyst* **2014**, *139* (16), 3949–3960.
- (61) Sobanska, S.; Hwang, H.; Choël, M.; Jung, H. J.; Eom, H. J.; Kim, H.; Barbillat, J.; Ro, C. U. *Anal. Chem.* **2012**, *84* (7), 3145–3154.
- (62) Tumolva, L.; Park, J.-Y.; Park, K. *Microsc. Res. Tech.* **2012**, *75* (4), 505–512.
- (63) Buscema, M.; Steele, G. a.; van der Zant, H. S. J.; Castellanos-Gomez, A. *Nano Res.* **2014**, *7* (4), 1–50.
- (64) Maver, U.; Planinšek, O.; Jamnik, J.; Hassanien, A. I.; Gaberšček, M. *Acta Chim. Slov.* **2012**, *59* (1), 212–219.

- (65) Homma, Y.; Suzuki, S.; Kobayashi, Y.; Nagase, M.; Takagi, D. *Appl. Phys. Lett.* **2004**, *84* (10), 1750–1752.
- (66) Momiuchi, Y.; Yamada, K.; Kato, H.; Homma, Y.; Hibino, H.; Odahara, G.; Oshima, C. *J. Phys. D. Appl. Phys.* **2014**, *47* (45), 455301.
- (67) Wise, M. E.; Martin, S. T.; Russell, L. M.; Buseck, P. R. *Aerosol Sci. Technol.* **2008**, *42* (January 2015), 281–294.
- (68) Semeniuk, T. a.; Wise, M. E.; Martin, S. T.; Russell, L. M.; Buseck, P. R. *Atmos. Environ.* **2007**, *41* (29), 6225–6235.
- (69) Peckhaus, A.; Grass, S.; Treuel, L.; Zellner, R. **2012**.
- (70) You, Y.; Renbaum-Wolff, L.; Carreras-Sospedra, M.; Hanna, S. J.; Hiranuma, N.; Kamal, S.; Smith, M. L.; Zhang, X.; Weber, R. J.; Shilling, J. E.; Dabdub, D.; Martin, S. T.; Bertram, a. K. *Proc. Natl. Acad. Sci.* **2012**, *109* (33), 13188–13193.
- (71) O'Brien, R. E.; Wang, B.; Kelly, S. T.; Lundt, N.; You, Y.; Bertram, A. K.; Leone, S. R.; Laskin, A.; Gilles, M. K. *Environ. Sci. Technol.* **2015**, *49* (8), 4995–5002.
- (72) Eom, H. J.; Gupta, D.; Li, X.; Jung, H. J.; Kim, H.; Ro, C. U. *Anal. Chem.* **2014**, *86* (5), 2648–2656.
- (73) Zhou, Q.; Pang, S.; Wang, Y.; Ma, J.; Zhang, Y. **2014**.
- (74) Wagner, G. *Sci. Total Environ.* **1995**, *176*, 63–71.
- (75) Eatough, D. J.; Obeidi, F.; Pang, Y.; Ding, Y.; Eatough, N. L.; Wilson, W. E. *Atmos. Environ.* **1999**, *33* (17), 2835–2844.
- (76) Dillner, A. M.; Phuah, C. H.; Turner, J. R. *Atmos. Environ.* **2009**, *43* (37), 5937–5943.
- (77) Gilkey, J. C.; Staehelin, L. A. *J. Electron Microsc. Tech.* **1986**, *3* (2), 177–210.

- (78) Facchini, M. C.; Rinaldi, M.; Decesari, S.; Carbone, C.; Finessi, E.; Mircea, M.; Fuzzi, S.; Ceburnis, D.; Flanagan, R.; Nilsson, E. D.; de Leeuw, G.; Martino, M.; Woeltjen, J.; O'Dowd, C. D. *Geophys. Res. Lett.* **2008**, *35* (17), 1–5.
- (79) Collins, D. B.; Ault, A. P.; Moffet, R. C.; Ruppel, M. J.; Cuadra-Rodriguez, L. a.; Guasco, T. L.; Corrigan, C. E.; Pedler, B. E.; Azam, F.; Aluwihare, L. I.; Bertram, T. H.; Roberts, G. C.; Grassian, V. H.; Prather, K. a. *J. Geophys. Res. Atmos.* **2013**, *118* (15), 8553–8565.
- (80) Chen, Q.; Farmer, D. K.; Schneider, J.; Zorn, S. R.; Heald, C. L.; Karl, T. G.; Guenther, a.; Allan, J. D.; Robinson, N.; Coe, H.; Kimmel, J. R.; Pauliquevis, T.; Borrmann, S.; Pöschl, U.; Andreae, M. O.; Artaxo, P.; Jimenez, J. L.; Martin, S. T. *Geophys. Res. Lett.* **2009**, *36* (20), 1–5.
- (81) Zhang, Q.; Jimenez, J. L.; Canagaratna, M. R.; Allan, J. D.; Coe, H.; Ulbrich, I.; Alfarra, M. R.; Takami, A.; Middlebrook, A. M.; Sun, Y. L.; Dzepina, K.; Dunlea, E.; Docherty, K.; DeCarlo, P. F.; Salcedo, D.; Onasch, T.; Jayne, J. T.; Miyoshi, T.; Shimo, A.; Hatakeyama, S.; Takegawa, N.; Kondo, Y.; Schneider, J.; Drewnick, F.; Borrmann, S.; Weimer, S.; Demerjian, K.; Williams, P.; Bower, K.; Bahreini, R.; Cottrell, L.; Griffin, R. J.; Rautiainen, J.; Sun, J. Y.; Zhang, Y. M.; Worsnop, D. R. *Geophys. Res. Lett.* **2007**, *34* (13), n/a – n/a.

- (82) Jimenez, J. L.; Canagaratna, M. R.; Donahue, N. M.; Prevot, A. S. H.; Zhang, Q.; Kroll, J. H.; DeCarlo, P. F.; Allan, J. D.; Coe, H.; Ng, N. L.; Aiken, A. C.; Docherty, K. S.; Ulbrich, I. M.; Grieshop, A. P.; Robinson, A. L.; Duplissy, J.; Smith, J. D.; Wilson, K. R.; Lanz, V. A.; Hueglin, C.; Sun, Y. L.; Tian, J.; Laaksonen, A.; Raatikainen, T.; Rautiainen, J.; Vaattovaara, P.; Ehn, M.; Kulmala, M.; Tomlinson, J. M.; Collins, D. R.; Cubison, M. J.; Dunlea, J.; Huffman, J. A.; Onasch, T. B.; Alfarra, M. R.; Williams, P. I.; Bower, K.; Kondo, Y.; Schneider, J.; Drewnick, F.; Borrmann, S.; Weimer, S.; Demerjian, K.; Salcedo, D.; Cottrell, L.; Griffin, R.; Takami, A.; Miyoshi, T.; Hatakeyama, S.; Shimono, A.; Sun, J. Y.; Zhang, Y. M.; Dzepina, K.; Kimmel, J. R.; Sueper, D.; Jayne, J. T.; Herndon, S. C.; Trimborn, A. M.; Williams, L. R.; Wood, E. C.; Middlebrook, A. M.; Kolb, C. E.; Baltensperger, U.; Worsnop, D. R. *Science* (80-.). **2009**, 326 (5959), 1525–1529.
- (83) Ott, D. K.; Cyrs, W.; Peters, T. M. *J. Aerosol Sci.* **2008**, 39 (2), 156–167.
- (84) Kuwata, M.; Kondo, Y. *Atmos. Chem. Phys. Discuss.* **2009**, 9 (1), 4653–4689.
- (85) Zhu, G.; Zhu, X.; Fan, Q.; Wan, X. *Spectrochim. Acta - Part A Mol. Biomol. Spectrosc.* **2011**, 78 (3), 1187–1195.
- (86) Terenziani, F.; Painelli, A.; Comoretto, D. *J. Phys. Chem. A* **2000**, 104 (47), 11049–11054.
- (87) Bougeard, D.; de Villepin, J.; Novak, A. *Spectrochim. Acta Part A Mol. Spectrosc.* **1988**, 44 (12), 1281–1286.
- (88) De Villepin, J.; Limage, M. H.; Novak, A.; Toupry, N.; Le Postollec, M.; Poulet, H.; Ganguly, S.; Rao, C. N. R. *J. Raman Spectrosc.* **1984**, 15 (1), 41–46.

- (89) Smith, M. L.; Bertram, A. K.; Martin, S. T. *Atmos. Chem. Phys.* **2012**, *12* (20), 9613–9628.
- (90) Smith, M. L.; You, Y.; Kuwata, M.; Bertram, A. K.; Martin, S. T. *J. Phys. Chem. A* **2013**, *117* (36), 8895–8906.
- (91) Smith, M. L.; Kuwata, M.; Martin, S. T. *Aerosol Sci. Technol.* **2011**, *45* (2), 244–261.
- (92) You, Y.; Renbaum-Wolff, L.; Bertram, a. K. *Atmos. Chem. Phys.* **2013**, *13* (23), 11723–11734.
- (93) Veghte, D. P.; Altaf, M. B.; Freedman, M. a. *J Am Chem Soc* **2013**, *135* (43), 16046–16049.
- (94) Weingartner, E.; Gysel, M.; Baltensperger, U. *Environ. Sci. Technol.* **2002**, *36* (1), 55–62.
- (95) Ma, Q.; Ma, J.; Liu, C.; Lai, C.; He, H. *Environ. Sci. Technol.* **2013**, *47*, 10381–10388.
- (96) Duplissy, J.; Gysel, M.; Sjogren, S.; Meyer, N.; Good, N.; Kammermann, L.; Michaud, V.; Weigel, R.; dos Santos, S. M.; Gruening, C.; Villani, P.; Laj, P.; Sellegri, K.; Metzger, A.; McFiggans, G. B.; Wehrle, G.; Richter, R.; Dommen, J.; Ristovski, Z.; Baltensperger, U.; Weingartner, E.; Martins Dos Santos, S.; Duplissy, J.; Gysel, M.; *S. Atmos. Meas. Tech.* **2009**, *2* (2), 363–378.
- (97) Koehler, K. A.; Kreidenweis, S. M.; DeMott, P. J.; Prenni, A. J.; Carrico, C. M.; Ervens, B.; Feingold, G. *Atmos. Chem. Phys. Discuss.* **2006**, *5* (5), 10881–10924.
- (98) Krieger, U. K.; Marcolli, C.; Reid, J. P. *Chem. Soc. Rev.* **2012**, *41* (19), 6631.

- (99) Lee, A. K. Y.; Ling, T. Y.; Chan, C. K. *Faraday Discuss.* **2008**, *137* (852), 245–263; discussion 297–318.
- (100) Holland, H. D. *The Chemistry of the Atmosphere and Oceans*; Wiley: New York, 1987.
- (101) Kawamura, K. *J. Geophys. Res.* **2003**, *108*, 1–7.
- (102) Baustian, K. J.; Wise, M. E.; Tolbert, M. a. *Atmos. Chem. Phys. Discuss.* **2009**, *9* (5), 20949–20977.
- (103) Zhang, T.; Zhang, C.; Dong, Z.; Guan, Y. *Sci. Rep.* **2015**, *5*, 9143.
- (104) Spinner, E. *Spectrochim. Acta Part A Mol. Biomol. Spectrosc.* **2003**, *59* (7), 1441–1456.
- (105) Baltrusaitis, J.; Grassian, V. H. *Surf. Sci.* **2009**, *603* (17), L99–L104.
- (106) García, R. *Dynamic atomic force microscopy methods*; 2002; Vol. 47.
- (107) Schuttlefield, J.; Al-Hosney, H.; Zachariah, A.; Grassian, V. H. *Appl. Spectrosc.* **2007**, *61* (3), 283–292.
- (108) Han, J.; Martin, S. T. **1999**, *104*, 3543–3553.
- (109) Cziczo, D. J.; Nowak, J. B.; Hu, J. H.; Abbatt, J. P. D. *J. Geophys. Res.* **1997**, *102* (D15), 18843.
- (110) Dougle, P. G.; Veefkind, J. P.; Ten Brink, H. M. *J. Aerosol Sci.* **1998**, *29* (3), 375–386.
- (111) Tang, I. N.; Munkelwitz, H. R.; Procedure, E. **1994**, *99* (94).
- (112) Song, M.; Marcolli, C.; Krieger, U. K.; Lienhard, D. M.; Peter, T. *Faraday Discuss.* **2013**, *165*, 289.
- (113) Tang, I. N.; Munkelwitz, H. R. *Abstr. Pap. Am. Chem. S.* **1977**, *173*, 60.

- (114) Wise, M. E.; Semeniuk, T. a.; Bruintjes, R.; Martin, S. T.; Russell, L. M.; Buseck, P. R. *J. Geophys. Res. Atmos.* **2007**, *112*, 1–12.
- (115) Weis, D. D.; Ewing, G. E.; Song, M.; Marcolli, C.; Krieger, U. K.; Lienhard, D. M.; Peter, T. *J. Geophys. Res.* **2013**, *104* (D17), 289.
- (116) Kohler, H. *Trans. Faraday Soc.* **1936**, *32* (1152), 1152.
- (117) Kreidenweis, S. M.; Koehler, K.; DeMott, P.; Prenni, a. J.; Carrico, C.; Ervens, B. *Atmos. Chem. Phys. Discuss.* **2005**, *5* (1), 287–323.
- (118) Gibson, E. R.; Hudson, P. K.; Grassian, V. H. *J. Phys. Chem. A* **2006**, *110* (42), 11785–11799.
- (119) Laskin, A.; Moffet, R. C.; Gilles, M. K.; Fast, J. D.; Zaveri, R. A.; Wang, B.; Nigge, P.; Shutthanandan, J. *J. Geophys. Res.* **2012**, *117* (D15), D15302.
- (120) Choi, M. Y.; Chan, C. K. *Environ. Sci. Technol.* **2002**, *36* (11), 2422–2428.
- (121) Ghorai, S.; Wang, B.; Tivanski, A.; Laskin, A. *Environ. Sci. Technol.* **2014**, *48* (4), 2234–2241.
- (122) Veghte, D. P.; Bittner, D. R.; Freedman, M. A. *Anal. Chem.* **2014**, *86* (5), 2436–2442.
- (123) Kwamena, N. O. a; Buajarern, J.; Reid, J. P. *J. Phys. Chem. A* **2010**, *114* (18), 5787–5795.
- (124) Ciobanu, V. G.; Marcolli, C.; Krieger, U. K.; Weers, U.; Peter, T. *J. Phys. Chem. Ahemistry. A* **2009**, *113* (41), 10966–10978.
- (125) Parsons, M. T. *J. Geophys. Res.* **2004**, *109* (D6), 1–8.
- (126) Lewis, E. R. *J. Aerosol Sci.* **2006**, *37* (11), 1605–1617.

- (127) Hyvärinen, A. P.; Lihavainen, H.; Gaman, A.; Vairila, L.; Ojala, H.; Kulmala, M.; Viisanen, Y. *J. Chem. Eng. Data* **2006**, *51* (1), 255–260.
- (128) Reid, J. P.; Dennis-Smith, B. J.; Kwamena, N.-O. a; Miles, R. E. H.; Hanford, K. L.; Homer, C. J. *Phys. Chem. Chem. Phys.* **2011**, *13* (34), 15559–15572.
- (129) Buajarn, J.; Mitchem, L.; Reid, J. P. *J. Phys. Chem. A* **2007**, *111*, 9054–9061.
- (130) H., M. R.; M., R. T. *J. Geophys. Res.* **2008**, *113* (August 2007), D04206.
- (131) Freney, E. J.; Adachi, K.; Buseck, P. R. *J. Geophys. Res.* **2010**, *115* (D19), D19210.
- (132) Wexler, A. S.; Seinfeld, J. H. *Atmos. Environ. Part A. Gen. Top.* **1991**, *25* (12), 2731–2748.
- (133) Ge, Z.; Wexler, A. S.; Johnston, M. V. *J. Phys. Chem. A* **1998**, *5639* (97), 173–180.
- (134) Li, X.; Gupta, D.; Eom, H. J.; Kim, H.; Ro, C. U. *Atmos. Environ.* **2014**, *82*, 36–43.
- (135) Park, K.; Kim, J.-S.; Miller, A. L. *J. Nanoparticle Res.* **2009**, *11* (1), 175–183.
- (136) Collins, D. B.; Zhao, D. F.; Ruppel, M. J.; Laskina, O.; Grandquist, J. R.; Modini, R. L.; Stokes, M. D.; Russell, L. M.; Bertram, T. H.; Grassian, V. H.; Deane, G. B.; Prather, K. a. *Atmos. Meas. Tech.* **2014**, *7* (11), 3667–3683.
- (137) Swietlicki, E.; Hansson, H.-C.; Hämeri, K.; Svenningsson, B.; Massling, A.; Mcfiggans, G.; McMurry, P. H.; Petäjä, T.; Tunved, P.; Gysel, M.; Topping, D.; Weingartner, E.; Baltensperger, U.; Rissler, J.; Wiedensohler, A.; Kulmala, M. *Tellus B* **2008**, *0* (0), 080414161623888 – ???

- (138) Zhang, R.; Khalizov, A. F.; Pagels, J.; Zhang, D.; Xue, H.; McMurry, P. H. *Proc. Natl. Acad. Sci. U. S. A.* **2008**, *105* (30), 10291–10296.
- (139) Petters, M. D.; Kreidenweis, S. M. **2007**, 1961–1971.
- (140) Cruz, C. N.; Pandis, S. N. *Environmental Science and Technology*. 2000, pp 4313–4319.
- (141) Prenni, A. J.; DeMott, P. J.; Kreidenweis, S. M.; Sherman, D. E.; Russell, L. M.; Ming, Y. *J. Phys. Chem. A* **2001**, *105*, 11240–11248.
- (142) Mikhailov, E.; Vlasenko, S.; Rose, D.; Pöschl, U. *Atmos. Chem. Phys.* **2013**, *13* (2), 717–740.
- (143) Laskin, a.; Cowin, J. P.; Iedema, M. J. *J. Electron Spectros. Relat. Phenomena* **2006**, *150* (2-3), 260–274.
- (144) Tivanski, A. V.; Hopkins, R. J.; Tyliczszak, T.; Gilles, M. K.; Science, C.; Di, V.; Ad, V.; Source, L.; Berkeley, L. **2007**, 5448–5458.
- (145) Hopkins, R. J.; Desyaterik, Y.; Tivanski, A. V.; Zaveri, R. A.; Berkowitz, C. M.; Tyliczszak, T.; Gilles, M. K.; Laskin, A. *J. Geophys. Res.* **2008**, *113* (D4), D04209.
- (146) Pósfai, M.; Fekete, A.; Vattay, G. *EPL (Europhysics Lett.)* **2010**, *18007*, 1–5.
- (147) Hitzenberger, R.; Berner, A.; Dusek, U.; Alabashi, R. *Aerosol Sci. Technol.* **1997**, *27* (2), 116–130.
- (148) Hegg, D. A.; Covert, D. S.; Crahan, K. K.; Jonsson, H. H.; Liu, Y. *Geophysical Research Letters*. 2006, p L21808.
- (149) Hegg, D. a.; Covert, D. S.; Jonsson, H. H. *Atmos. Chem. Phys. Discuss.* **2008**, *8*, 10531–10560.

- (150) Stock, M.; Cheng, Y. F.; Birmili, W.; Massling, A.; Wehner, B.; Müller, T.; Leinert, S.; Kalivitis, N.; Mihalopoulos, N.; Wiedensohler, A. *Atmos. Chem. Phys.* **2011**, *11* (9), 4251–4271.
- (151) Yeung, M. C.; Chan, C. K. *Aerosol Sci. Technol.* **2010**, *44* (4), 269–280.
- (152) Wang, X.; Sultana, C. M.; Trueblood, J.; Hill, T. C. J.; Malfatti, F.; Lee, C.; Laskina, O.; Moore, K. a.; Beall, C. M.; McCluskey, C. S.; Cornwell, G. C.; Zhou, Y.; Cox, J. L.; Pendergraft, M. a.; Santander, M. V.; Bertram, T. H.; Cappa, C. D.; Azam, F.; DeMott, P. J.; Grassian, V. H.; Prather, K. a. *ACS Cent. Sci.* **2015**, 150518113258002.
- (153) Parsons, M. T.; Knopf, D. a.; Bertram, A. K. *J. Phys. Chem. A* **2004**, *108* (52), 11600–11608.
- (154) Robinson, C. B.; Schill, G. P.; Tolbert, M. a. *J. Atmos. Chem.* **2014**, *71* (2), 145–156.
- (155) Ebert, M.; Inerle-Hof, M.; Weinbruch, S. *Atmos. Environ.* **2002**, *36* (39-40), 5909–5916.
- (156) Hiranuma, N.; Brooks, S. D.; Auvermann, B. W.; Littleton, R. *Atmos. Environ.* **2008**, *42* (9), 1983–1994.
- (157) Hoffman, R. C.; Laskin, A.; Finlayson-Pitts, B. J. *J. Aerosol Sci.* **2004**, *35* (7), 869–887.
- (158) Matsumura, T.; Hayashi, M. *Aerosol Sci. Technol.* **2007**, *41* (8), 770–774.
- (159) Ammann, M.; Zelenay, V.; Krepelova, A.; Birrer, M.; Tzvetkov, G.; Vernooij, M. G. C.; Raabe, J.; Huthwelker, T. *J. Aerosol Sci.* **2011**, *42* (1), 38–51.

- (160) Kelly, S. T.; Nigge, P.; Prakash, S.; Laskin, A.; Wang, B. B.; Tyliczszak, T.; Leone, S. R.; Gilles, M. K. *Rev. Sci. Instrum.* **2013**, *84* (7), 73708.
- (161) Ghorai, S.; Laskin, A.; Tivanski, A. V. *J. Phys. Chem. A* **2011**, *115* (17), 4373–4380.
- (162) Laskina, O.; Morris, H. S.; Grandquist, J. R.; Estillore, A. D.; Stone, E. A.; Grassian, V. H.; Tivanski, A. V. *Environ. Sci. Technol.* **2015**, *49* (22), 13447–13453.
- (163) Gao, Y.; Yu, L. E.; Chen, S. B. *J. Phys. Chem. A* **2007**, *111* (42), 10660–10666.
- (164) Bruzewicz, D. a.; Checco, A.; Ocko, B. M.; Lewis, E. R.; McGraw, R. L.; Schwartz, S. E. *J. Chem. Phys.* **2011**, *134* (4).
- (165) Jacobson, M. Z. *J. Geophys. Res.* **2001**, *106* (2000), 1551.
- (166) Mircea, B. M.; Facchini, M. C.; Decesari, S. *Tellus* **2002**, 74–81.
- (167) Asa-Awuku, a.; Nenes, a.; Sullivan, a. P.; Hennigan, C. J.; Weber, R. J. *Atmos. Chem. Phys. Discuss.* **2007**, *7*, 3589–3627.
- (168) Dinar, E.; Mentel, T. F.; Rudich, Y. *Atmos. Chem. Phys. Discuss.* **2006**, *6*, 7835–7867.
- (169) Parungo, F. P.; Nagamoto, C. T.; Rosinski, J.; Haagenson, P. L. *J. Atmos. Chem.* **1986**, *4* (2), 199–226.
- (170) Park, J. Y.; Kim, M.; Han, S.; Lim, S.; Kim, G.; Park, K. *J. Aerosol Sci.* **2014**, *75*, 22–34.
- (171) Mochida, M.; Umemoto, N.; Kawamura, K.; Lim, H. J.; Turpin, B. J. *J. Geophys. Res.* **2007**, *112* (D15), D15209.

- (172) Held, I. M.; Soden, B. J. *Annu. Rev. Energy Environ.* **2000**, 25 (1), 441–475.
- (173) Power, R. M.; Reid, J. P. *Rep. Prog. Phys.* **2014**, 77 (7), 074601.
- (174) Badger, C. L.; George, I.; Griffiths, P. T.; Braban, C. F.; Cox, R. a.; Abbatt, J. P. *D. Atmos. Chem. Phys. Discuss.* **2005**, 5 (5), 9581–9620.
- (175) Freedman, M. a.; Baustian, K. J.; Wise, M. E.; Tolbert, M. a. *Anal. Chem.* **2010**, 82 (19), 7965–7972.
- (176) Martin, S. T. *Chem. Rev.* **2000**, 100 (617), 3403–3453.
- (177) Zhang, X.; Massoli, P.; Quinn, P. K.; Bates, T. S.; Cappa, C. D. **2014**, No. 1, 8384–8399.
- (178) Hansson, H. C.; Rood, M. J.; Koloutsou-Vakakis, S.; Hämeri, K.; Orsini, D.; Wiedensohler, a. *J. Atmos. Chem.* **1998**, 31 (3), 321–346.
- (179) DeMott, P. J.; Sullivan, R. C.; Ruppel, M. J.; Hill, T. C.; Mason, R.; Ault, A. P.; Prather, K. a.; Collins, D. B.; Kim, M. J.; Bertram, A.; Bertram, T.; Grassian, V. K.; Franc, G. D. **2013**, 941 (2013), 941–944.
- (180) Ault, A. P.; Guasco, T. L.; Baltrusaitis, J.; Ryder, O. S.; Trueblood, J. V.; Collins, D. B.; Ruppel, M. J.; Cuadra-Rodriguez, L. a.; Prather, K. a.; Grassian, V. H. *J. Phys. Chem. Lett.* **2014**, 5 (15), 2493–2500.
- (181) Pradeep Kumar, P.; Broekhuizen, K.; Abbatt, J. P. D. *Atmos. Chem. Phys. Discuss.* **2003**, 3, 949–982.
- (182) Takemura, T.; Nozawa, T.; Emori, S.; Nakajima, T. Y.; Nakajima, T. *J. Geophys. Res. D Atmos.* **2005**, 110 (2), 1–16.
- (183) Sorjamaa, R.; Svenningsson, B.; Raatikainen, T.; Laaksonen, A. *Atmos. Chem. Phys. Discuss.* **2004**, 4 (3), 2781–2804.

- (184) Kokkola, H.; Sorjamaa, R.; Peräniemi, a.; Raatikainen, T.; Laaksonen, a. *Geophys. Res. Lett.* **2006**, *33* (10), n/a – n/a.
- (185) Raatikainen, T.; Laaksonen, a. *Geosci. Model Dev. Discuss.* **2010**, *3* (3), 1139–1159.
- (186) Willeke, K.; Whitby, K. T. *J. Air Pollut. Control Assoc.* **1975**, *25* (5), 529–534.
- (187) Raymond, T. M.; Pandis, S. N. *J. Geophys. Res. Atmos.* **2002**, *107* (24), 4787.
- (188) Tang, I. N.; Tridico, a. C.; Fung, K. H. *J. Geophys. Res.* **1997**, *102*, 23269.
- (189) Peng, C.; Chan, M. N.; Chan, C. K. *Environ. Sci. Technol.* **2001**, *35* (22), 4495–4501.
- (190) de Leeuw, G.; Neele, F. P.; Hill, M.; Smith, M. H.; Vignati, E. *J. Geophys. Res.* **2000**, *105* (D24), 29397.
- (191) Leeuw, G. De; Andreas, E. L.; Anguelova, M. D.; Fairall, C. W.; Ernie, R.; Dowd, C. O.; Schulz, M.; Schwartz, S. E. **2011**, *80* (2010), 1–39.
- (192) Gwaze, P.; Annegarn, H. J.; Huth, J.; Helas, G. *Atmos. Res.* **2007**, *86* (2), 93–104.
- (193) Yazdanpanah, M. M.; Hosseini, M.; Pabba, S.; Berry, S. M.; Dobrokhoto, V. V.; Safir, A.; Keynton, R. S.; Cohn, R. W. *Langmuir* **2008**, *24* (23), 13753–13764.
- (194) Barber, A. H.; Cohen, S. R.; Daniel Wagner, H. *Phys. Rev. Lett.* **2004**, *92* (18), 186103–1.
- (195) Walczyk, W.; Schönherr, H. *Langmuir* **2014**, *30* (24), 7112–7126.
- (196) Uddin, M. H.; Tan, S. Y.; Dagastine, R. R. *Langmuir* **2011**, *27* (6), 2536–2544.
- (197) Vignati, E.; Facchini, M. C.; Rinaldi, M.; Scannell, C.; Ceburnis, D.; Sciare, J.; Kanakidou, M.; Myriokefalitakis, S.; Dentener, F.; O’Dowd, C. D. *Atmos. Environ.* **2010**, *44* (5), 670–677.

- (198) Quinn, P. K.; Bates, T. S.; Schulz, K. S.; Coffman, D. J.; Frossard, a. a.; Russell, L. M.; Keene, W. C.; Kieber, D. J. *Nat. Geosci.* **2014**, 7 (3), 228–232.
- (199) Narukawa, M.; Kawamura, K.; Takeuchi, N.; Nakajima, T. **1999**, 26 (20), 3101–3104.
- (200) Röhrl, A.; Lammel, G. *Environ. Sci. Technol.* **2001**, 35 (1), 95–101.
- (201) Kiss, G.; Tombácz, E.; Hansson, H. C. *J. Atmos. Chem.* **2005**, 50 (3), 279–294.
- (202) Hutter, J. L.; Bechhoefer, J. *Rev. Sci. Instrum.* **1993**, 64 (7), 1868–1873.
- (203) McGuiggan, P. M.; Wallace, J. S. *J. Adhes.* **2006**, 82, 997–1011.
- (204) Yazdanpanah, M. M.; Harfenist, S. A.; Safir, A.; Cohn, R. W. *J. Appl. Phys.* **2005**, 98 (7), 0–7.
- (205) Krueger, B. J.; Grassian, V. H.; Iedema, M. J.; Cowin, J. P.; Laskin, a. *Anal. Chem.* **2003**, 75 (19), 5170–5179.
- (206) Extended AIM Aerosol Thermodynamics Model
<http://www.aim.env.uea.ac.uk/aim/aim.php>.
- (207) Dutcher, C. S.; Wexler, A. S.; Clegg, S. L. *J. Phys. Chem. A* **2010**, 114 (46), 12216–12230.
- (208) Clegg, S. L.; Pitzer, K. S.; Brimblecombe, P. *J. Phys. Chem.* **1992**, 96 (23), 9470–9479.
- (209) Wexler, A. S.; Clegg, S. L. *J. Geophys. Res.* **2002**, 107 (D14), 4207.
- (210) Clegg, S. L.; Brimblecombe, P.; Wexler, A. S. *The Journal of Physical Chemistry A*. 1998, pp 2155–2171.
- (211) Pope, F. D.; Dennis-smither, B. J.; Griffiths, P. T.; Clegg, S. L.; Cox, R. A. *Growth Factors* **2010**, 5335–5341.

- (212) Aerosol Inorganic-Organic Mixture Functional groups Activity Coefficients.
- (213) Zuend, A.; Marcolli, C.; Booth, A. M.; Lienhard, D. M.; Soonsin, V.; Krieger, U. K.; Topping, D. O.; McFiggans, G.; Peter, T.; Seinfeld, J. H. *Atmos. Chem. Phys.* **2011**, *11* (17), 9155–9206.
- (214) Cruz, C. N.; Pandis, S. N. *Atmos. Environ.* **1997**, *31* (15), 2205–2214.
- (215) Gérard, V. M. F.; Noziere, B.; Baduel, C.; Fine, L.; Frossard, A. A.; Cohen, R. C. *Environ. Sci. Technol.* **2016**, acs.est.5b05809.
- (216) Egemen, E.; Nirmalakhandan, N.; Trevizo, C. *Environ. Sci. Technol.* **2000**, *34* (12), 2596–2600.
- (217) Spracklen, D. V.; Arnold, S. R.; Sciare, J.; Carslaw, K. S.; Pio, C. *Geophys. Res. Lett.* **2008**, *35* (12), 1–5.
- (218) Moffet, R. C.; Henn, T. R.; Tivanski, a. V.; Hopkins, R. J.; Desyaterik, Y.; Kilcoyne, a. L. D.; Tyliczszak, T.; Fast, J.; Barnard, J.; Shutthanandan, V.; Cliff, S. S.; Perry, K. D.; Laskin, a.; Gilles, M. K. *Atmos. Chem. Phys. Discuss.* **2009**, *9*, 16993–17033.
- (219) Wolfenden, R.; Wolfenden, R. **2006**, *106* (July), 3379–3396.
- (220) Copeland, R. a; Pompliano, D. L.; Meek, T. D. *Nat. Rev. Drug Discov.* **2006**, *5* (9), 730–739.
- (221) Zinn, N.; Hopf, C.; Drewes, G.; Bantscheff, M. *Methods* **2012**, *57* (4), 430–440.
- (222) Ho, W. *J. Chem. Phys.* **2002**, *117* (24), 11033.
- (223) Evans, E. **2001**.
- (224) Neuman, K. C.; Nagy, A. *Nat. Methods* **2008**, *5* (6), 491–505.

- (225) Müller, D. J.; Krieg, M.; Alsteens, D.; Dufrêne, Y. F. *Curr. Opin. Biotechnol.* **2009**, *20* (1), 4–13.
- (226) Florin, A. E.; Moy, V. T.; Gaub, H. E. **2016**, *264* (5157), 415–417.
- (227) Hinterdorfer, P.; Dufrêne, Y. F. *Nat. Methods* **2006**, *3* (5), 347–355.
- (228) Lee, C. K.; Wang, Y. M.; Huang, L. S.; Lin, S. *Micron* **2007**, *38* (5), 446–461.
- (229) Ray, C.; Brown, J. R.; Akhremitchev, B. B. *Langmuir* **2007**, *23* (11), 6076–6083.
- (230) Ebner, A.; Wildling, L.; Kamruzzahan, A. S. M.; Rankl, C.; Wruss, J.; Hahn, C. D.; Hölzl, M.; Zhu, R.; Kienberger, F.; Blaas, D.; Hinterdorfer, P.; Gruber, H. J. *Bioconjug. Chem.* **2007**, *18* (4), 1176–1184.
- (231) Cecconi, C.; Shank, E. A.; Dahlquist, F. W.; Marqusee, S.; Bustamante, C. *Eur. Biophys. J.* **2008**, *37* (6), 729–738.
- (232) Touhami, A.; Jericho, M. H.; Beveridge, T. J. *Langmuir* **2007**, *23* (5), 2755–2760.
- (233) Moffitt, J. R.; Chemla, Y. R.; Smith, S. B.; Bustamante, C. *Annu. Rev. Biochem.* **2008**, *77*, 205–228.
- (234) Ratto, T. V.; Langry, K. C.; Rudd, R. E.; Balhorn, R. L.; Allen, M. J.; McElfresh, M. W. *Biophys. J.* **2004**, *86* (4), 2430–2437.
- (235) Friedsam, C.; Wehle, A. K.; K hner, F.; Gaub, H. E. *J. Phys. Condens. Matter* **2003**, *15* (18), S1709–S1723.
- (236) Singh, P.; Morris, H.; Tivanski, A. V.; Kohen, A. *Data Br.* **2015**, *4*, 19–21.
- (237) Cameron, C. E.; Benkovic, S. J. *Biochemistry* **1997**, *36* (50), 15792–15800.
- (238) Ravi Rajagopalan, P. T.; Lutz, S.; Benkovic, S. J. *Biochemistry* **2002**, *41* (42), 12618–12628.
- (239) Kohler, N.; Sun, C.; Wang, J.; Zhang, M. *Langmuir* **2005**, *21* (19), 8858–8864.

- (240) Klein, D. C. G.; Stroh, C. M.; Jensenius, H.; Van Es, M.; Kamruzzahan, A. S. M.; Stamouli, A.; Gruber, H. J.; Oosterkamp, T. H.; Hinterdorfer, P. *ChemPhysChem* **2003**, *4* (12), 1367–1371.
- (241) Stroh, C. M.; Ebner, A.; Geretschläger, M.; Freudenthaler, G.; Kienberger, F.; Kamruzzahan, A. S. M.; Smith-Gill, S. J.; Gruber, H. J.; Hinterdorfer, P. *Biophys. J.* **2004**, *87* (3), 1981–1990.
- (242) Stroh, C.; Wang, H.; Bash, R.; Ashcroft, B.; Nelson, J.; Gruber, H.; Lohr, D.; Lindsay, S. M.; Hinterdorfer, P. *Proc. Natl. Acad. Sci. U. S. A.* **2004**, *101* (34), 12503–12507.
- (243) Benters, R.; Niemeyer, C. M.; Wöhrle, D. *Chembiochem* **2001**, *2* (9), 686–694.
- (244) Nitin, N.; LaConte, L. E. W.; Zurkiya, O.; Hu, X.; Bao, G. *J. Biol. Inorg. Chem.* **2004**, *9* (6), 706–712.
- (245) Grandbois, M.; Beyer, M.; Rief, M.; Clausen-Schaumann, H.; Gaub, H. E. *Science* (80-.). **1999**, *283* (5408), 1727–1730.
- (246) McGuire, J. *Curr. Pharm. Des.* **2003**, *9*, 2593–2613.
- (247) Ruiz-pernia, J. J.; Luk, L. Y. P.; Garc, R.; Mart, S.; Loveridge, E. J. **2013**.
- (248) Wang, Z.; Wang, Y.; Zhang, L. *J. Am. Chem. Soc.* **2014**, *136* (25), 8887–8890.
- (249) Singh, P.; Abeysinghe, T.; Kohen, A. *Molecules* **2015**, *20* (1), 1192–1209.
- (250) Francis, K.; Kohen, A. *Curr. Opin. Chem. Biol.* **2014**, *21C*, 19–24.
- (251) Hammes-Schiffer, S. *Acc. Chem. Res.* **2006**, *39* (2), 93–100.
- (252) Liu, H.; Warshel, a. *J. Phys. Chem. B* **2007**, *111*, 7852–7861.
- (253) Rod, T. H.; Brooks, C. L. *J. Am. Chem. Soc.* **2003**, *125* (29), 8718–8719.

- (254) Clementi, C.; Jennings, P. a; Onuchic, J. N. *Proc. Natl. Acad. Sci. U. S. A.* **2000**, 97 (11), 5871–5876.
- (255) K., A. R.; Li, L.; Badilla, C. L.; Fernandez, J. M. *Biophys. J.* **2005**, 88, 168a – 168a.
- (256) Rief, M.; Gautel, M.; Oesterhelt, F.; Fernandez, J. M.; Gaub, H. E. *Science* **1997**, 276 (5315), 1109–1112.
- (257) Boland, T.; Ratner, B. D. *Proc. Natl. Acad. Sci. U. S. A.* **1995**, 92 (12), 5297–5301.
- (258) Lee, G. U.; Chrisey, L. a; Colton, R. J. *Science (80-.)*. **1994**, 266 (5186), 771–773.
- (259) Strunz, T.; Oroszlan, K.; Schäfer, R.; Güntherodt, H. J. *Proc. Natl. Acad. Sci. U. S. A.* **1999**, 96 (20), 11277–11282.
- (260) Pope, L. H.; Davies, M. C.; Laughton, C. a; Roberts, C. J.; Tendler, S. J.; Williams, P. M. *Eur. Biophys. J.* **2001**, 30 (1), 53–62.
- (261) Rief, M.; Clausen-Schaumann, H.; Gaub, H. E. *Nat. Struct. Biol.* **1999**, 6 (4), 346–349.
- (262) Noy, a; Vezenov, D. V; Kayyem, J. F.; Meade, T. J.; Lieber, C. M. *Chem. Biol.* **1997**, 4 (7), 519–527.
- (263) Fierke, C. a; Johnson, K. a; Benkovic, S. J. *Biochemistry* **1987**, 26 (13), 4085–4092.